Michael Hertz Vaksdal

Pipeline Free Span Fatigue Based on DNV RP & Time Domain VIV Modelling Procedures

Master's thesis in Marine Technology
Supervisor: Prof. Svein Sævik, NTNU, Nils Melhuus, Reinertsen New Energy, Tom Bostrøm, Reinertsen New Energy
June 2023

Master's thesis

NTNU
Norwegian University of
Science and Technology

Michael Hertz Vaksdal

Pipeline Free Span Fatigue Based on DNV RP & Time Domain VIV Modelling Procedures

Master's thesis in Marine Technology
Supervisor: Prof. Svein Sævik, NTNU, Nils Melhuus, Reinertsen New Energy, Tom Bostrøm, Reinertsen New Energy
June 2023

Norwegian University of Science and Technology
Faculty of Engineering
Department of Marine Technology

NTNU
Norwegian University of
Science and Technology

Master Thesis Description Spring 2023

for

Stud. Tech. Michael Hertz Vaksdal

**Pipeline Free Span Fatigue Based on DNV RP &
Time Domain VIV Modelling Procedures**
*Virvelindusert utmatting av frie spenn i rørledninger
med bruk av DNVs responsmodell versus tidsplan VIV modell*

Vortex Induced Vibrations (VIV) can lead to fast accumulation of fatigue damage to offshore slender structures, such as free spanning subsea pipelines. A new empirical method for time domain (TD) calculation of VIV has been developed by NTNU. This method is capable of accounting for structural non-linearity and time-varying flow compared to the traditional frequency domain analyses. The objective of this study is to compare validate the TD-VIV prediction tool for free spanning pipelines and evaluate non-linear local stress at pipeline shoulders.

The master work to be performed during Spring 2023 represents a continuation of the project work performed in Fall 2022 and is to be carried out as follows:

1. Report the result of the literature review conducted during Fall 2022 into the master thesis document.
2. If deemed necessary, additional literature review into the fundamental theory of VIV & VIM, numerical prediction, tools and relevant standards. This is to further support the scope of work identified during the project thesis Fall 2022.
3. If deemed necessary, adjust the models obtained in project thesis.
4. Continue analysis of established case scenario and perform correlation studies between the response-based procedure of the DNV RP and the TD-VIV model in SIMLA addressing both in-line and cross-flow fatigue.
5. Perform sensitivity studies on cases/parameters agreed upon with the supervisors.
6. Conclusions and recommendations for further work.

The work scope may prove to be larger than initially anticipated. Subject to approval from the supervisors, topics may be deleted from the list above or reduced in extent. This is to be notified to the reader in the introduction.

In the master report, the candidate shall present his/her personal contribution to the resolution of problems within the scope of the master work.

Theories and conclusions should be based on mathematical derivations and/or logic reasoning identifying the various steps in the deduction.

The candidate should utilise the existing possibilities for obtaining relevant literature.

Master report format

The master report should be organised in a rational manner to give a clear exposition of results, assessments, and conclusions. The text should be brief and to the point, with a clear language. Telegraphic language should be avoided.

The report shall contain the following elements: A text defining the scope (this document to be included), preface, list of contents, summary, main body of thesis, conclusions with recommendations for further work, list of symbols and acronyms, references and (optional) appendices. All figures, tables and equations shall be numerated.

The supervisors may require that the candidate, in an early stage of the work, presents a written plan for the completion of the work.

The original contribution of the candidate and material taken from other sources shall be clearly defined. Work from other sources shall be properly referenced using an acknowledged referencing system.

The report shall be submitted in electronic format (.pdf):
-   Signed by the candidate.
-   The text defining the scope shall be included (this document).
-   Drawings and/or computer models that are not suited to be part of the report in terms of appendices shall be provided on separate (.zip) files.

Ownership

NTNU has according to the present rules the ownership of the master reports. Any use of the report has to be approved by NTNU (or external partner when this applies). The department has the right to use the report as if the work was carried out by a NTNU employee, if nothing else has been agreed in advance.

Thesis supervisors:

Prof. Svein Sævik, NTNU,
Nils Melhuus, Reinertsen New Energy,
Tom Bostrøm, Reinertsen New Energy.

Deadline: June 11th, 2023.

Trondheim, January 2023.

Svein Sævik   Nils Melhuus   Tom Bostrøm

Candidate – date and signature:

Michael Hertz Vaksdal, January 15th, 2023.

Preface

The following report is the outcome of my master's thesis at the Department of Marine Technology, Norwegian University of Science and Technology. It is a continuation of the project work conducted during the fall semester of 2022.

The focus of this master's thesis is on the analysis of pipeline free span fatigue, utilizing the recommended response-based model by DNV, and the recently NTNU-developed time-domain model for the prediction of vortex-induced vibrations (VIV). Extensive efforts have been invested in learning the fundamental principles of the VIV phenomenon and gaining proficiency in utilizing DNV's software, Fat-Free, along with the non-linear finite element tool, SIMLA. SIMLA are employed in conjunction with the time domain VIV model, to accurately predict the occurrence of vortex-induced vibrations and the impact on the fatigue life of the pipeline.

Professor Svein Sævik, Department of Marine Technology, NTNU, Nils Melhuus, Reinertsen New Energy, Nikolai Hammer, Reinertsen New Energy (Fall 2022) and Tom Bostrøm (Spring 2023), has made significant contributions to the thesis and to whom I would like to convey my profound gratitude. During our weekly sessions, their advice and suggestions were really helpful in achieving the objectives of the work. The importance of their high level of dependability and accessibility should be highlighted in particular because their assistance has been needed on several occasions throughout the project, mainly by providing data and input to the model, and their willfulness to share their knowledge and offer me insightful counsel.

It is advised that the readers of this paper have a basic understanding of structural analysis and hydro-dynamics. Understanding the context of this report would be made easier by having a basic knowledge of the fundamental theory underlying static and dynamic analysis. A prior understanding of some fundamental VIV-related topics would also be helpful.

Abstract

Free spanning subsea pipelines are subjected to various environmental loads, among which vortex-induced vibrations (VIV) are one of the most significant contributors leading to fatigue failure. VIV is a self-excited phenomenon caused by the interaction between ocean currents and waves with the pipeline, which can induce large-amplitude oscillations and high stress concentrations at specific locations of the pipeline. The detrimental effects of VIV on the integrity of free spanning subsea pipelines have been widely studied in the past decades, leading to the development of various VIV prediction models and tools. However, VIV remains a major challenge in design and operation, and further research is required to improve the understanding of VIV mechanisms and enhance the reliability of VIV prediction.

This master thesis investigates the fatigue damage of a free-spanning pipeline for a given case scenario using two different VIV prediction models; the recommended response-based model in DNV-RP-F105 and a newly developed time-domain VIV (TD-VIV) model at NTNU. The software FatFree is used in compliance with the response-based model, and the finite element method (FEM) tool SIMLA is used for the TD-VIV model. The study includes a sensitivity analysis of the shoulder elements and a parameter study on the hydrodynamic coefficients used for the TD-VIV model.

The study finds that the in-line damage per year calculated by FatFree and SIMLA is in good agreement, but the cross-flow damage shows an order of magnitude difference between the two, with FatFree being more conservative. The sensitivity analysis highlights the importance of choosing the correct element for fatigue damage calculations in SIMLA, with a significant difference seen in the maximum damage between neighbouring elements due to non-linear effects and shifting constraints present in the TD-VIV model. The parameter study shows that the default parameters for the TD-VIV model in SIMLA correlate well with the response model in FatFree for the in-line response amplitude, while a reduced quadratic drag coefficient predicts a significantly larger response. None of the parameter sets corresponds well with the response model in FatFree for the cross-flow response amplitude, and the response model is generally more conservative compared to the TD-VIV model for all current velocities, explaining the higher cross-flow damage per year in the case scenario.

Overall, the study provides insights into the importance of choosing the correct model and parameter sets for VIV prediction in fatigue damage calculations for free-spanning pipelines. The results suggest further work is needed to validate the TD-VIV model with reference data and develop standard procedures and coefficients for different free-span situations.

Table of Contents

List of Figures

List of Tables

List of Abbreviations

3D	Three-dimensional
CFD	Computational Fluid Dynamics
CF	Cross-flow
DNV	Det Norske Veritas
DOF	Degrees of Freedom
FD	Frequency Domain
FEM	Finite Element Method
FFT	Fast Fourier Transform
IL	In-line
RM	Response Model
RP	Recommended Practice
TD	Time Domain
VIM	Vortex-Induced Motions
VIV	Vortex-Induced Vibrations

Nomenclature

α	Parameter that determines the extent of the dependence of the IL force frequency on the respective CF frequency (initial IL synchronization model)
α_1	Mass-proportional damping coefficient
α_2	Stiffness-proportional damping coefficient
Δt	Time-step
$\dot{\phi}_{exc,x}$	In-line instantaneous frequency
$\dot{\phi}_{exc,y}$	Cross-flow instantaneous frequency
$\dot{x}_{rel}$	Relative in-line velocity of the structure
$\dot{y}_{rel}$	Relative cross-flow velocity of the structure
$\hat{f}$	Non-dimensional oscillation frequency
$\hat{f}_{0,x}$	Non-dimensional in-line excitation frequency of maximum energy transfer
$\hat{f}_{0,y}$	Non-dimensional cross-flow excitation frequency of maximum energy transfer
$\hat{f}_{exc,x}$	Non-dimensional in-line excitation frequency used to denote the IL synchronization range
$\hat{f}_{exc,y}$	Non-dimensional cross-flow excitation frequency used to denote the CF synchronization range
$\hat{f}_{max,x}$	Upper limit of the IL synchronization range
$\hat{f}_{max,y}$	Upper limit of the CF synchronization range

$\hat{f}_{min,x}$	Lower limit of the IL synchronization range
$\hat{f}_{min,y}$	Lower limit of the CF synchronization range
λ_i	Modal damping ratio for mode number i
C	System's damping matrix
F	Total hydrodynamic force
K	System's mass matrix
$\mathbf{u_n}, \mathbf{\dot{u}_n}$	Normal component of the incident flow velocity and acceleration vectors
$\mathbf{u_t}$	Tangential component of the incident flow velocity vector
$\mathbf{u}$	Incident flow velocity vector
$\mathbf{v_n}$	Relative flow velocity vector
ν	Kinematic viscosity of the fluid
ν	Posson's ratio
ω	Oscillation frequency in rad/s
ω_n	Natural oscillation frequency for mode number n
$\phi_{\dot{x}_{rel}}$	Instantaneous phase angle of the structure's relative in-line velocity
$\phi_{\dot{y}_{rel}}$	Instantaneous phase angle of the structure's relative cross-flow velocity
$\phi_{exc,x}$	Instantaneous phase angle of the vortex-induced excitation force in the IL direction
$\phi_{exc,y}$	Instantaneous phase angle of the vortex-induced excitation force in the CF direction
ρ	Density of the fluid
ρ_s/ρ	Specific mass ratio
θ	Angular position in pipe cross-section
θ_x	Instantaneous phase difference between the structure's relative in-line velocity and the in-line excitation force
θ_y	Instantaneous phase difference between the structure's relative cross-flow velocity and the cross-flow excitation force
ζ_{pipe}	Structural damping ratio of the pipe
ζ_{soil}	Soil damping ratio
ζ_{s}	Structural damping ratio
A	Cross-sectional area of the examined cylinder or pipe
C_A	Added mass coefficient
C_D	Non-dimensional drag coefficient
C_L	Lateral dynamic stiffness factor
C_L	Non-dimensional lift coefficient
$C_{v,x}$	In-line vortex-induced excitation force coefficient
$C_{v,y}$	Cross-flow vortex-induced excitation force coefficient

C_V	Vertical dynamic stiffness factor
D	Diameter of the examined cylinder or pipe
EA	Axial stiffness
EI	Bending stiffness
F_x	Drag force
$f_{exc,x}$	In-line excitation frequency
$f_{exc,y}$	Cross-flow excitation frequency
$f_{n,x}$	Still water natural frequency in the in-line direction for mode number n
$f_{n,y}$	Still water natural frequency in the cross-flow direction for mode number n
f_{osc}	Oscillation frequency
f_s	Vortex shedding frequency
F_y	Lift Force
G	Shear Modulus of the soil
k	Spring stiffness
K_C	Keulegan-Carpenter number
k_i	Linearized spring stiffness at support no. i
$K_{L,d}$	Lateral Dynamic Soil Stiffness
$K_{L,s}$	Lateral Static Soil Stiffness
$K_{V,d}$	Vertical Dynamic Soil Stiffness
$K_{V,s}$	Vertical Static Soil Stiffness
L	Length of the pipe
L_s	Length of the free span
M	Bending moment
m	Dry mass
m^*	Mass ratio
m_a	Added mass
Q	Shear force
Q_v	Static vertical soil reaction force per unit length of pipe
Re	Reynolds number
St	Strouhal number
t	Time variable
U	Incident flow velocity
V_R	Reduced velocity
f_n	Still water natural frequency for mode number n

1 Introduction

1.1 Background and motivation

To have as much value creation as possible from the extraction of Norwegian petroleum resources, efficient transportation methods are needed. The offshore pipeline network on the Norwegian continental shelf in Figure 1.1 is an important part of this, where the gas pipeline system alone has a total length similar to the distance between Oslo and Bangkok according to Norskpetroleum.no. In addition, there are several kilometres of pipelines connecting oil fields to the mainland oil terminals.

These pipelines often pass uneven areas on the seafloor. One of the main concerns regarding this is the formation of free spans when crossing depressions. Consequently, if subjected to dynamic loads, oscillations might occur and time-varying stresses and associated fatigue damage may eventually lead to structural failure. Vortex-induced vibrations (VIV) caused by currents are a major source of dynamic stresses, but VIV due to waves in addition to direct wave loads are also important at shallower water depths. The key challenge for the industry today is to verify that the pipeline can sustain the environmental conditions it is subjected to throughout its lifetime.

Accurate prediction of fatigue damage due to vortex-induced vibrations is difficult due to the complex interaction between loads and structural response. Several models and procedures exist today to describe the phenomenon. Often used are empirical models relying on experimental data, which are usually restricted to solving the equation of motion in the frequency domain. That is, it is only suitable for linear models and steady-state flows. Further, combined frequency interactions are difficult to account for, and vortex-induced vibrations due to unsteady flows such as waves and time-varying currents are not predictable. Additionally, cross-flow and in-line motion are predicted separately, neglecting the combined effect between the two.

A free spanning pipeline is a highly non-linear scenario and includes non-linear effects such as pipe-soil interaction and tensile variations. To include these important effects in a VIV analysis, and to solve the aforementioned problems, a time domain (TD) model for vortex-induced vibrations must be coupled with a nonlinear structural model. Such a promising TD VIV model has been developed by PhD. Mats J. Thorsen at the Department of Marine Technology has been implemented into the nonlinear structural software SIMLA. In this thesis, this approach is investigated and compared with one of the leading industry approaches (fatigue analysis of free spanning pipelines using FatFree), for a highly realistic free span scenario.

Figure 1.1: Pipelines on the Norwegian Continental Shelf.

1.2 Structure of the thesis

Chapter 2 serves as an introduction to the fundamental theory of VIV essential for this thesis. In order to explain the hydrodynamic phenomena observed when the cylinder is subjected to a fluid flow, a concise presentation of the fundamental theory underlying VIV is given, with emphasis on both rigid and elastically mounted cylinders. Following this, VIV prediction models are defined and elaborated on.

Chapter 3 gives an introduction to the main characteristics of free spanning subsea pipelines. It defines important parameters that are used in free span assessments and elaborates on the structural response of flexible members under dynamic loading. Additional theory regarding VIV on free spanning pipelines is described in this chapter.

Chapter 4 is based on *DNV-RP-F114: Pipe-soil interaction for submarine pipelines*, and provides a concise introduction to the topic of pipe-soil interaction for submarine pipelines. This chapter focuses on the characteristics of soil stiffness and damping and offers some of the simplifications suggested in the recommended practice for soil and damping properties in free spanning pipeline analysis.

Chapter 5 provides the two VIV assessment models used in the thesis. The underlying theory of the VIV response-based model currently used by the industry and the newly developed time-domain model are presented and formulated.

Chapter 6 elaborates on the theory used for the cumulative damage analysis on the time-domain model. That is, the rainflow counting algorithm, which is ideal for systems under varying amplitude and frequency loading. The chapter additionally introduces the Palmgren-Miner linear damage rule and Haibach SN-curves.

Chapter 7 presents the case scenario developed from data provided by Reinertsen New Energy in order to define and model a realistic free span scenario. Pipeline geometry and mechanical properties are given, as well as seabed geotechnical properties and environmental conditions at the site.

Chapter 8 provides an overview of the modelling of the structural model in SIMLA, as well as the modelling of current conditions and pipe-soil interaction. The hydrodynamic properties used for the model in the case scenario are also given in this chapter.

Chapter 9 gives a description of the analysis methodology that was used in order to perform the stress and fatigue calculations for the case scenario. Additional theories about static, modal and dynamic analysis methods are elaborated on.

Chapter 10 presents the results and discussion of the case scenario for the two VIV models. Details about the static configuration of the pipeline in shutdown condition, possible excited modes, FatFree and SIMLA fatigue damage/y results for a specific shoulder element are provided. Additionally, representative simulation results from the TD-VIV model are given.

Chapter 11 gives the results of two sensitivity studies that were performed on the model. The first study investigated the sensitivity between the damage/y of the shoulder elements of the SIMLA model, while the second study studies the sensitivity of the hydrodynamic parameters used for the model. The second study also compares the response and damage/y for individual currents with the response-based model in FatFree.

Chapter 12 finally summarizes and concludes the results and a recommendation for further work is given.

2 Fundamental theory of vortex-induced vibrations

2.1 Steady flow around a circular cylinder

When a real fluid flows past a circular cylinder, a boundary layer that travels along it is formed due to fluid viscosity according to Hibbeler [1]. The layer contains different velocity gradients, which at the instant surface is zero because of the no-slip condition. Further, it tends to stick to the cylinder surface due to the *Coanda effect*. Point A in Figure 2.1 is called the stagnation point and is where the incoming flow hits the cylinder. From there, the boundary layer is formed at the surface as the fluid travels along it. In the region AB' the layer travels with an increasing velocity, producing a favourable pressure gradient that decreases within the region (Bernoulli's principle). At B', the maximum velocity and minimum pressure occur. Downstream from B', there is a decreasing velocity until flow separation occurs at C'. This happens as velocity gradients close to the surface become zero or negative and we get a region of reversed flow. As this happens, vortices are shed downstream. A series of vortices is called a wake.
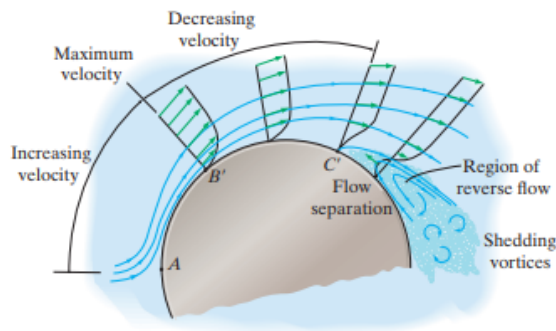
Figure 2.1: Boundary layer separation [1].

A parameter that is helpful for predicting the flow pattern around the cylinder is the *Reynolds number* as given by Sumer and Fredsøe [2]. It can be defined as the ratio of inertial forces to viscous forces within a fluid that is subjected to relative internal movement due to different fluid velocities:

$$Re = \frac{UD}{\nu},$$

(2.1)

where U is the incoming flow velocity, D is the characteristic dimension for the body around which the fluid flows (diameter in the case of a cylinder), and ν is the kinematic viscosity of the fluid. In general, for a very low Reynolds number ($Re < 5$), the flow will be laminar and follow the contours of its obstruction, and no vortices will appear. When $5 < Re < 40$ a fixed and symmetric pair of vortices is formed in the wake. For $40 < Re < 200$ the vortices will shed downstream in a laminar vortex street. Further, a transition to turbulence in the wake will happen at $200 < Re < 300$. In the range of $300 < Re < 3 \times 10^5$ the wake is completely turbulent, while the boundary layer separation on each side of the cylinder is laminar. This is called the *subcritical* regime. Next is the *critical* regime at ($3 \times 10^5 < Re < 3.5 \times 10^5$), where one side has a laminar boundary separation and the other has a turbulent boundary separation (but laminar boundary layers). When $3.5 \times 10^5 < Re < 1.5 \times 10^6$ the flow is in the *supercritical* regime, where turbulent boundary layer separation on both sides is present, and the boundary layers are partly laminar and partly turbulent. At $1.5 \times 10^6 < Re < 4 \times 10^6$ the boundary layer is completely turbulent at one side. Lastly, the boundary layer on both sides is completely turbulent for $4 \times 10^6 < Re$, which is

called the *transcritical* regime. An overview of the different regimes is added in Appendix A. Typical for free spanning pipelines are $10^4 < Re < 2 \times 10^6$ as illustrated in Figure 2.2. The figure was made by using a current velocity of 2m/s as extreme current condition, and $D = 1.2$m as the largest pipeline diameter for the maximum Reynold numbers, considering that the largest subsea pipeline in the north sea (Langeled) has a diameter of 1.1m. It can be seen that these Reynold numbers lie between the subcritical, critical and supercritical regimes, where vortex shedding is highly relevant.
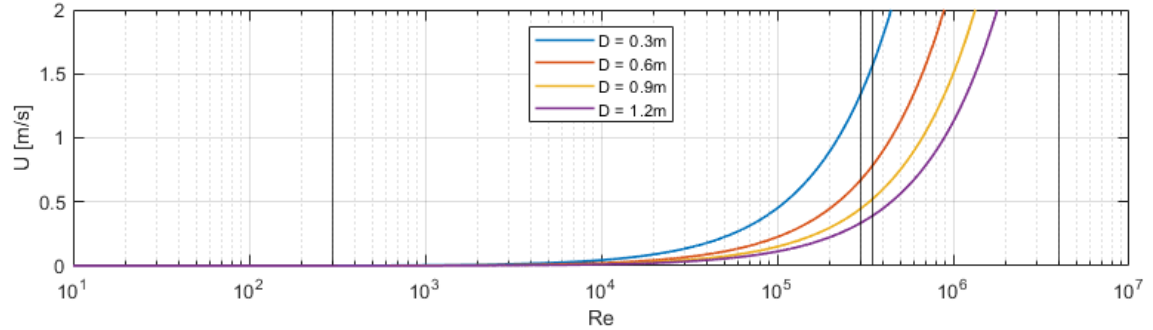
Figure 2.2: Typical Reynolds number for free spanning pipelines. Vertical black lines represent the four regimes from left to right; subcritical (Re > 300), critical, supercritical and transcritical.

Most experimental data for vortex shedding are obtained in the subcritical regime, and there exist fewer data and more uncertainties regarding empirical models at higher Reynolds numbers. However, it is commonly conservative to use data from the subcritical regime when applied to cases with higher *Re*. One of the first to investigate the stream behind a cylinder was Theodore von Kármán, hence the vortex stream formed is often called a *von Kármán vortex street*.
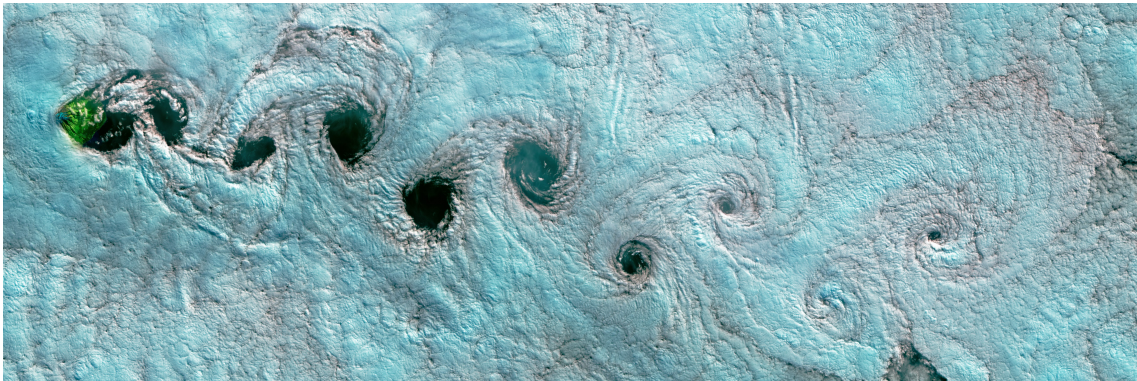
Figure 2.3: Satellite captured photo (natural color) of the formation of a Von Kármán vortex street in the clouds at Guadalupe Island, Mexico. Taken by NASA in 2017.

The Strouhal frequency, f_s at which the vortices are shed from each side of the cylinder is a function of the *Strouhal number, St*:

$$f_s = \frac{St\, U}{D},\qquad(2.2)$$

where St is a dimensionless parameter which is highly dependent on the Reynolds number. Empirical values for different cases are developed and can be found in the literature. Data for a smooth and rough cylinder is shown in Figure 2.4. It can clearly be seen that for the smooth cylinder, the Strouhal number is

a function of the Reynolds number and that for the rough cylinder, it is relatively insensitive to it. Subsea pipelines normally have a sufficiently rough surface to give a fairly stable vortex shedding process, and $St = 0.2$ is often an accurate approximation under the transcritical regime in which they lie.
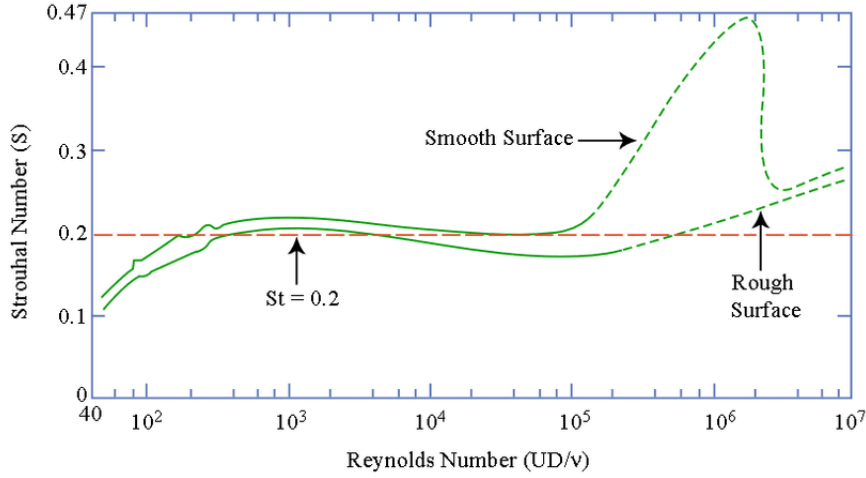
Figure 2.4: Relationship between Strouhal number and Reynolds number for vortex shedding on a circular cylinder in uniform flow. Plot by MIT OCW. Data is taken from Lienhard (1966) and Achenbach and Heinecke (1981).

The stream of alternating vortex shedding behind the cylinder causes fluctuations in pressure, which leads to oscillating forces in the vertical and horizontal directions. These are called lift force and drag force respectively, and are obtained by integrating the fluid pressure over the surface. In addition to the oscillating drag component, there is a mean drag component due to tangential viscous shear stress. In fluid mechanics, it has become a standard procedure to describe drag and lift by the following two equations:

$$F_y = \frac{1}{2}\rho U^2 C_y D \qquad and \qquad F_x = \frac{1}{2}\rho U^2 C_x D, \qquad (2.3)$$

where F_y is the lift force, F_x is the drag force, and C_y and C_x is their corresponding dimensionless drag and lift coefficients. ρ is the fluid density. It is important to note that the lift force oscillates with the same frequency as the shedding frequency, and the drag force oscillates at a frequency of $2f_s$. The latter is small compared to mean drag and fluctuating lift. Because of symmetry, the mean lift force is zero.
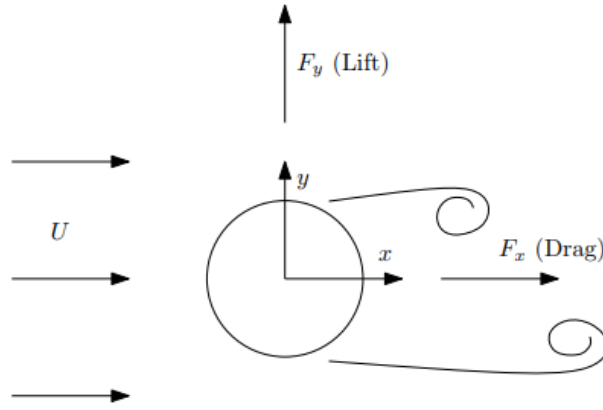
Figure 2.5: Illustration of drag and lift force in an incoming fluid flow [3].

2.2   Lock-in phenomena on elastically mounted rigid cylinders

If we consider the cylinder as a dynamic system it will have an oscillating response to the excitation forces from the vortex shedding, either in pure cross-flow (CF) or in-line (IL) direction or in a combination of both. This is what is called vortex-induced vibrations, or VIV. The uncoupled equation of motion (using the cross-flow direction as an example) can be described by:

$$m\ddot{y} + c\dot{y} + ky = F_y,$$ (2.4)

where m is the cylinder dry mass, c is the structural damping coefficient and k is the spring stiffness. The force components can, in general, be divided into two components; one which is in phase with the cylinder velocity, and one which is in phase with cylinder acceleration. The component that is in phase with the cylinder velocity will either dampen or excite the system, while the component in phase with the acceleration works as an inertia force, and may be expressed as an added mass m_a. That is, the mass an object appears to have when it is accelerated relative to a surrounding fluid. The natural frequency of such a dynamic system including the added mass can in general be described by:

$$f_n = 2\pi \sqrt{\frac{k}{m + m_a}}.$$ (2.5)

Note that the added mass is a function of the cylinder's oscillation frequency and amplitude, which means that the natural frequency has the ability to change when there is an incoming flow. Therefore, resonance might occur over a range of different excitation frequencies. This flow-dependent frequency is denoted as f_{osc}. Numerous VIV experiments have been performed on rigid cylinders for pure cross-flow, pure in-line, and combined in-line and cross-flow responses. An extensively used parameter for the determination of the velocity ranges where vortex shedding will be in resonance with the natural frequency is called the *reduced velocity*, V_R:

$$V_R = \frac{U}{f_n D}.$$ (2.6)
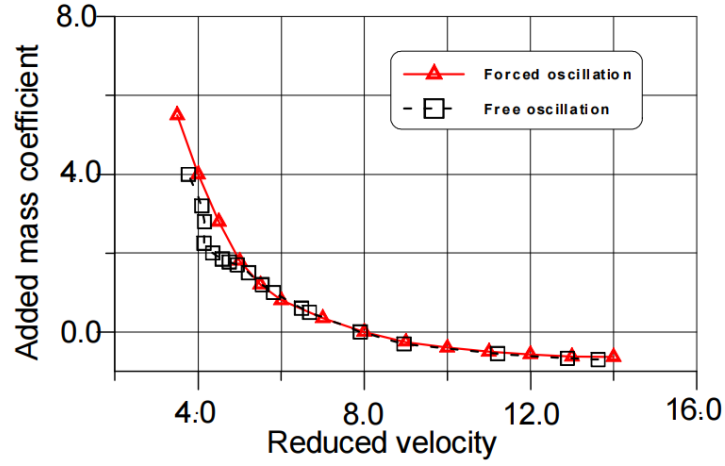
Figure 2.6: Added mass coefficient vs. reduced velocity for forced oscillations (Gopalkrishnan [4]) and free oscillations (Vikestad et al. [5]).

One experiment was conducted in the absence of added mass in order to maintain the still water natural frequency, it showed that for $V_R < 5$ the cylinder did not vibrate and that the vortex shedding followed the Strouhal frequency. As the reduced velocity increased to 5, the cylinder started to vibrate as $f_s = f_n$. When the reduced velocity increased further, the shedding frequency would continue to lock on to the natural frequency of the cylinder until $V_R \approx 7$. This effect was described as the lock-in phenomenon or synchronization. In seawater, added mass has a significant influence on the natural frequency and lock-in range, and cannot be neglected. A mass ratio was therefore introduced, as a measure of the ratio between cylinder mass and mass of displaced fluid:

$$m^* = \frac{m}{0.25\rho\pi D^2}.$$ (2.7)

Some literature uses ρD^2 in the denominator. A larger mass ratio gives a lower lock-in range than a lower mass ratio. Typically, cross-flow vortex-induced vibrations occur in a reduced velocity range of $3 \le V_R \le 16$ for low mass ratios, i.e. for pipelines and risers, and maximum response amplitude lies normally between $5 \le V_R \le 9$ as shown in Figure 2.7. In-line vibrations typically occur for $1 \le V_R \le 4.5$.
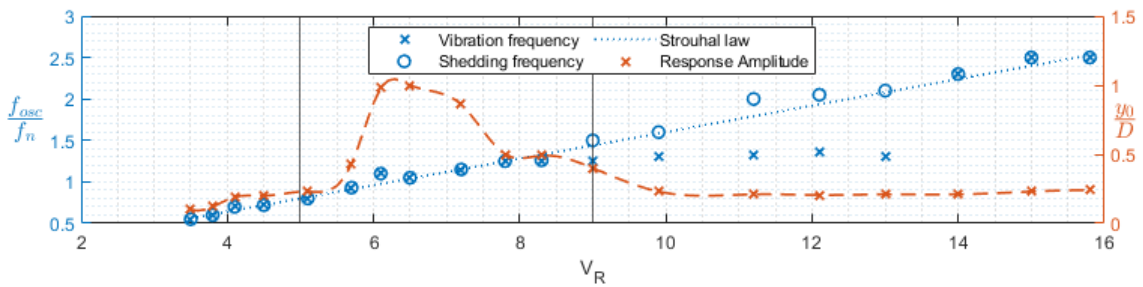
Figure 2.7: Crossflow response of a flexibly-mounted circular cylinder subject to steady current in water. m* = 5.3. (Anand, 1985). Figure is for illustration purposes and data is extracted from a figure in a paper by Sumer and Fredsøe [6].

The peak amplitude of the response denoted as y_0/D is independent of the mass ratio m^*, but varies with the structural response as $m^*\zeta_s$, where ζ_s is the structural damping ratio due to internal friction.

For slender elements in water, this ratio ranges from 0.005 for steel pipes to 0.03-0.04 for flexible pipes according to Blevins [7]. Studies on the coupled cross-flow and in-line response (2-DOF) of the cylinder by Sarpkaya [8] have shown that the response also is affected by the ratio between their respective natural frequencies. For mass ratios less than 6, the maximum cross-flow amplitude increased significantly due to in-line vibrations having an effect on it. The large amplitude also introduced a new wake mode named 3T, forming triplets of vortices on each half cycle as shown by Jauvtis and Williamson [9]. For mass ratios larger than 6, this effect was not seen. In addition, experiments for Reynolds number in the sub-critical range for elastically mounted cylinders show that the maximum response amplitude and the mean drag decreases for increasing roughness and that the synchronization is delayed and bandwidth reduced.

The drag coefficients of an oscillating cylinder are different than for a cylinder in still water, and an additional drag amplification due to vortex-induced vibrations is of importance when performing VIV assessments. Different expressions for the increase in drag exist in the literature, and a simple formulation applicable to an elastically mounted rigid cylinder is also given by Blevins:

$$C_D = C_{Do} \left[1 + 2.1 \left(\frac{y_0}{D} \right) \right].$$

(2.8)

The stability parameter, K_s, is another factor influencing the response. This is also known as the Scrouton number and is proportional to the damping and inversely proportional to the total shedding force of the excited vertices. As a result, the parameter is large when the damping is large or when the lock-in region of the member is small in comparison to the pipe length. The stability parameter is defined for a uniform diameter and a uniform flow condition along the member length as:

$$K_S = \frac{2m\,\zeta}{\rho D^2},$$

(2.9)

where m is dry mass, ζ is the sum of structural damping ζ_s, soil damping ζ_{soil}, other damping ζ_{other}, and hydrodynamic damping ζ_h. For more details see *DNV-RP-C205: Environmental Conditions and Environmental Loads* [10].

2.3 VIV in time-varying flows

Flows are rarely in a steady state at sea, so we have to consider a cylinder subjected to a sinusoidal flow with velocity $U(t) = U_m sin(2\pi f_w t)$. By assuming that the Strouhal relation is still valid, the vortex shedding frequency can be written as:

$$f_s(t) = St \frac{U_m}{D} |sin(2\pi f_w t)|.$$

(2.10)

From this it is observed that excitation (positive energy transfer) is only possible at specific time intervals, shown in Figure 2.8. That is when the vortex shedding frequency is close to and synchronizes with the cylinder's natural frequency. Outside of these intervals, the main force acting on the cylinder will be damping. The VIV response is anticipated to be more erratic than in the case of steady flow because the situation is continuously switching from excitation to damping. In addition, vertices previously shed might be present in the incoming flow, which further complicates the matter.
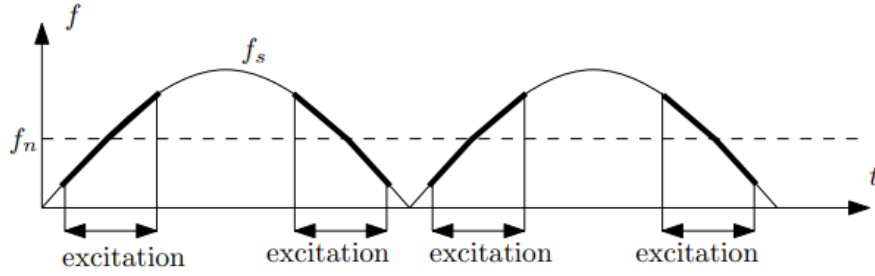
Figure 2.8: Illustration of shedding frequency for a cylinder in a sinusoidal flow [3].

The Keulegan-Carpenter number (KC number), also known as the period number, is a dimensionless quantity used in fluid dynamics to indicate the relative importance of drag forces over inertia forces for a bluff object in an oscillating flow. Likewise, it can be used for an oscillating body in a fluid at rest. Inertia predominates for lower KC, whereas drag forces are important for larger KC. For an oscillating flow, it is in general given as:

$$KC = \frac{U_m T_w}{D},$$
(2.11)

where U_m flow velocity oscillation amplitude and $T_w = 1/f_w$ is the oscillation period. Since $A_m = U_m T_w / 2\pi$ in a sinusoidal flow the equation can be rewritten as:

$$KC = \frac{2\pi A_m}{D}.$$
(2.12)

We can interpret this as a measure of the distance the flow travels before it is reversed relative to the cylinder diameter.

2.4 VIV prediction models

For prediction of vortex-induced vibrations the following models can be used according to DNV-RP-C205 [10]:

- Response-based models

    Response-based models are empirical models that give the steady state VIV amplitude as a function of hydrodynamic and structural parameters. These models are based on high-quality experimental data and are often used for screening analysis, producing conservative results. A commonly used and recommended practice for free spanning pipelines is the response-based model described in *DNV-RP-F105: Free Spanning Pipelines* [11], which is used in conjunction with DNV's software *FatFree* [12].

- Force-based models

    Inertia, damping, and excitation forces are calculated using integrated force coefficients derived from empirical data. Structure-based parameters are used to calculate the response. A force model is based on the well-known Morison's equation. Solutions in the time domain (TD) and frequency domain (FD) are both acceptable. A time domain solution can account for all significant

non-linearities, but it generally requires more computational effort. Universally applicable force models for VIV do not exist today, and empirical response models are in general superior for free span assessments. The newly developed TD-VIV model is a promising force-based model and is used in conjunction with the FEM tool SIMLA in this thesis.

- Flow-based models

    Flow-based models simulate the fluid flow around the structure and deduce the forces acting on it from the characteristics of the flow (velocity and its gradients, fluid pressure). This definition includes solving Navier-Stokes equations, which is known as computational fluid dynamics (CFD). However, not all approaches that are regarded as flow-based models completely and consistently resolve the Navier-Stokes equations. Some problems may be solved using boundary layer equations, whereas other solutions of the problem use inviscid flow techniques, where the solution consists of discrete vortex particles in otherwise potential flow. These models are computationally expensive and not applicable for large and complex problems, and will not be discussed or used in this thesis.

3 Free spanning subsea pipelines

3.1 Problem definition

The single free spanning pipeline in Figure 3.1 is suspended above the ocean floor between two touch-down points, which are typically referred to as the span shoulders or soil supports. The following section will give a description of basic parameters that influence the pipeline's dynamic response as suggested by Vedeld et al. [13].
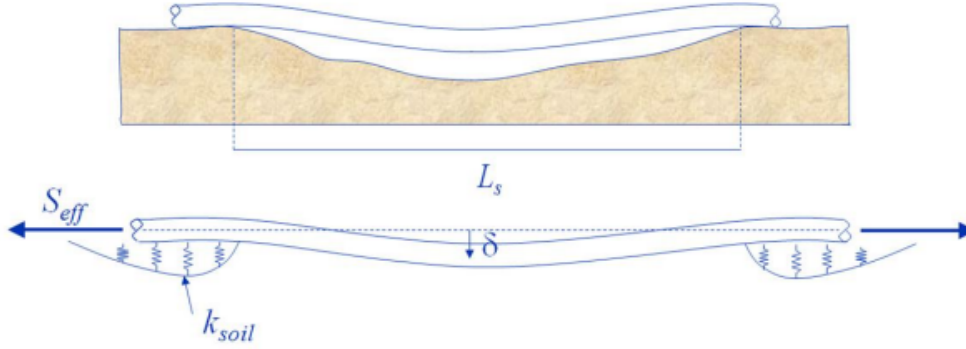
Figure 3.1: Free span scenario of a pipeline, indicating free span length L_s, soil stiffness k_s, effective axial force S_{eff}, and mid-span deflection, δ [13].

Naturally, the span length has a significant impact on the dynamic response. The pipe has an effective mass per unit length m_e, which is taken as the total of the dry mass, that is the mass of the steel pipe and all of its coatings, the mass of the fluid inside, and the mass added by hydrodynamics (due to acceleration of the surrounding water). The pipe has an axial stiffness of EA and a bending stiffness of EI, where E is Young's modulus and I is the second moment of inertia, and A is the steel pipe's cross-sectional area. The geometric stiffness of the pipeline is taken into consideration in addition to the stiffness of the soil and the structure. Effective axial force, given by Equation 3.1, is defined as positive in tension and affects the geometric stiffness of the pipeline. It is determined by and equals the axial force, N, in the steel wall adjusted for the effects of internal pressure, p_i, and external pressure, p_e, according to Vedeld et al. [14].

$$S_{eff} = N - p_i A_i + p_e A_e. \tag{3.1}$$

A_e is the external cross-sectional area including all coating layers and A_i is the internal cross-sectional area of the pipe. When a pipe is completely restrained axially, maximum compression is achieved, and the effective axial force can then be expressed as:

$$S_{eff} = H_{eff} - \Delta p_i A_i (1 - 2\nu) - EA\alpha\Delta T, \tag{3.2}$$

where H_{eff} is the residual lay tension, Δp_i is the change in internal pressure with respect to the time of laying, α is the pipe steel's temperature expansion coefficient, and T is the change in temperature since the time of laying. The effective axial force for a pipe that is totally unrestrained axially is zero.

For a response-based model or force-based model in the frequency domain, separate modal analyses must be performed for CF and IL direction since the soil stiffness and static configuration are typically different in both directions. The bending stiffness and the axial stiffness of the pipe become coupled as a result of the static deflection into the span in the cross-flow direction. Thus, providing more stiffness due to this arc-like effect, which could significantly raise the natural frequency of the free span. Hence, the fundamental cross-flow frequency is dependent on the mid-span deflection. If the drag loading caused by a steady current is not negligible, the static deflection in the in-line direction should also be taken into consideration.

3.2 VIV on subsea pipelines

To understand the behaviour of a subsea pipeline, it is useful to start with the dynamic equilibrium equation of a beam. As depicted in Figure 3.2, the equation can be derived by considering the vertical equilibrium of a small segment of the cylinder with a length of dz. The resulting equation is as follows:

$$T\frac{\partial^2 u}{\partial z^2} + \frac{\partial Q}{\partial z} + q(z,t) = m\frac{\partial^2 u}{\partial t^2}, \tag{3.3}$$

The variable u represents the lateral displacement of the cylinder. The tension is denoted by T, the internal shear force by Q, the external lateral load by q, and the mass per unit length of the cylinder by m. The shear force Q can be described in terms of the bending moment M, which is determined by the bending stiffness EI and the curvature of the cylinder by:

$$Q = \frac{\partial M}{\partial z} = \frac{\partial}{\partial z}\left(-EI\frac{\partial^2 u}{\partial z^2}\right), \tag{3.4}$$

If we assume that EI remains constant, we can derive the dynamic equilibrium equation for the cylinder by substituting Equation 3.4 into Equation 3.3:

$$m\frac{\partial^2 u}{\partial t^2} - T\frac{\partial^2 u}{\partial z^2} + EI\frac{\partial^4 u}{\partial z^4} = q(z,t). \tag{3.5}$$

It is important to note that Equation 3.5 is only applicable to small displacements and does not account for shear deformations. Moreover, if the tension T is constant, the equation indicates that when the cylinder vibrates freely (i.e., $q(z,t) = 0$), the solution for the lateral displacement can be expressed as:

$$u(z,t) = \psi(z)Y(t) = u_0 \sin\left(\frac{n\pi z}{L}\right)\sin\omega_n t, \qquad n = 1,2... \tag{3.6}$$

In this case, the cylinder is assumed to be pinned, implying that both the displacement and curvature are zero at both ends. The initial portion of the solution, which characterizes the spatial variation of the displacement, is known as the mode shape. Figure 3.3 illustrates the first four mode shapes (i.e., for n = 1-4). Each mode is linked to a natural frequency, which is determined as follows:

$$\omega_n = \frac{n\pi}{L}\sqrt{\frac{T}{m} + \left(\frac{n\pi}{L}\right)^2 \frac{EI}{m}}. \tag{3.7}$$

As expressed in the equation, the natural frequency of the cylinder increases with increasing n, indicating that the first mode has the lowest natural frequency. The natural frequency is influenced by both the tension and bending stiffness, with the bending stiffness becoming progressively more significant as n increases.
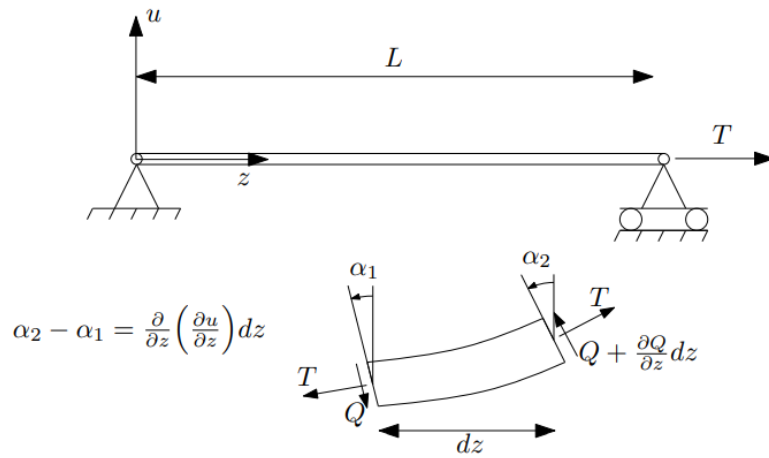
Figure 3.2: Flexible cylinder and internal forces acting on a small segment dz in a displaced configuration [3].
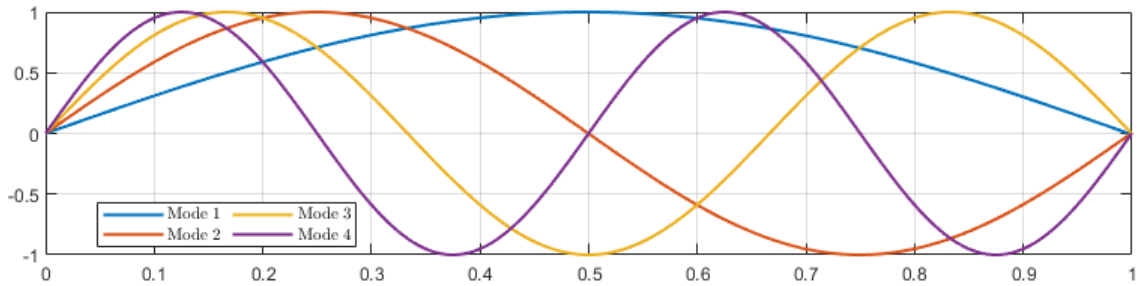
Figure 3.3: Normalized modeshapes for $n = 1, 2, 3, 4$ for a pinned-pinned beam under axial load.

A significant amount of work has been done to modify the analytical expressions for the natural frequencies and mode shapes to a free spanning pipeline for both in-line and cross-flow vibrations. The optimized solutions include coating stiffness, initial deflection, soil stiffness effects and so-called effective span lengths. For a full elaboration on the state-of-the-art analytical formulas see Fyrileiv and Mørk [15] and DNV-RP-F105 [11].

In Section 2.2 the effect of VIV was explained for an elastically mounted rigid cylinder. To better understand the effects of VIV on free spanning subsea pipelines, we examine it for an incoming flow with increasing velocity on a beam. As the beam has an infinite number of natural frequencies, lock-in can occur for any of these frequencies, making the dynamic behaviour more complicated. The oscillation frequency initially follows the Strouhal law for low current velocities, giving small vibration amplitudes. As the oscillation frequency gets close to the first natural frequency of the beam, ω_1, synchronization occurs as expected significant response amplitudes. For the elastically mounted rigid cylinder, a further increase in flow velocity would result in desynchronization and the oscillations to go back to following Strouhal's law, resulting in lower vibration amplitudes. This is not the case for a free spanning subsea pipeline, as the second natural frequency of the beam, ω_2, might lie in the vicinity of the oscillation frequency. The response amplitude might therefore increase or decrease depending on the energy

transfer between the fluid and the pipe. To summarize the above, it is clear that in the case of flexible pipes, the oscillation frequency might be close to the infinite many natural frequencies of the structure at any time. Thus, resulting in lock-in and high amplitude vibrations. Further, only steady current has been considered, and more complexity is introduced considering pipes in space- and time-varying flow. According to Voie et al. [16] this can introduce a "multi-frequency" response, where several natural frequencies can be excited simultaneously across the length of the pipe. In addition, since the flow velocity varies over the span length, the response can consist of either standing (combination of two waves moving in opposite directions) or travelling waves according to an experimental investigation of a long marine riser by Trim et al. [17]. The former is more common for lower flow velocities and the latter for higher flow velocities.

Besides the fundamental cross-flow and in-line responses at vortex shedding frequencies of f_s and $2f_s$ respectively, a third harmonic component associated with shedding frequencies of $3f_s$ was briefly mentioned in section 2.2, forming triplets of vertices. This higher-order component is non-negligible as it might be close to one of the structure's natural frequencies, resulting in high-frequency stresses and fatigue damage accumulation. In many cases, the stresses induced by the third harmonic component can be the dominant source of stresses and fatigue damage, which is more significant for tension-dominated beams than for bending-dominated beams. This correlates to stresses from the third harmonic component to be more significant at lower vibration modes which usually are tension dominated rather than at higher vibration modes where bending stiffness dominates. In addition, the study shows that higher harmonic VIV occurs typically for high flow velocity, that is for travelling waves rather than standing waves. It should be mentioned that the study was on a slender vertical riser, where tension tends to dominate rather than on a free spanning subsea pipeline where bending stiffness tends to dominate.

As mentioned, the presence of a sag caused by gravity is another distinctive feature of free spanning pipelines. Sag can lead to different natural frequencies in the two orthogonal directions (IL and CF). Specifically, the presence of a long and deep sag highly influences the natural frequency in the CF direction, leading to first-mode cross-flow natural frequencies to be close to or higher than second-mode in-line natural frequencies. In addition, the mode shape of the first CF mode for a significant sag is often a 2nd harmonic. As a result, simultaneous mode 1 CF and IL vibration can occur.

3.3 In-line vibrations

Research on VIV in long, slender marine structures such as risers and pipelines has predominantly focused on cross-flow vibrations. However, recent studies have shifted their attention towards in-line and the combined effects of both phenomena. As mentioned, the vortex shedding frequency of IL-VIV is twice as high as that of CF-VIV, which makes it more likely to occur over lower flow velocities. This means that fatigue damage from IL-VIV accumulates much faster than fatigue damage from CF-VIV. Typically, free spanning pipelines are designed to avoid cross-flow vibrations and are more exposed to experience fatigue damage from in-line vibrations. In-line vibrations can be divided into three categories, two of which occur at low-velocity current (first and second instability region), and a third region observed at higher velocities in connection with cross-flow VIV, called cross-flow induced in-line vibrations.

In the first instability region, which occurs for reduced velocities between 1 and 2.5, two coupled processes lead to the vibrations of a cylinder. Firstly, normal vortex shedding occurs, inducing two oscillations per shedding. Secondly, the relative IL motion of the cylinder to the fluid causes symmetric vortex shedding. The formation of secondary, symmetric vortex shedding suggests that vibrations from normal vortex shedding already exist. However, in a flow without turbulence or perturbation, the secondary

system would not occur. But if excited, the IL force of the flow oscillates at a frequency approximately three times the Strouhal frequency according to Sumer and Fredsøe [2]:

$$\frac{f_x D}{U} = 3St,$$ (3.8)

where f_x is the frequency of the oscillating IL force. When the frequency of the oscillating force is close to a natural frequency f_n, "first lock-in" occurs, resulting in large vibration amplitudes. When the reduced velocity is increased further, resulting in larger f_x, the difference between f_x and f_n is also increased. Consequently, the symmetric vortex shedding stops. In cases where only normal vortex shedding is present, the IL-force frequency is as mentioned about twice the Strouhal frequency. This value is lower compared to the first instability region. As the reduced velocity of the flow increases further, the IL-force frequency approaches the natural frequency again, leading to the second lock-in, giving large vibration amplitudes. The second instability region occurs at reduced velocities between 2.5 and 4. It is important to note that a constant Strouhal number of 0.2 is assumed until this point, as is often the case for the sub-critical regime. However, for larger Strouhal numbers, the first and second instability regions occur at lower reduced velocity values. The amplitudes of IL VIV in these two regions are generally much smaller than CF VIV amplitudes. This is because IL VIV can be initiated from smaller forces and at lower current velocities. Furthermore, the drag coefficient CD during IL VIV is smaller than the lift coefficient CL during CF VIV

Cross-flow induced in-line VIV occurs in a reduced velocity region that is typically associated with the initiation of CF VIV, but far from any lock-in point for in-line vibrations. However, significantly larger IL-motion and IL-force amplitudes compared to the first and second instability regions can be observed here. The IL-force frequency acting on the cylinder is still twice the Strouhal frequency. To initiate IL VIV in this higher reduced velocity region, several phenomena must occur simultaneously. Firstly, the cylinder must experience much higher velocities than in the IL region, leading to larger vibration amplitudes in the CF direction. Secondly, stronger and more orderly vortex shedding must occur, which results in an increase in the drag force coefficient. This increase in the drag force coefficient ultimately causes IL VIV. Strong growth of the fluctuating drag coefficient for a cylinder oscillating in the CF direction is observed for A/D ratios greater than 0.2 to 0.3.
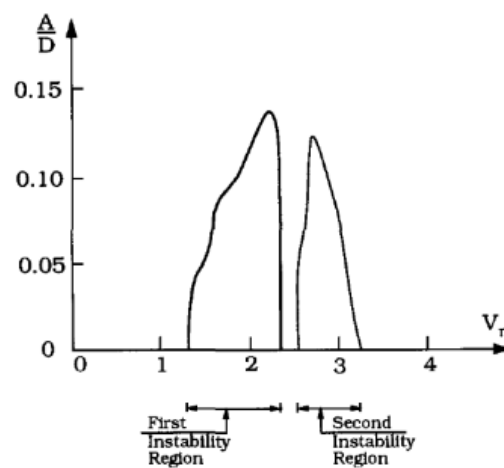
Figure 3.4: First and second instability region for in-line VIV for a cylinder with $Re = 6 \times 10^4$ [2].

3.4   Pipeline conditions

Free span assessments must be carried out independently for each phase of the pipeline's design life since the static configuration of the pipeline, as well as the span lengths and effective axial forces will vary. The different phases are defined as:

- After installation, the pipe is usually in a temporary state called "as-laid condition," in which the internal pressure and temperature are low and the effective axial force is equal to the residual lay tension. We expect the span lengths and gaps to be large, and the static deflection from self-weight to be moderate.

- A "water-filled state" occurs when the pipe is flooded or completely filled with water prior to the system pressure test. The additional submerged weight brought on by the water content will result in significant static deflections brought on by gravity. The deflections into the spans cause the pipe to stretch, and in areas with several spans, the effective axial force may thus approach larger tensile values.

- A "*pressure-test condition*" is when the pressure within the water-filled pipe is increased to a certain level. Given the pressure tests' limited duration, modal analyses and assessments of fatigue caused by VIV are often not required. However, as the pressure test is non-linear and dependent on the sequence of loading, it should be included in the static analysis in order to later provide an accurate estimate of the static configuration.

- The pipeline is said to be in an "*operational condition*" when it is filled with the intended fluid, such as gas or oil. Of course, it is the phase of the pipeline's design life that lasts the longest. Equation 3.2 states that when operational pressure and temperature are supplied, the effective axial force transforms into a compressive force. The increased internal pressure and temperature cause the pipe to expand, slide axially and sag deeper into the spans (a process known as "feed-in"). Consequently, free span lengths and gaps tend to shorten during the operational period.

- "*Shut-down condition*". Multiple cycles of alternating shut-down and operational states may occur in the pipe. The static configuration must be determined for shut-down conditions (i.e., with fluid content but at reduced pressure and temperature) if the duration of the shut-down phases is not negligible with regard to fatigue damage.

4 Pipe-Soil interaction for subsea pipelines

The flow conditions and structural characteristics of subsea pipelines are highly dependent on the properties of the soil, i.e. the pipe's static configuration, its natural frequencies, the "lock-in" phenomena, and in general the dynamic behaviour is affected by it. An accurate representation of the seabed and its properties is difficult due to its unevenness and irregularities in material properties along its path, but several methods and recommendations exist whereas the *DNV-RP-F114: Pipe-soil interaction for submarine pipelines* [18] is a leading practice. The shoulders of the free span, where the pipe is in contact with the seafloor, are typically an area of considerable stress concentration as a result of resonant VIV occurrences. Due to this, there may be a non-negligible accumulation of fatigue damage in this area. In addition, the formation of free spans is not the only typical pipeline scenario where pipe-soil interaction is important. According to the recommended practice, other common pipeline scenarios include lateral buckling, end expansion, pipeline walking, route-curve pullout, flow line anchoring, on-bottom stability, and trawl impact.

As briefly mentioned in the introduction, a free spanning pipeline includes non-linear properties in which the interaction between pipe and soil is an important factor to consider. That is since the position of the touchdown point and the general area of contact between the pipe and the soil will be strongly dependent on the pipe's actual time-varying response, as well as a number of other factors, e.g. the fluctuation of the applied tension and the modification of the seabed's profile due to soil erosion. Also, non-linear soil damping has a significant impact on the response. This means that a non-linear structural model, as well as a time-domain analysis, should be performed to include these effects. For instance, if springs are used to simulate the seafloor contact in an analysis (also called a "penalty formulation" for contact), the spring properties must be non-linear in order to both prevent the pipe from penetrating the seafloor and to take into account the "lift-off" phenomenon that allows the pipe to detach from the seafloor and reattach to it during its oscillatory motion. Applying this non-linear contact formulation to the seafloor will result in a non-linear and time-varying boundary condition.

In addition to some of the aforementioned uncertainties, the soil surrounding the pipe might eventually be disturbed, i.e. new trenches can develop and soil properties can change. Due to all the complexities regarding the pipe-soil interaction, simplifications and assumptions have been made in order to establish trustworthy and efficient soil models. From DNV-RP-F114 the pipe-soil interaction can be divided into five categories:

- *Embedment*: This is the vertical pipe-soil interaction, where the initial embedment is governed by the soil conditions and the loads during and following installation. This has a significant influence on the subsequent axial and lateral response.

- *Axial friction*: This is the axial pipe-soil interaction which can be subdivided into three divisions:

  - *Axial breakout response*: An initial peak in resistance that is mainly relevant to the first load response.

  - *Axial residual resistance*: The large displacement response as the pipe expands or contracts.

  - *Cyclic axial response*: The long-term cyclic response under repeated expansion and contraction.

- *Lateral resistance*: This is the lateral pipe-soil interaction which can be subdivided into three divisions:

- *Lateral breakout response*: An initial peak in the resistance as the pipe first displaces from the as-installed position

- *Lateral residual resistance*: The large displacement resistance.

- *Cyclic lateral response*: The long term cyclic response, when the pipe becomes embedded in a trench within a buckled pipe section and soil berms grow causing a rise in lateral resistance.

- *Soil stiffness*: Can be subdivided into vertical static and dynamic stiffness, and lateral static and dynamic stiffness.

- *Soil damping*: Soil damping may be introduced in dynamic analyses.

The modelling of the first three types of pipe-soil responses is a challenging procedure and necessitates in-depth knowledge of the soil properties and the pipeline installation process. Only soil stiffness and damping will be discussed in more detail in the following.

4.1 Soil stiffness

It is apparent that the type of soil being considered has a significant impact on how rigid the seafloor is. The soil material can be divided into two major groups; cohesive soil (clay), and cohesionless soil (sand), in accordance with DNV-RP-F114. The various types of soil have diverse characteristics, however, the shear strength, soil submerged unit weight, Poisson's ratio, and plasticity index are among the most crucial for determining the soil stiffness. It is advised in the recommended practice to employ elastic springs to describe the seabed properties if the non-linear response of the seabed cannot be explicitly taken into consideration while evaluating soil stiffness. These springs must be able to take into account the response of the seafloor, which is inherently non-linear. By employing this method, the soil stiffness can be represented as a secant stiffness, which represents the projected load level in the pipeline scenario under consideration. Additionally, it is advised to make a distinction between static soil stiffness, which is typically linked to a static loading state, and dynamic soil stiffness, which is typically linked to a dynamic loading state.

4.1.1 Static soil stiffness

The static vertical stiffness is a secant stiffness that reflects penetration situations like those that occur during installation and when free spans emerge as a result of erosion. The following equation defines static vertical stiffness [18]:

$$K_{V,s} = \frac{Q_v}{z},$$ (4.1)

where Q_v is the static soil reaction force per unit length of pipe, and z is the vertical soil penetration. It is possible to establish a penetration curve using DNV-RP-F114. Figure 4.2 shows examples of equivalent secant stiffness at various load levels.
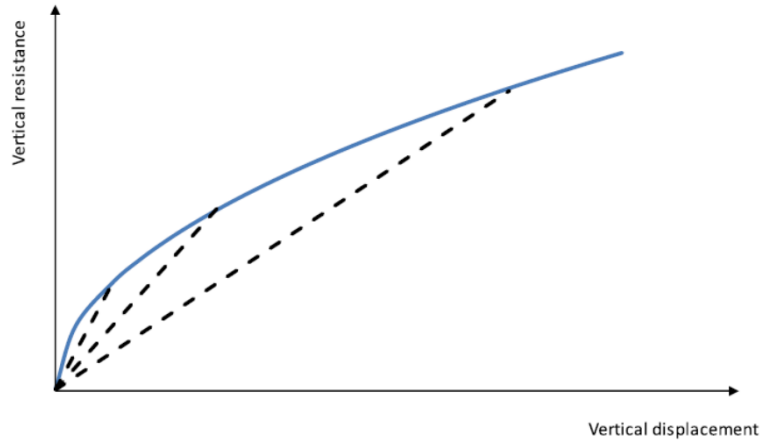
Figure 4.1: Examples of vertical static secant soil stiffness for different load levels [18].

4.1.2 Dynamic soil stiffness

Generally, an equivalent shear modulus of the soil can be used to evaluate its stiffness. The soil's shear strain amplitude, γ_c, determines the shear modulus G, which is characterized as a secant modulus. From the following expression, the shear modulus, G_{max}, for sands under minor strains can be derived as:

$$G_{max} = \frac{625}{0.3 + 0.7 \cdot e_s^2} \cdot \sqrt{\sigma_a \cdot \sigma_s}, \tag{4.2}$$

where σ_a is the atmospheric pressure, 100kPa, σ_s is the mean effective stress in the soil, and e_s is the void ratio. Considering clays, as a best estimate to laboratory test data, G_{max} may alternatively be found using the undrained shear strength s_u as:

$$\frac{G_{max}}{s_u} = \left(30 + \frac{300}{(I_p + 0.03)}\right) \cdot OCR^{-0.25}, \tag{4.3}$$

where I_p is the plasticity index (in absolute numbers) and OCR is the overconsolidation ratio of the clay. A typical curve of G/G_{max} versus γ_c is used to represent the relationship between the secant shear modulus G and the cyclic shear strain amplitude, γ_c, with a typical range as shown in Figure 4.2. Such relationships should be used cautiously, especially at high strains where it's crucial to prevent shear stresses above the shear strength.
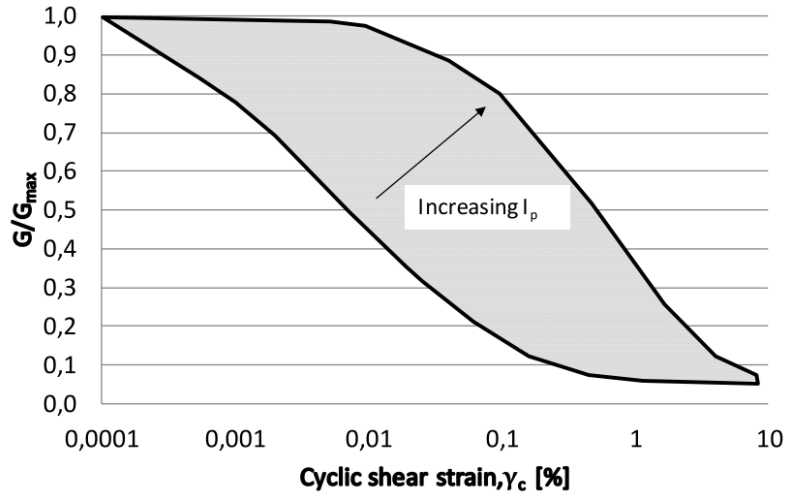
Figure 4.2: G/G_{max} as function of cyclic shear strain, typical range [18].

Keep in mind that different methods might also be used, and the models shown above serve as examples. Due to the complexity of the soil behaviour under dynamic loading, specialised analyses are needed. DNV-RP-C212 provides additional guidance on this. When evaluating G_{max} for a free spanning pipeline from Equation 4.2, the mean effective stress, σ_s, in the soil at the span support can be calculated at a given depth below the pipe. This depth may be assumed equal to a contact width B.

$$\sigma_s = \frac{1}{2} \cdot (1 + K_0) \cdot B \cdot \gamma' + \frac{V}{3 \cdot B} \cdot \left(1 + \frac{L}{2 \cdot L_{sh}}\right). \tag{4.4}$$

Here K_0 is the coefficient of earth pressure at rest, γ' is the submerged unit weight of soil, V is the submerged weight of the pipe per unit length, B is the pipe-soil contact width, L is the span length, and L_{sh} is the span support length at one shoulder. In the temporary phase that accompanies pipe laying, the clay may not have consolidated for the weight of the pipe, and should thus be considered when evaluating G_{max} for pipes on clay by Equation 4.3. The contact length between the pipe and the soil on one shoulder, or the span support length, L_{sh}, relies on the span length, the soil stiffness of the shoulders, the type of soil, the shoulder geometry, and the submerged weight and stiffness of the pipe. The vertical and lateral dynamic soil stiffness $K_{V,d}$ and $K_{L,d}$, can be determined from the following equations respectively:

$$K_{V,d} = \frac{0.88 \cdot G}{1 - \nu}, \tag{4.5}$$

$$K_{L,d} = 0.76 \cdot G \cdot (1 + \nu). \tag{4.6}$$

With the assumption of a pipe length equal to 10 times the contact breadth between the pipe and the earth and based on the elastic half-space theory for a rectangular foundation. For sand and clay, respectively, the Poisson's ratio, ν, ranges from 0.3 to 0.35 and 0.45 to 0.5. Finding a representative equivalent shear modulus for the elastic half-space is the key challenge.

4.1.3 Simplified static and dynamic soil stiffness

According to DNV-RP-F114, when the topographical conditions are simple, the soils are not stratified and homogenous, and no in-depth investigation has been performed to determine the soil stiffness, the vertical and lateral dynamic stiffness, $K_{V,d}$ and $K_{L,d}$ may be determined simply as follows:

$$K_{V,d} = \frac{C_V}{1-v} \cdot \left(\frac{2}{3} \cdot \frac{\rho_s}{\rho} + \frac{1}{3} \right) \cdot \sqrt{D}, \tag{4.7}$$

$$K_{L,d} = C_L \cdot (1+v) \cdot \left(\frac{2}{3} \cdot \frac{\rho_s}{\rho} + \frac{1}{3} \right) \cdot \sqrt{D}, \tag{4.8}$$

where D is the outer diameter of the pipe including coating, ρ_s/ρ is the specific mass ratio between the pipe mass (not including added mass) and the displaced water, and v is the Poisson's ratio. The coefficients C_V and C_L are provided in Tables 3.2 and 3.3 for various types of soil material. These tables also include suggested values for the vertical static soil stiffness.

Sand type	Friction angle, φ [°]	C_V [kN/m$^{5/2}$]	C_L [kN/m$^{5/2}$]	$K_{V,s}$ [kN/m/m]
Loose	28-30	10500	9000	250
Medium	30-36	14500	12500	530
Dense	36-41	21000	18000	1350

Table 4.1: Simplified dynamic stiffness factor and static stiffness for pipe-soil interaction in sand.

Clay type	Undrained shear strength, S_u [kN/m^2]	C_V [kN/m$^{5/2}$]	C_L [kN/m$^{5/2}$]	$K_{V,s}$ [kN/m/m]
Very soft	< 12.5	600	500	50-100
Soft	12.5-25	1400	1200	160-260
Firm	25-50	3000	2600	500-800
Stiff	50-100	4500	3900	1000-1600
Very stiff	100-200	11000	9500	2000-3000
Hard	> 200	12000	10500	2600-4200

Table 4.2: Simplified dynamic stiffness factor and static stiffness for pipe-soil interaction in clay.

To appropriately account for the implications of complex soil mobility, such as erosion and self-burial, the lateral dynamic stiffness should be calculated under the assumption of loose sand properties for free spans supported by sand. Typically, the axial dynamic stiffness is not significant. However, it is crucial to include an axial soil-support model with friction and stiffness when taking into account long free spans. The axial dynamic soil stiffness may be assumed to be equal to the lateral dynamic soil stiffness in the absence of data.

When designing a pipeline, it is important to take into account the capacity for the transfer of axial loads between the pipe and the surrounding soil. Axial frictional stresses may be present between the pipe

and soil and can be caused by residual stresses from the pipelay process. These stresses can extend over long distances from the point of separation between the pipe and soil on the shoulder of the free span.

The axial friction will be limited by the interface shear resistance. In areas where there is lateral movement of the pipe, such as on the shoulders near the free span, the available surface friction needs to be shared between axial and lateral stresses. This interaction can reduce both the axial and lateral resistance at the shoulders and should be taken into account during the design process.

4.2   Soil damping

Soil damping in free span assessments generally depends on the dynamic loads that the soil experiences. There are two types of soil damping mechanisms that can be distinguished according to *DNV-RP-F114: Pipe-soil interaction for submarine pipelines* [18]. The first is radiation damping, which is associated with the propagation of elastic waves through the yield zone. The second is material damping, which occurs close to the yield zone in contact with the pipe due to hysteresis effects.

When it comes to evaluating radiation damping, available solutions for elastic soils can be used with the relevant soil modulus reflecting the soil stress (or strain) levels. The frequency of the oscillations has a significant impact on radiation damping and is especially important for high-frequency oscillations. In general, soil material damping typically governs soil damping for free spanning pipelines. The modal soil damping ratio specific to the pipe-soil interaction for a given case, ζ_{soil}, is given by:

$$\zeta_{soil} = \frac{1}{4 \cdot \pi \cdot f_0} \cdot \left(\frac{\int_L c(s) \varphi^2(s) ds}{\int_L m(s) \varphi^2(s) ds} \right),$$

(4.9)

where $c(s)$ is the soil damping per unit length, which can be defined based on the energy balance between the maximum elastic energy stored by the soil during one oscillation cycle and the energy dissipated by a viscous damper during the same cycle. The equation can be solved by finite element analysis where discrete soil supports are used in the pipeline model. For support no. i, the viscous damping coefficient, c_i is given by:

$$c_i = 2 \cdot \zeta_{soil,i} \cdot \frac{k_i}{\omega},$$

(4.10)

where k_i is the linearized spring stiffness at support no. i, $\zeta_{soil,i}$ is the damping ratio for the same support, and ω is the angular frequency of the mode being considered. By knowing the non-linear hysteric reaction of a support length the damping ratio representing the support can be calculated as:

$$\zeta_{soil,i} = \frac{1}{4 \cdot \pi} \cdot \frac{E_{Dissipated}}{E_{Elastic}},$$

(4.11)

where $E_{Dissipated}$ is the energy dissipation at support no.i and $E_{Elastic}$ is the equivalent elastic energy at support no.i. See Figure 4.3.
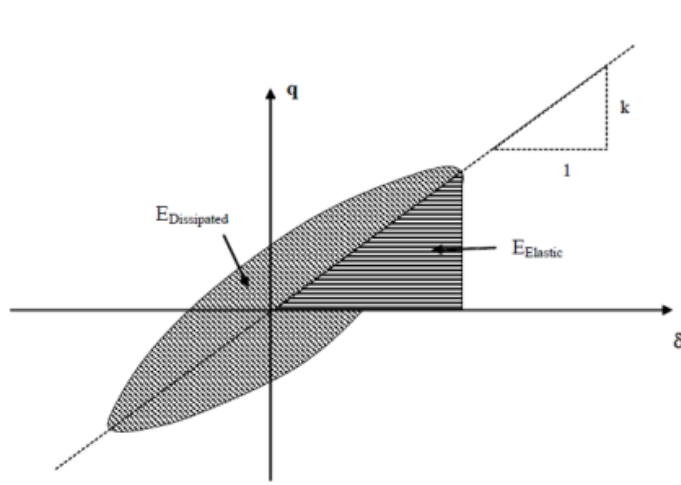
Figure 4.3: Energy dissipation at soil support, shown in the load-displacement space [18].

In pipeline design, it is important to consider the non-linearity of soil, as the equivalent spring stiffness and damping ratio are dependent on the displacements at the support. To determine the modal soil damping ratio for a specific case, it is necessary to take this into account, which requires an iterative solution to ensure compatibility between various dependencies:

- The dependency of the mode shape on the equivalent support springs.

- The dependency of the oscillation amplitude on the modal damping.

- The dependency of the equivalent springs and the damping ratio of the discrete soil supports on the cyclic support displacements.

- The dependency of the modal damping ratio on mode-shape and on support springs and damping ratio.

To perform these iterations, non-linear relationships for the spring stiffness (k_i) and damping ratio (ζ_i) as a function of pipe penetration and cyclic displacements for the relevant soil and pipe diameter are required. Figure 4.4 qualitatively illustrates such relationships, which can be determined either experimentally or analytically. These relationships serve as the basis for the iterative solution and help ensure accurate determination of the modal soil damping ratio. Simplified soil damping values can be found in the recommended practice if no detailed assessment has been performed.

Figure 4.4: Non-linear characteristics of soil stiffness and damping.

5 VIV assessment models

5.1 Response model in FatFree

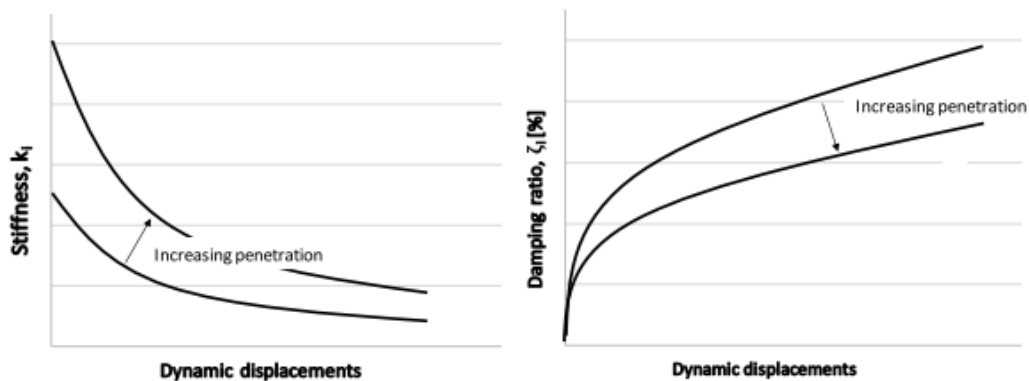FatFree software is used in the design, assessment, and reassessment of subsea pipeline spans in accordance with the response model in DNV-RP-F105 [11]. The software allows for the design of fatigue lifetimes for new free-spanning pipelines due to vortex-induced vibrations (VIV) and direct wave loading, as well as fatigue lifetime reassessment of existing pipelines. In the response-based model, possible excited modes are identified, and stress ranges resulting from VIV are calculated from mode shapes/curvatures obtained through Finite Element Analysis (FEA) and VIV response model curves. The curves are based on parametric equations developed from experiments to define response amplitudes for both the in-line (IL) and cross-flow (CF) direction, over a range of reduced velocities for different flow angles.

5.1.1 Formulation for pure in-line and cross-flow induced in-line response

The pure in-line vortex-induced vibration stress range $S_{IL,j}(x)$, can be calculated from:

$$S_{IL,j}(x) = 2 \cdot A_{IL,j}(x) \cdot \left(\frac{A_y}{D}\right)_j \cdot \Psi_{\alpha,IL} \cdot \gamma_s,$$ (5.1)

where $A_{IL,j}(x)$ is the unit diameter stress amplitude for IL mode j at location x, given by Equation 5.2. It is the stress caused by unit diameter IL mode shape deflection. $(A_y/D)_j$ is the normalised IL VIV response amplitude for mode j, $\Psi_{\alpha,IL}$ is a correction factor for current flow ratio $\alpha = U_c/(U_c + U_w)$, where U_c and U_w are current and wave velocity respectively. γ_s is a safety factor to be multiplied by the stress range.

$$A_{IL,j}(x) = (1 + CSF) \cdot D \cdot \kappa_{IL,j}(x) \cdot E \cdot r$$ (5.2)

In the equation above CSF is a concrete stiffening factor to be included if relevant, D is the outer diameter of the pipeline (including coating), $\kappa_{IL,j}(x)$ is the curvature of mode j for IL direction, E is Young's modulus, and r is the radial distance to the weld toe or weld root. As mentioned, the response model is highly dependent on empirical data, and values for $(A_y/D)_j$ to use in the stress calculation are given by Figure 5.1. The figure displays the IL VIV amplitude as a function of reduced velocity (including safety factors). γ_{on} is a safety criterion for onset values for the IL response, and the design stability parameter $K_{sd} = K_s/\gamma_k$, where γ_k is a safety factor. $R_{i\theta,1}$ and $R_{i\theta,2}$ are reduction functions between 0 and 1 accounting for the effect of turbulence intensity and angle of attack (in radians). For parametric equations for the model see [11].

To consider the potential for CF-induced IL VIV it is necessary to take into account all active CF modes. The IL-mode with an eigenfrequency closest to twice the oscillating frequency of the CF-mode with the largest response amplitude is the most likely candidate for CF-induced IL VIV. This candidate mode can be identified by finding the minimum value of the expression:

$$|f_{IL,k}^{part} - 2 \cdot f_{CF-RES,i}|,$$ (5.3)

where $f_{IL,k}^{part}$ is the natural frequency of the k-th participating IL-mode. Further, the stresses due to CF-induced IL VIV are found by:

$$S_{IL-CF}(x) = 0.8 \cdot A_{IL,k}(x) \cdot \left(\frac{A_z}{D}\right)_{max} \cdot R_k \cdot \gamma_s, \tag{5.4}$$

where $A_{IL,k}$ is the unit diameter amplitude of the selected candidate mode, $(A_z/D)_{max}$ denoted the maximum normalized response amplitude obtained from the CF response model. If the candidate mode for CF-induced IL VIV is an active IL mode, the stress for IL VIV is determined as the maximum value between stresses resulting from CF-induced IL VIV and pure IL VIV. However, if the candidate mode is not among the active modes, it is added as a new active mode with its stress range. Further, the combined IL stress range can be calculated using the formula:

$$S_{comb,IL}(x) = \sqrt{\sum_{j=1}^{m_{avg}} (S_{IL,j}(x))^2}, \tag{5.5}$$

where $S_{IL,j}$ is the response stress range due to j-th contributing IL mode, m_{avg} is equal to the number of contributing modes m if the CF-induced IL mode is among these. Otherwise, it is equal to $m+1$. Finally, the IL cycle-counting frequency is given by:

$$f_{cyc,IL}(x) = \sqrt{\sum_{j=1}^{m_{avg}} \left(f_{IL,j} \cdot \frac{S_{IL,j}(x)}{S_{comb,IL}(x)}\right)^2}, \tag{5.6}$$

where $f_{IL,j}$ is the natural frequency of the j-th contributing IL mode. For the CF-induced IL mode, this is set to $2 \cdot f_{CF-RES,i}$.
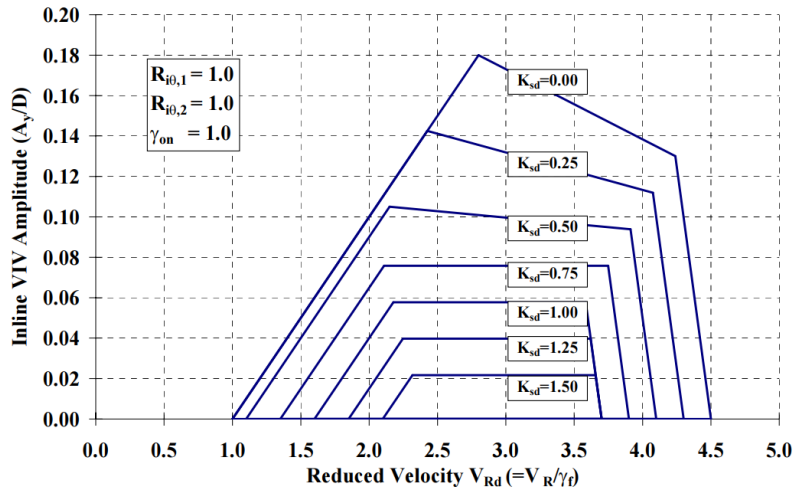

Figure 5.1: Illustration of in-line VIV response amplitude [19]. (A_y/D) is defined as the maximum in-line VIV response amplitude (normalized with D) as a function of V_{Rd} and K_{Sd}. For parametric formulas for the response model see [11].

5.1.2 Formulation for cross-flow response

Similar to the in-line response model, a stress range due to VIV from combined current and wave flow can be established by the following equation:

$$S_{CF,i}(x) = 2 \cdot A_{CF,i}(x) \cdot \left(\frac{A_z}{D}\right)_i \cdot R_k \cdot \gamma_s, \tag{5.7}$$

where $A_{CF,i}$ is the unit diameter stress amplitude for CF mode i at location x, given by Equation 5.8. It is the stress due to unit diameter CF mode shape deflection. $(A_z/D)_i$ is the normalized CF vortex-induced vibration response amplitude for mode i given in Figure 5.2, R_k is an amplitude reduction factor due to damping and γ_s is a safety factor for the stress range. The cross-flow response model is also clearly dependent on the Keulagen Carpenter number (KC) and the current flow ratio, with a maximum response $A_z/D = 1.3$. In addition, it is dependent on multiple onset correction factors such as for seabed proximity $\Psi_{proxi,onset}$, trench geometry $\Psi_{trench,onset}$, specific mass (gravity) of pipe $\Psi_{mass,onset}$, and at last current to wave ratio $\Psi_{\alpha,onset}$. For parametric formulas for the response model see [11].

$$A_{CF,i}(x) = (1 + CSF) \cdot D \cdot \kappa_{CF,i}(x) \cdot E \cdot r. \tag{5.8}$$

The combined stress range from all active modes is given by:

$$S_{comb,CF} = \sqrt{\sum_{j=1}^{m} \left(S_{CF,j}(x)\right)^2}, \tag{5.9}$$

where m is the number for active modes. In order to determine the appropriate cycle-counting frequency for CF VIV, it is necessary to make a correction to the added mass coefficient. This is because the added mass coefficient varies as the structure oscillates. The corrected added mass coefficient, denoted as $C_{a,CF-RES}$, can be obtained in the recommended practice and used to correct the CF response frequency:

$$f_{CF-RES,j} = f_{CF,j} \sqrt{\frac{s_g + C_a}{s_g + C_{a,CF-RES}}}, \tag{5.10}$$

where $f_{CF,j}$ is the CF response frequency without correction, s_g is the specific gravity of the pipeline and can be calculated by $(q+b)/b$, where q represents the submerged weight and b represents the buoyancy. Additionally, the still-water added mass coefficient is denoted C_a and $C_{a,CF-RES}$ is the added mass coefficient due to CF response. At last, the CF cycle-counting frequency is found by:

$$f_{cyc,CF}(x) = \sqrt{\sum_{j=1}^{m} \left(f_{CF-RES,j} \cdot \frac{S_{CF,j}(x)}{S_{comb,CF}(x)}\right)^2}. \tag{5.11}$$
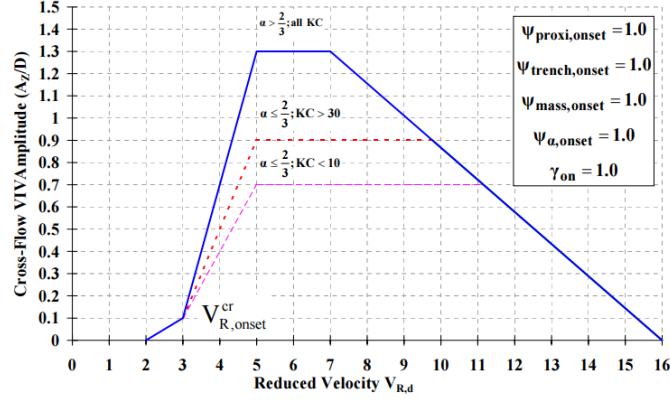
Figure 5.2: Illustration of cross-flow VIV response amplitude [19]. The figure provides characteristic maximum values of the normalized response. For parametric formulas for the response model see [11].

5.1.3 Fatigue damage

The response model produces two combined stress ranges $S_{comb,CF}$ and $S_{comb,IL}$ as mentioned above, which accounts for all the stresses related to a particular load case. The cycle-counting frequency associated with each stress range is used to determine the number of cycles per year. By using the combined stress ranges as input to an SN-curve for the pipeline cap and root position, the number of cycles to failure can be determined. The total damage caused by CF VIV and IL VIV can then be calculated by adding their respective damages.

5.2 Time-domain force model in SIMLA

Strip theory serves as the foundation for the time domain VIV model implemented in SIMLA. It is described by the incoming flow vector **u**, the cylinder response vector **x**, and the hydrodynamic coefficients. Figure 5.3 illustrates the cylinder in a local coordinate system. The incoming flow vector can be decomposed into a normal component **u_n**, and a tangential component **u_t** to the cylinder strip. When considering only the normal component, the hydrodynamic loads and structural response can be simplified into a two-dimensional problem. That is, in the **j₁j₂**-plane with **j₃** being in the axial direction of the local coordinate system. This is the system that the drag force and vortex shedding forces follow, and where **j₁** is parallel to the relative flow velocity vector, **v_n** = **u_n** − **ẋ**. Obviously, the shedding forces will change direction as the relative flow changes, so cross-flow or in-line direction will be referred in the local coordinate system in the present text. The hydrodynamic force model is expressed in Equation 5.12 by Ulveseter et al. [20].

$$
\boldsymbol{F_n} = \underbrace{C_M \rho \frac{\pi D^2}{4} \boldsymbol{\dot{u}_n}}_{\text{Froude-Kriloff force}} \underbrace{- (C_M - 1) \rho \frac{\pi D^2}{4} \boldsymbol{\ddot{x}_n}}_{\text{Inertia force}} + \underbrace{\frac{1}{2} \rho D C_D |\boldsymbol{v_n}| \boldsymbol{v_n}}_{\text{Drag force}}
$$

$$
\underbrace{\phantom{F_n = C_M \rho \frac{\pi D^2}{4} \dot{u}_n - (C_M - 1) \rho \frac{\pi D^2}{4} \ddot{x}_n + \frac{1}{2} \rho D C_D |v_n| v_n}}_{\text{Morison's equation}}
$$

$$
+ \underbrace{\frac{1}{2} D C_{v,x} |\boldsymbol{v_n}| \boldsymbol{v_n} cos\phi_{exc,x}}_{\text{In-line vortex shedding force } (\boldsymbol{F_{v,x}})} + \underbrace{\frac{1}{2} \rho D C_{v,y} |\boldsymbol{v_n}| \left(\boldsymbol{j_3} \times \boldsymbol{v_n}\right) cos\phi_{exc,y}}_{\text{Cross-flow vortex shedding force } (\boldsymbol{F_{v,y}})}.
$$

(5.12)

The three first terms are the well-known Morison's equation that is applicable in cases where the ratio of

wavelength to cylinder diameter is larger than 5, and when waves are not breaking. This is, in general, true for slender structures such as pipelines, risers and cables. In the equation C_M is the inertia coefficient, C_D is the drag coefficient, while D and ρ er cylinder diameter and fluid density respectively. The two last terms are the vortex shedding forces, in the in-line and cross-flow direction and with $C_{v,x}$ and $C_{v,y}$ as their respective shedding force coefficients. The instantaneous phases of the vortex shedding forces are decided by $\phi_{exc,x}$ and $\phi_{exc,y}$.
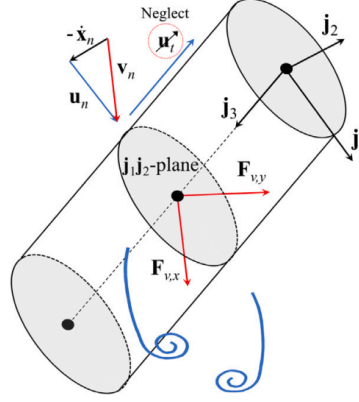

Figure 5.3: A cylinder strip with the relevant vectors and local coordinate system for the TD-VIV force model [21].

The shedding force coefficients $C_{v,x}$ and $C_{v,y}$ determine the magnitude of the vortex shedding forces, while the instantaneous phases $\phi_{exc,x}$ and $\phi_{exc,y}$ which varies in time makes them oscillate. Synchronization models are applied to each direction to ensure that the instantaneous frequency of the vortex-shedding force can increase or decrease so that its phase can match the instantaneous phase of the cylinder velocity. That is what simulates the lock-in phenomenon associated with vortex-induced vibrations. Synchronization is only allowed to take place when in a non-dimensional frequency range, i.e. the synchronization range. For cross-flow direction, Equation 5.14 can be used to express the instantaneous vortex shedding frequency.

$$\dot{\phi}_{exc,y} = \frac{d\phi_{exc,y}}{dt} = 2\pi f_{exc,y} = \frac{2\pi|\mathbf{v_n}|}{D}\hat{f}_{exc,y}. \tag{5.13}$$

$$\hat{f}_{exc,y} = \begin{cases} \hat{f}_{0,y} + (\hat{f}_{max} - \hat{f}_{0,y})\sin\theta_y, & \theta_y \geq 0 \\ \hat{f}_{0,y} + (\hat{f}_{0,y} - \hat{f}_{min})\sin\theta_y, & \theta_y < 0. \end{cases} \tag{5.14}$$

Here $\hat{f}_{min,y}$ and $\hat{f}_{max,y}$ is the synchronization range for cross-flow and $\hat{f}_{0,y}$ is the non-dimensional maximum energy transfer frequency. θ_y is the phase difference between cylinder cross-flow velocity and the corresponding cross-flow shedding force, $\theta_y = \phi_{\dot{y}rel} - \phi_{exc,y}$. More specifically, this means that lock-in occurs for $\hat{f}_{min,y} \leq \hat{f}_{exc,y} \leq \hat{f}_{max,y}$, and when $\hat{f}_{exc,y} = \hat{f}_{0,y}$ the vortex-induced cross-flow excitation force is in phase with the cylinder's cross-flow velocity, i.e. $\theta_y = 0$.

There are two types of in-line responses. The first occurs at lower current speeds and is known as the pure in-line response, and a model for this response was first introduced by Ulveseter et al. [22] in 2017. The other one is the cross-flow induced in-line response which occurs at higher current speeds. For the cross-flow induced in-line response, two different models have been proposed for the synchronization

process. The first one by Ulveseter et al. [20] in 2018 and the second one more recently by Kim et al. [21] in 2021. With regards to the first one, the idea behind it is that it is based on a trend shown in experimental data, where the IL VIV frequency usually is two times the achieved CF VIV frequency. That is, $\dot{\phi}_{exc,x}$ can be established as a function of $\dot{\phi}_{exc,y}$ and the instantaneous phase difference between the phase of the relative in-line velocity of the cylinder $\phi_{\dot{x}_{rel}}$, versus the instantaneous phase of the in-line excitation force:

$$\dot{\phi}_{exc,x} = 2\pi \dot{\phi}_{exc,y}[1 + \alpha \sin(\phi_{\dot{x}_{rel}} - \phi_{exc,x})], \tag{5.15}$$

where α tells the amount of frequency of the in-line response depending on the cross-flow force. The second synchronization model for the cross-flow induced in-line vibrations was developed due to inaccurate results by the model above in the Hanøytangen test [21]. In fact, this updated model is exactly the same as the one proposed by Ulveseter in 2017.

$$\dot{\phi}_{exc,x} = \frac{d\phi_{exc,x}}{dt} = 2\pi f_{exc,x} = \frac{2\pi |\mathbf{v_n}|}{D} \hat{f}_{exc,x}. \tag{5.16}$$

$$\hat{f}_{exc,x} = \begin{cases} \hat{f}_{0,x} + (\hat{f}_{max} - \hat{f}_{0,x}) \sin\theta_x, & \theta_x \geq 0 \\ \hat{f}_{0,x} + (\hat{f}_{0,x} - \hat{f}_{min}) \sin\theta_x, & \theta_x < 0. \end{cases} \tag{5.17}$$

Again $\hat{f}_{min,x}$ and $\hat{f}_{max,x}$ is the synchronization range for pure in-line and $\hat{f}_{0,x}$ is the non-dimensional maximum energy transfer frequency. θ_x is the phase difference between cylinder in-line velocity and the corresponding in-line shedding force, $\theta_x = \phi_{\dot{x}rel} - \phi_{exc,x}$. More specifically, this means that lock-in occurs for $\hat{f}_{min,x} \leq \hat{f}_{exc,x} \leq \hat{f}_{max,x}$, and when $\hat{f}_{exc,x} = \hat{f}_{0,x}$ the vortex-induced in-line excitation force is in phase with the cylinder's in-line velocity, i.e. $\theta_x = 0$. The basic idea is that the pure IL-induced force component and the IL force component associated with the simultaneous presence of CF VIV can both be predicted using the same synchronization model. By selecting a sufficiently wide synchronization range, it should be possible to simulate both pure in-line and cross-flow induced in-line vibrations using the same synchronization model.

6 Fatigue

6.1 Rainflow Counting

Cumulative damage analysis is an important aspect of structural reliability and safety, as it allows engineers to predict the likelihood of failure and estimate the remaining life of a system (Berge and Ås [23]). Rainflow counting is particularly useful in this context, as it allows for the consideration of both the amplitude and the number of cycles of a given stress level. This can provide a more accurate estimate of damage than methods that only consider the stress amplitude. Rainflow counting is a commonly used method for cumulative damage analysis in mechanical systems, such as subsea pipelines and other offshore structures under dynamic loading. The method is based on the concept of "rainflow cycles," which are defined as the number of stress cycles between a given minimum and maximum stress level. The rainflow counting algorithm is used to identify and count these cycles, which can then be used to estimate the total damage to a system over time.

The rainflow counting algorithm is implemented by first sorting the stress history data in descending order. The algorithm then identifies local maxima and minima in the stress time history, and the range between these extrema is used to define the rainflow cycles. The cycles are then grouped into "bins," based on their range, and the number of cycles in each bin is counted. This information can then be used to estimate the damage to the system using a damage accumulation model, such as the Palmgren-Miner linear damage rule. The algorithm is designed to identify and count cycles in a material's stress-strain response. This is achieved by analyzing the strain history, as illustrated in Figure 6.1 and the corresponding stress-strain path. The individual cycle 2-3-2 does not affect the remainder of the stress-strain history, and each time a hysteresis loop is closed, a cycle count is made.
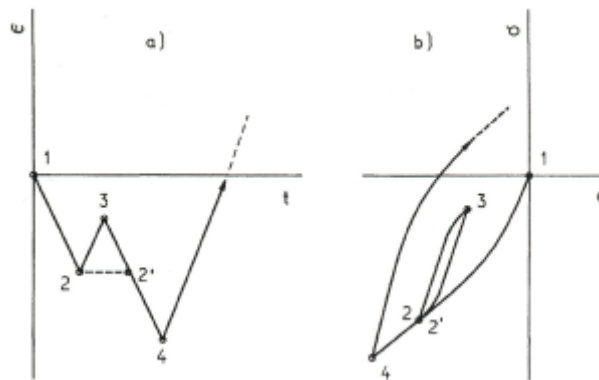

Figure 6.1: Part of a strain history (a) and the stress-strain response (b). The Rainflow counting method counts small cycles within large cycles similar to the way closed hysteresis loops are formed. The cycle count is thus reflecting the way in which the material is responding. Berge and Ås [23].

The rainflow counting method gets its name from the analogy of rain falling down a pagoda roof, as shown in Figure 6.2. The strain history in this figure is more complex than in Figure 6.1, but the concept is the same. The rules for rainflow counting are as follows:

1. Rain initiates at the inside of each peak or valley and drips down when it reaches the edge.

2. A cycle is completed when the rain meets another flow from above.

3. The flow stops when it comes opposite a more positive peak (starting from a peak) or a more negative valley (starting from a valley) than the one from which it started.
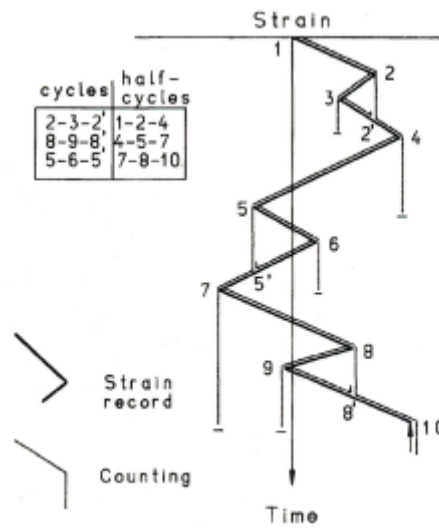

Figure 6.2: Illustration of the pagoda roof rainflow analogy. Berge and Ås [23].

By following these rules, it can be verified that this counting procedure reproduces the cyclic stress-strain loops of the material undergoing the same loading history. The closed stress-strain loops, known as hysteresis loops, represent energy dissipated due to dislocation movements in the material. The fatigue damage caused by a closed loop in a variable amplitude loading history is equivalent to the damage caused by a cycle in a constant amplitude fatigue test with the same stress range. However, residual half-cycles that cannot be paired up with other half-cycles to form complete loops cannot be determined with this approach. Rainflow counting is recommended for wide-band loading, but for narrow-band loading, all the counting procedures will yield similar results. It's important to note that unless the load history starts with its most positive peak or its most negative valley, a rainflow count may give a number of unpaired half cycles that are difficult to handle in cumulative damage analysis. Additionally, when applied to cracked specimens where crack closure may occur under compressive loading, rainflow counting loses its physical significance. The choice of method for cycle counting in fatigue analysis becomes important only when the design is based on actual load-time history. These histories can come from various sources such as recorded loads or stresses from an actual structure, simulated load histories from model experiments, or computer-generated time histories.

6.2   Palmgren-Miner linear damage rule

The Palmgren-Miner linear damage rule is based on the concept of "damage," which is defined as the ratio of the accumulated fatigue damage to the total damage that would cause failure. It is a widely used method for calculating fatigue damage in marine structures. The method is based on the principle that the damage accumulated by a structure due to fatigue loading is the sum of the damage caused by each individual loading cycle. It uses a damage index, which is a function of the stress range and the number of cycles at that stress range. The damage index is then multiplied by the number of cycles at each stress range to obtain the damage for that stress range. The total damage is obtained by summing up the damage for all stress ranges. The Palmgren-Miner linear damage rule is given by the following

formula (Berge and Ås [23]):

$$D = \sum_i \frac{n_i}{N_i}.$$ (6.1)

The total accumulated damage D is described by the number of cycles n_i for a corresponding stress range $\Delta\sigma_i$, and the number of cycles until failure, N_i. The relationship between the number of cycles until failure N_i, and the stress range $\Delta\sigma_i$ can be represented by an SN-curve using the material parameters m and log A.

$$\log N_i = log A - m \log \Delta\sigma_i$$ (6.2)

The traditional SN-curve is based on the assumption of constant amplitude loading and is used to predict the fatigue life of a material under such conditions. Haibach extrapolated SN-curves are a specific type of SN-curve that is used to predict the fatigue life of marine structures, such as subsea pipelines, that are subjected to vortex-induced vibrations. These structures experience cyclic loading with varying amplitudes caused by the vortex shedding phenomenon, which results in a fatigue life that is significantly shorter than structures with constant dynamic loading. Haibach extrapolation method is a statistical method which is a way to estimate the number of cycles to failure at very high numbers of cycles.
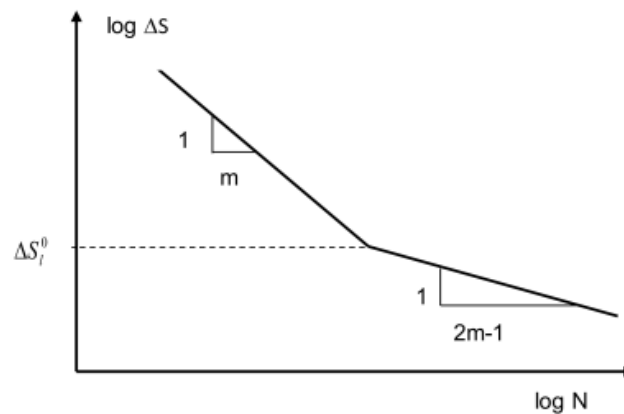

Figure 6.3: Haibach extrapolated SN-curve for cumulative damage calculations. Berge and Ås [23].

7 Case description

A realistic seabed profile, taken from a field measurement survey, is shown in Figure 7.1. The figure displays a 3.6km seabed route with a pipeline in empty lay condition. It is located at water depths spanning between approximately 867 and 842 meters and the pipeline direction in degrees relative to the geographic north is 165.51° as shown in Figure 7.2. The design life for the pipeline is 25 years. Data for the case scenario has been provided by Reinertsen New Energy.
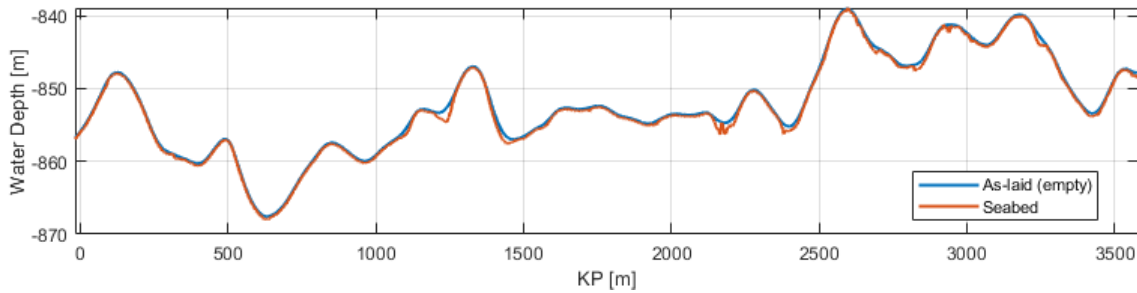

Figure 7.1: Illustration of realistic seabed profile containing multiple spans and showing pipeline lay in empty condition. KP is the kilometre point (curvilinear distance).
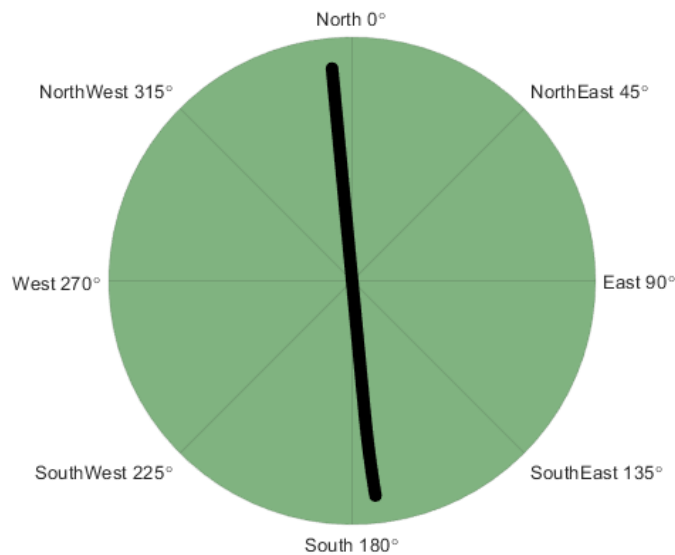

Figure 7.2: Illustration of pipeline direction relative to geographic north.

A previously performed free span assessment has been done for the multi-span scenario above, including all the pipeline conditions mentioned in Section 3. That includes static-, modal-, and VIV analysis based on the response model recommended in *DNV-RP-F105: Free Spanning Pipelines* [11]. The most critical spans and their corresponding VIV fatigue damage (yearly rate), as well as information about pipeline conditions, free span lengths and effective axial forces, are given in Table 7.1. Operation B-25 means the operational condition in the year 2025, which also is the start-up year for this pipeline. Likewise, B-31 refers to the operational condition in the year 2031. In this thesis, the free span at KP Value 600m with a span length of 189m is chosen as the case scenario. The model in Figure 7.1 has been "cut" at 300m and 1000m in order to isolate the free span and to perform a new VIV assessment with the response-based model and the newly developed TD-VIV force model.

KP Value [m]	Condition	Free Span Length [m]	Effective axial force [kN]	Damage/year (in-line)	Damage/year (cross-flow)
1100	Operation B-31	39	-400	5.67E-04	-
1100	Shutdown	49	1000	1.17E-02	-
3250	Operation B-25	57	-300	1.02e-03	-
3250	Operation B-31	58	30	3.42E-04	-
600	Shutdown	189	1150	-	8.50E-04
2200	Shutdown	109	915	-	4.54E-03

Table 7.1: Previous free span assessment results by Reinertsen New Energy based on the response model recommended in DNV-RP-F105.

7.1 Environmental condition

7.1.1 Current condition

Provided current data for the pipeline's location was used to create the 3D histogram plot in Figure 7.3, which represents the probability of occurrence of currents from different directions and velocities. The plot shows the most common current direction falls between 0 and 90 degrees relative to the geographic North, and the highest probability of occurrence between 0.05 and 0.35m/s. Additionally, the plot can be used to identify less common current directions and velocities that may still have a significant impact on structural loads. The histogram data is used as input directly into FatFree, which returns some key statistical data and extreme values as shown in Table 7.2. In SIMLA, the current velocities and directions have been used to model current profiles for the time-domain analysis as described later in Section 8.3, and the probability of occurrence has been used for the fatigue damage calculations.
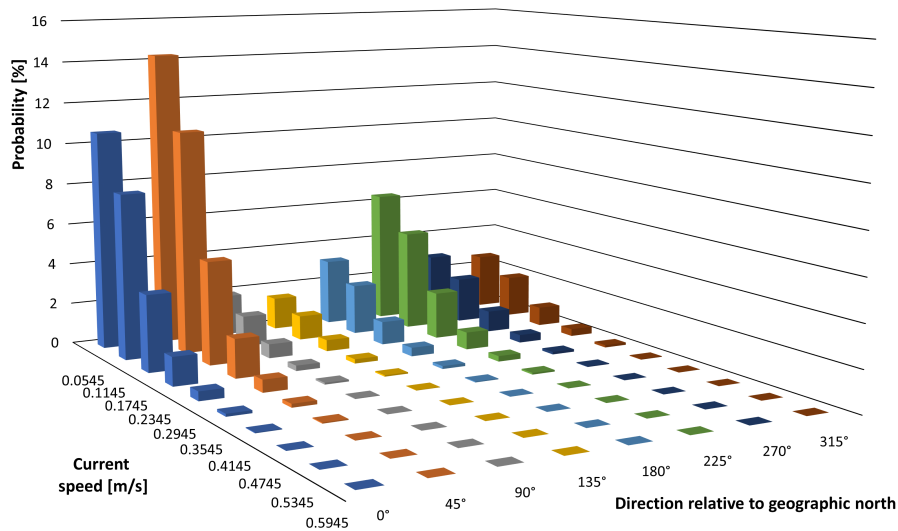

Figure 7.3: Current condition histogram.

	0 °	45 °	90 °	135 °	180 °	225 °	270 °	315 °
Probability	0.24	0.33	0.04	0.04	0.07	0.15	0.07	0.06
Mean value [m/s]	0.11	0.11	0.11	0.11	0.11	0.11	0.11	0.11
1 year [m/s]	0.445	0.445	0.325	0.325	0.385	0.385	0.385	0.385
10 year [m/s]	0.505	0.505	0.445	0.445	0.445	0.505	0.445	0.445
100 year [m/s]	0.625	0.625	0.565	0.505	0.565	0.565	0.565	0.565

Table 7.2: Key statistical data and extreme values from current condition histogram.

7.1.2 Seabed geotechnical properties

Pipe-soil parameters are provided and the route consists mainly of very soft clay, with some smaller sections of outcropped stiff clay. The static soil parameters given by Reinertsen New Energy states an axial friction coefficient in the range of 0.25-0.40, a lateral friction coefficient of 0.6-1.0, and a vertical stiffness of 20-40kN/m/m. Further, the estimated range in the dynamic stiffness for the soil on free span shoulders is 600-1400kN/m/m in the vertical direction and 350-800kN/m/m in the lateral direction. Based on this, simplified soil stiffness and damping values according to DNV-RP-F115 and given in Table 7.3 have been chosen for the case scenario.

Description	Symbol	Unit	Value
Vertical, static soil stiffness	$K_{V,s}$	kN/m/m	30.0
Vertical, dynamic soil stiffness	$K_{V,d}$	kN/m/m	1000
Lateral, dynamic soil stiffness	$K_{L,d}$	kN/m/m	600
Soil damping ratio (in-line)	$\zeta_{soil,IL}$	-	0.010
Soil damping ratio (cross-flow)	$\zeta_{soil,CF}$	-	0.010

Table 7.3: Pipe-soil parameters.

7.2 Pipeline data

7.2.1 Pipe geometry

The characteristic data for the pipeline geometry is summarized in Table 7.4.

Description	Symbol	Unit	Value
Steel wall internal diameter	D_{si}	m	0.4064
Steel wall outer diameter	D_{so}	m	0.4572
Outer diameter (coating included)	OD	m	0.4732
Steel wall thickness	t_s	m	0.0254
Coating thickness	t_c	m	0.008
Second moment of area	I	m^4	0.0121

Table 7.4: Characteristic data for pipeline geometry.

7.2.2 Material

The pipeline material data is summarized in Table 7.5.

Description	Symbol	Unit	Value
Young's Modulus	E	MPa	2.07×10^5
Shear Modulus	G	MPa	9.62×10^3
Axial stiffness	EA	kN	7.1×10^6
Bending stiffness	EI	kNm^2	1.67×10^5
Torsional stiffness	GJ	kNm^2	1.55×10^4
Poisson's ratio	ν	-	0.3
Steel density	ρ_s	kg/m^3	7850
Dry Weight (air-filled)	m	kg/m	281
Thermal expansion coefficient at 20°C	α	$°C^{-1}$	1.17×10^{-5}
Specified Minimum Yield Strength (SMYS) at 20°C	σ_y	MPa	450
Specified Minimum Tensile Strength (SMTS) at 20°C	σ_u	MPa	535

Table 7.5: Pipeline material data.

7.2.3 SN-curves

The Haibach SN-curves and SCFs for cap (outside) and root (inside) position of pipeline which are used in the VIV fatigue analysis are given in Table 7.6. These applies to all pipeline conditions. The SN-curve for cap position is a standard class E curve for an object in seawater with cathodic protection. The curve for the root position is a "F1-custom" curve provided by Reinertsen New Energy.

Parameter	Cap Position	Root Position
m_1	3	3
m_2	5	5
$Log(C_1)$	11.610	11.222
$Log(C_2)$	15.350	14.832
$\log N_{SW}$	6.00	5.81
SCF	1.197	1.046

Table 7.6: SN-curves and SCFs for cap and root position.

8   SIMLA model

8.1   Structural model

In this study, SIMLA was utilized for the analysis of the free span scenario. SIMLA is a powerful finite element method/analysis (FEM/FEA) tool that can handle pipe-laying analysis while taking into account non-linear material and contact behaviour, as well as large deformations. The behaviour of a FEM model for dynamic analysis can be described by the equation of motion on matrix form:

$$\mathbf{M\ddot{r}} + \mathbf{C\dot{r}} + \mathbf{Kr} = \mathbf{R}, \tag{8.1}$$

where $\mathbf{M}$ is the consistent mass matrix of the system, $\mathbf{C}$ is the damping matrix of the system, $\mathbf{K}$ is the stiffness matrix of the system and $\mathbf{R}$ is the external nodal loads. $\mathbf{r}$ and its derivatives are the nodal displacements, velocities and accelerations respectively. The structural damping model was established using the Rayleigh damping formulation, where the damping matrix is determined through a linear combination of the global mass and stiffness matrices (Ivar Langen [24]):

$$\mathbf{C} = \alpha_1 \mathbf{M} + \alpha_2 \mathbf{K}, \tag{8.2}$$

where the coefficients α_1 and α_2 are used to represent the mass-proportional and stiffness-proportional damping, respectively. Rayleigh damping formulation is a widely used method for modelling structural damping in linear dynamic systems. One of the key advantages of this approach is its computational convenience in implementing and specifying the damping level. Another significant feature of this method is that it results in a damping matrix that is orthogonal with respect to the eigenvectors. Although Rayleigh damping is typically used for linear dynamic systems, it can also serve as a reference for nonlinear dynamic systems. Taking use of the orthogonal properties and on normal form, the damping is often expressed as a damping ratio:

$$\lambda_i = \frac{1}{2}\left(\frac{\alpha_1}{\omega_i} + \alpha_2\omega_i\right), \tag{8.3}$$

where $\alpha_1 = 0$ gives damping ratio proportional to the eigenfrequency ω_i and $\alpha_2 = 0$ gives damping ratio inversely proportional to ω_i. To prevent unphysical structural damping caused by rigid body motions, the damping term proportional to the mass matrix is typically excluded, with α_1 set to 0. This approach was for the model. As a result, the only remaining term is $\alpha_2\mathbf{K}$, which is stiffness-proportional damping which corresponds to a modal damping ratio of $\lambda_i = \frac{\alpha_2\omega_i}{2}$. Further, α_2 was set to 0.05 using Equation 8.3 with the fundamental cross-flow frequency and a structural damping ratio of 0.005. This structural damping ratio was also used in the FatFree software. Note that α_2 has a level of uncertainty to it and can therefore be a source of error in the result. More extensive research should be performed numerically or experimentally to find appropriate values for the model.

The 3D beam element PIPE31 was used in SIMLA to model the pipeline with linear material properties and constant axial strain and torsion. To determine the optimal balance between result accuracy and simulation length, a convergence analysis was conducted by varying the element length in the model. The findings of the investigation indicate an optimal element length of approximately 0.61m. The pipeline was fixed against translational movements in all directions and free to rotate about the y- and z-axis at one end node. At the other end node, it was fixed for translational movement in y- and

z-direction, and free in the x-direction due to the application of effective axial force. Further, the same constraints for rotation were used for this node as for the previous. This approach ensures that the model can accurately capture the realistic behaviour of the pipeline under the given operational conditions. Note that two smaller spans at each side of the major span are included in the model. This was modelled to account for the effects of multiple spans on the pipeline shoulder. The model and its global coordinate system are displayed in Figure 8.1.
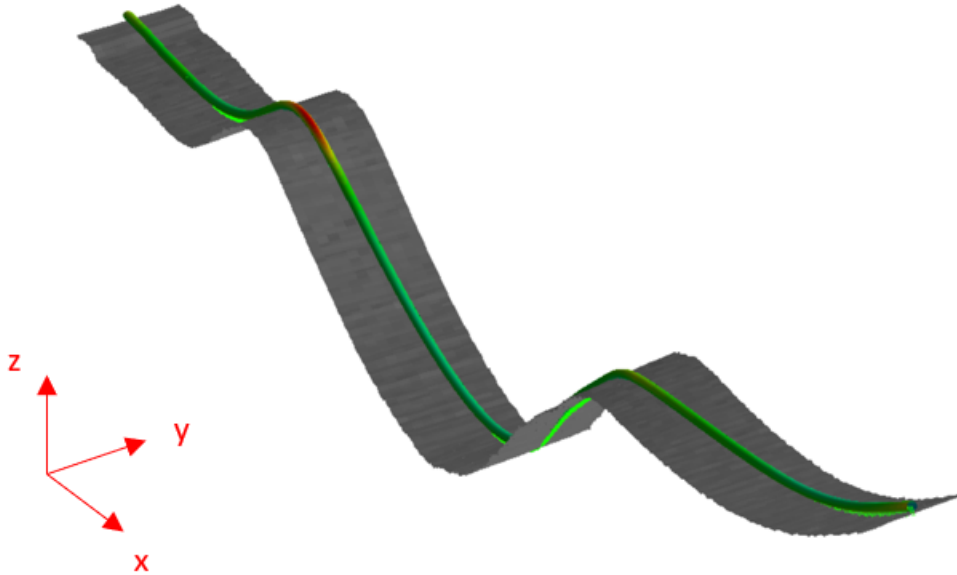
Figure 8.1: Structural model in SIMLA.

8.2 Hydrodynamic properties

As previously discussed, a time domain analysis is necessary to account for the non-linearities inherent in a realistic vortex-induced vibration scenario. Therefore, the updated synchronization load model for combined cross-flow and in-line VIV proposed by Kim, which was extensively studied in Section 5.2, was employed. To apply this time domain VIV model, suitable empirical coefficients for hydrodynamic drag, added mass, and vortex-induced excitation force had to be selected. Generally, these coefficients rely on parameters such as the Reynolds number, surface roughness (which was not considered in this study since the pipeline under examination is assumed to be smooth), and Keulegan-Carpenter number (KC).

In SIMLA, the element properties are defined by the ELPROP card which e.g. takes in two components for the hydrodynamic drag coefficient. That is a normal/radial component that has a significant contribution to the response, and which is strongly connected to Reynolds number. Assuming a smooth pipe and that the Reynolds number is within the sub-critical flow regime, this value is typically set to 1.2. The second contribution to the hydrodynamic drag coefficient is the tangential component, which represents skin friction and is typically negligible for pipelines due to their smooth surfaces and high Reynolds number.

In addition to the normal and tangential components of the hydrodynamic drag coefficient, the added mass coefficient is also an important factor used as input in the ELPROP card. For smooth cylinders, the normal/radial added mass coefficient of a circular cross-section is typically assumed to have a value

of 1.0. However, in real-world scenarios, the added mass coefficient may vary depending on several factors as mentioned in Section 2.2, where it can be seen that it is clearly a function of the reduced velocity and hence the vibration frequency. The tangential component of the added mass coefficient is typically considered negligible for practical applications. This is because the tangential motion of the fluid particles along the surface of a smooth cylinder is generally much smaller than the normal motion, resulting in a relatively small contribution to the added mass coefficient.

Further element properties can be defined by the HYDROPRO card, which is used to specify specific hydrodynamic properties such as parameters for the TD-VIV *ALLVIV* model used in this study to describe both cross-flow and in-line vortex-induced vibrations. The determination of suitable excitation force coefficients and synchronization parameters for practical applications is an ongoing field of research for the model, and the parameters chosen in the case scenario were default values from the SIMLA user manual [25], which are shown in Table 10.2.

Description	Symbol	Unit	Value
Quadratic drag coefficient in normal direction	C_{Dn}	-	1.2
Quadratic drag coefficient in tangential direction	C_{Dt}	-	0.1
Added mass coefficient in normal direction	C_{An}	-	1
Added mass coefficient in tangential direction	C_{At}	-	0.1
Cross-flow vortex shedding coefficient	$C_{v,y}$	-	1.0
In-line vortex shedding coefficient	$C_{v,x}$	-	0.8
Maximum cross-flow energy transfer frequency	$\hat{f}_{0,y}$	-	0.18
Minimum cross-flow synchronization range	$\hat{f}_{min,y}$	-	0.125
Maximum cross-flow synchronization range	$\hat{f}_{max,y}$	-	0.3
Maximum in-line energy transfer frequency	$\hat{f}_{0,x}$	-	0.5
Minimum in-line synchronization range	$\hat{f}_{min,x}$	-	0.3
Maximum in-line synchronization range	$\hat{f}_{max,x}$	-	0.7

Table 8.1: Default hydrodynamic parameters used in the TD-VIV model in SIMLA.

8.3 Modelling of current condition

In order to model realistic current conditions, several current profiles along the seabed profile were modelled for the free span case scenario. The seabed elevation can cause variations in current velocity at different locations of the span, so there can exist multiple vortex-induced vibration frequencies. Fatigue damage is a function of the number of load cycles experienced by the pipeline, and thus it is important to consider all the dominant frequencies of vibration that can occur along the span.

The current profiles were modelled based on the DNV-RP-F105 standard, which distinguishes between two zones of flow: an outer zone and an inner zone. The outer zone is located approximately one local seabed form height above the seabed crest, and it is characterized by mean current velocity and turbulence that vary only slightly in the horizontal direction. In the inner zone, which is closer to the seabed, the mean current velocity and turbulence exhibit significant variations in the horizontal direction. The current velocity profile in this zone is approximately logarithmic, assuming that flow separation does not occur. The logarithmic profile can be described by the following equation:

$$U(z) = U(z_r) \frac{\ln z - \ln z_0}{\ln z_r - \ln z_0}, \tag{8.4}$$

where $U(z)$ is the current velocity at elevation z above the seabed, $U(z_r)$ is the reference current velocity at a height z_r in the outer zone, and z_0 is the bottom roughness parameter which typically is between 0.001 and 0.005 for soft clay. In this case, 0.001 was chosen as roughness, and the reference height was calculated to be approximately 4m. Figure 8.2 displays 10 current profiles (representing each current velocity from the current histogram) used to model the varying current along the seabed profile. Three profiles were used for the span of interest, while one profile was used for each of the two side spans.
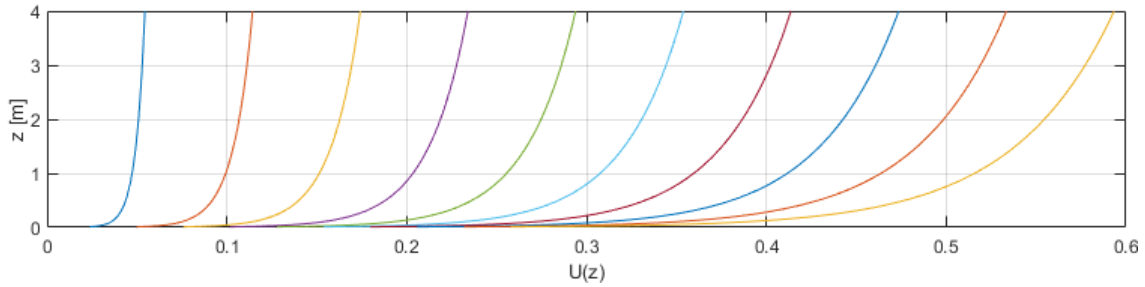
Figure 8.2: Current velocity profiles used in SIMLA.

8.4 Modelling of pipe-soil interaction

In order to model the interaction between the pipeline and the seabed, the SIMLA model employs 3D seabed contact elements (CONT126). The contact element types are defined by a user-defined material surface property that describes the material curve in the x-, y-, and z-directions. By default, a Coulomb model is utilized which multiplies the force x and y components with the z-force reaction and a friction coefficient. As a result, the material curves for the x- and y-directions must be specified as displacement versus unit force curves, as was the case for this model.

The material properties for the x- and y-directions in this model are defined by elastoplastic material behaviour (ep-curves) that includes kinematic hardening. For the z-direction, hyperelastic (non-linear elastic) material behaviour was employed. The soil friction coefficients were set to 0.32 and 0.8 in the global x- and y-directions, respectively. The material curve for the z-direction was generated by identifying the soil penetration in the static analysis where simplified static soil stiffness was used. In the dynamic analysis, further penetration than static penetration was defined by the simplified dynamic vertical stiffness. It is important to note that soil modelling can involve significant uncertainties and, as a result, further investigation may be required in future models.

9 Analysis methodology

The following chapter elaborates on the two procedures used to calculate fatigue damage of the subsea pipeline, with a focus on the TD-VIV approach. In addition, a limited amount of theory is given about the analysis methods used. The goal is to investigate the damage per year at the free span shoulder where fatigue is likely to occur and to compare the results from the two procedures/models. The specific location for fatigue damage calculation is specified later. Figure 9.1 summarizes the procedures for the two models.
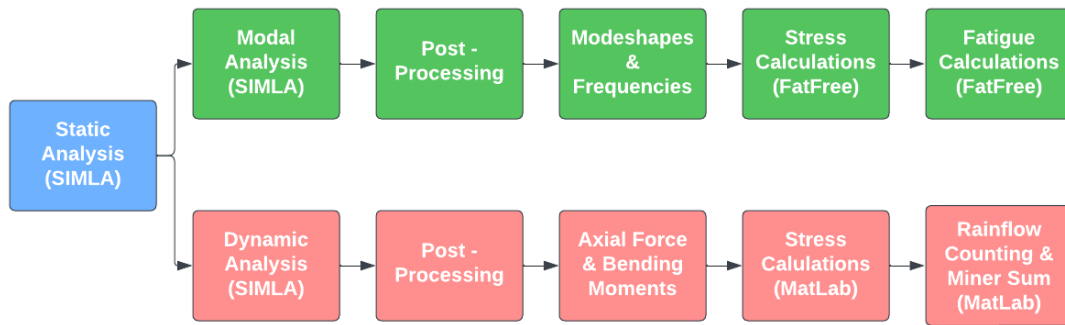
Figure 9.1: Flowchart of analysis methodology.

9.1 Static analysis

By performing a static analysis prior to the modal and dynamic analysis, the effects of static deflection on the pipeline's dynamic response can be accurately captured as mentioned in Section 3, leading to more accurate predictions of the pipeline's behaviour under different loading conditions. The load history used for the static analysis of the shutdown condition is the buoyancy and external pressure, dry mass factored by 1.0203 and the effective axial force of 1150kN in order to replicate the shutdown condition given in the case description. In-line deflection due to steady current is neglected in the analysis since the most probable current velocities are small. The stiffness relation of a static system is given by:

$$\mathbf{Kr} = \mathbf{R}, \tag{9.1}$$

A Newton-Rhapson equilibrium iteration procedure is used to find the static solution at each load step. At iteration zero, the load increment $\Delta\mathbf{R} = \mathbf{R^{II}} - \mathbf{R^{I}}$ results in a displacement increment $\Delta\mathbf{r}$, where $\mathbf{R^{I}}$ is the load at equilibrium state I and $\mathbf{R^{II}}$ is the load at equilibrium state II. The internal load vector and stiffness matrix are updated and iterations are repeated until convergence is achieved. The procedure can be written as given in the SIMLA theory manual by Sævik [26]:

$$\Delta\mathbf{r}_{k+1}^{i} = \mathbf{K}_{T,k+1}^{-1i} \, \Delta\mathbf{R}_{k+1}^{i}. \tag{9.2}$$

9.2 Modal analysis

After the static analysis when the free spanning pipeline is in equilibrium, a modal analysis is performed in order to find the mode shapes and natural frequencies of the system. The modal coordinates and frequencies are extracted using SIMPOST and further processed in FatFree in order to calculate stress ranges by the VIV response model and fatigue damage using the SN-curve approach. The solution to the eigenvalue problem is found by solving:

$$(\mathbf{K} - \omega^2 \mathbf{M})\Phi = 0, \tag{9.3}$$

where $\mathbf{M}$ is the mass matrix, ω is the eigenfrequency and Φ is the mode shape. SIMLA utilizes the well-known Lanczos algorithm to find the eigenvalues and eigenvectors of large Hamiltonian matrices by iteration. The algorithm works by constructing a sequence of approximations to the matrix's eigenvectors and using these approximations to calculate the eigenvalues. The quality of the approximations improves with each iteration, allowing the algorithm to converge to the true eigenvalues and eigenvectors of the matrix. Section 3.2 in Bell [27] describes the computational procedure in detail.

9.3 Dynamic analysis

The dynamic analysis in SIMLA using the TD-VIV force model is aimed to obtain time histories of axial force and bending moments at the pipeline shoulder, as this location is critical for fatigue damage due to the significant stresses and bending moments it experiences from dynamic loads. The pipeline shoulder is particularly susceptible to damage from cross-flow vibrations due to the large span length, which can cause large-amplitude oscillations of the pipeline in the transverse direction. As a result, it is crucial to study the behaviour of the pipeline at this location to accurately assess the potential for fatigue damage and ensure the safety and reliability of the structure.

Special care must be given to the selection of the simulation duration. The simulation should be reaching to a steady state within the given time to obtain reliable results. Several simulations were run, and after observing the signal pattern, it was concluded that the steady-state condition was usually reached well before 100 seconds for all cases, and the system's behaviour remained consistent throughout the simulation period after. Therefore, in order to be sure that the transient phase is not included in the stress and fatigue calculations, the first 100s of the signal were removed. As for the simulation duration, 1000s was used which corresponds to at least 100 periods of the lowest natural period (9.8s) from the modal analysis. The time-step chosen was 0.1s and is based on the lowest observed period of the simulations, which is approximately 1.6s (0.6Hz). That gives 16 steps for the lowest natural period. To more accurately capture the peaks, more than 16 steps could be used for the lowest periods (simulations with larger current velocities), but a sensitivity study performed gave insignificant differences in the mean stress ranges and fatigue damage calculations. To summarize, a simulation length of 1000s and time-step of 0.1 was used for all the simulations in the case scenario.

In solving nonlinear dynamic problems, modal superposition is not applicable and direct time integration of the equation of motion is required. Two methods can be used for this purpose, namely, explicit and implicit methods [26] [24]. Explicit methods are commonly expressed in the form of Equation 9.4, where the displacement at the next timestep is determined based on information from the current and previous timesteps. These methods are conditionally stable, requiring the use of very small time steps to ensure accuracy. If explicit methods are formulated in terms of lumped mass and damping matrices,

there is no need to solve a coupled equation system, resulting in minimal computational efforts per time step. Explicit methods are particularly useful in the analysis of impulse-type responses, such as explosion and impact analysis, where small time steps are necessary to achieve adequate precision. On the other hand, implicit methods are unconditionally stable, allowing for the use of larger time steps, but require the solution of a coupled equation system at each time step.

$$\mathbf{r_{k+1}} = \mathbf{f}(\ddot{\mathbf{r}}_\mathbf{k}, \dot{\mathbf{r}}_\mathbf{k}, \mathbf{r_k}, \mathbf{r_{k-1}}, ...)$$ (9.4)

Implicit methods, such as those expressed in Equation 9.5, have better numerical stability than explicit methods because they use information from the next time step. The stability of implicit methods varies based on assumptions about how acceleration changes between time steps and when the equilibrium equation is fulfilled. By assuming constant average acceleration, an unconditionally stable method can be achieved, which provides numerical stability regardless of the time step size. This makes it beneficial to use implicit methods for long analysis durations. However, if short time steps are necessary for accuracy, solving a coupled equation system at every time step can become uneconomical.

$$\mathbf{r_{k+1}} = \mathbf{f}(\ddot{\mathbf{r}}_\mathbf{k+1}, \ddot{\mathbf{r}}_\mathbf{k}, \dot{\mathbf{r}}_\mathbf{k+1}, \dot{\mathbf{r}}_\mathbf{k}.\mathbf{r_k}, ...)$$ (9.5)

In practical cases, the guarantee of unconditional stability for implicit methods does not hold for nonlinear systems, but this is generally not a significant issue. In dynamic analysis, high-frequency modes are of little interest and can be described with less accuracy than lower modes. To achieve this, it is desirable to remove high-frequency modes while accurately describing lower modes. Increasing the damping ratio or introducing Rayleigh-damping in the Newmark-β method can dampen out medium modes while leaving lower and higher modes almost unaffected. Numerical damping can also be used to damp out higher modes, at the cost of reducing accuracy from 2nd order to 1st order. However, this drawback can be eliminated by applying the implicit HHT-α method, which retains 2nd order accuracy while damping out high-frequency modes. In this model, a HHT-α factor of -0.05 was used. For references see the SIMLA theory manual [26].

9.4 Stress calculations

In order to assess the fatigue damage on the free-spanning pipeline shoulder element, time histories of axial force and bending moments at the shoulder obtained in the dynamic analysis were processed in the post-processing program DYNPOST, which is a part of the SIMLA software package. The purpose of this post-processing step was to compute time histories of stresses and to calculate fatigue damage, which could then be used to evaluate the structural integrity of the pipeline. In addition to the axial force and bending moment data, the displacement in both in-line and cross-flow directions at the mid-span was also processed. The resulting data was then analyzed using MatLab. To investigate the frequencies at which vortex-induced vibrations and lock-in were occurring, a fast Fourier transform (FFT) was performed on the time-domain signals. FFT is a mathematical technique that allows signals to be transformed from the time domain into the frequency domain. By performing FFT on the time-domain signals, it was possible to identify the frequencies at which the pipeline was experiencing vortex-induced vibrations and possibly lock-in. In order to convert the combined effect of the axial force (Fx) and bending moments (My, Mz) into a stress signal, an analytical procedure was performed. This was necessary because the axial force and bending moments alone do not provide an accurate representation of the stresses experienced by the pipeline. The following equation was used to perform the stress conversion:

$$\sigma_x = \frac{F_x}{A} + \frac{M_y}{I} R \sin\theta + \frac{M_z}{I} R \cos\theta, \tag{9.6}$$

where F_x is the axial force, A is the cross-section area, I is the area moment of inertia, and R takes the value of either the outer radius (cap) or inner radius (root) of the pipeline's cross-section. M_y is the bending about y-axis (bending in cross-flow direction), and M_z is the bending about z-axis (in-line direction). The angle θ takes values of 0-315 degrees with a 45-degree step interval, allowing for the computation of stresses and fatigue damage around the cross-section as shown in Figure 9.2.
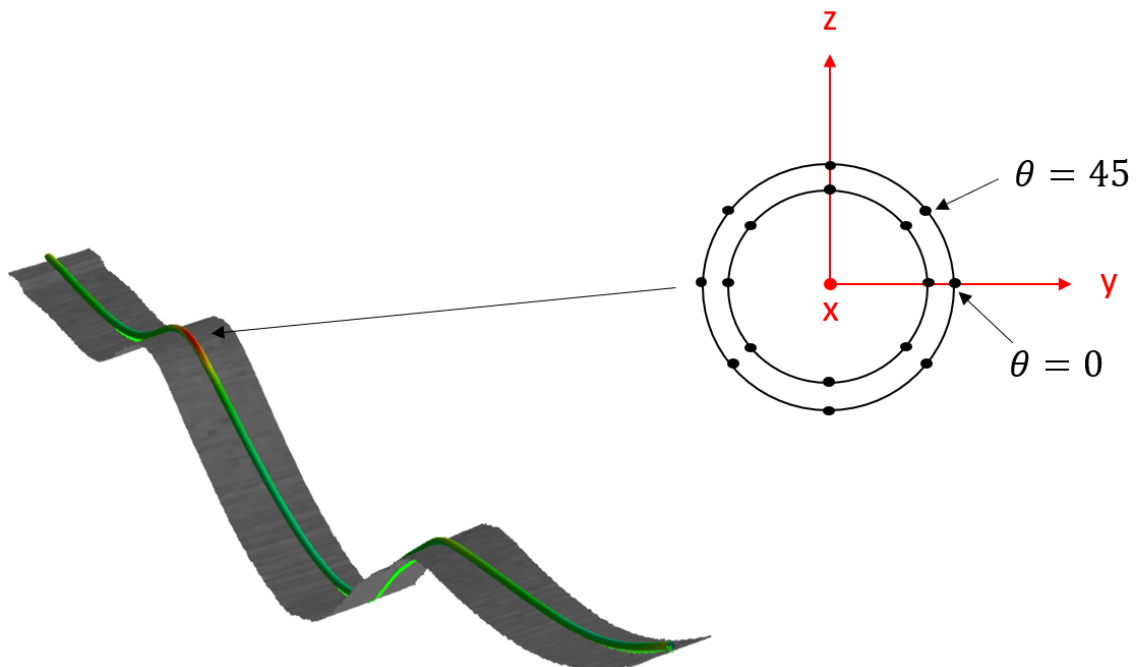
Figure 9.2: Overview of stress calculations. Longitudinal stress and fatigue damage have been calculated at each black dot.

9.5 Fatigue damage per year calculations

To calculate the fatigue damage/y at the shoulder element, individual current simulations were run for the case scenario. For each simulation, stresses around the mentioned points of the pipe's cross-section were calculated, and the resulting stress histories were evaluated for stress range ($\Delta\sigma$) and corresponding cycles (n_i) using the Rainflow algorithm in MATLAB.

Fatigue damage was calculated for each current velocity and direction based on the Haibach SN curves and the Palmgren-Miner linear damage accumulation rule. The SN data given for both cap and root in Section 7.2.3 was used to find the maximum cycles (N_i) in a specific stress range. Miner sum was then calculated for each of the individual simulations, and the results were used to find the total fatigue damage.

The fatigue damage for each current was multiplied by the corresponding probability of occurrence obtained from the current histogram. This weighs the contribution of each current to the total fatigue damage and gives fatigue damage representing the real loading condition. The individual damage for each simulation was scaled to damage per year, and the total damage for all simulations was summed up to obtain the total fatigue damage per year for the free span shoulder element. The procedure for calculating the fatigue damage per year was as follows:

1. For each simulation, direction, and point in cross-section, evaluate the stress range ($\Delta\sigma$) and corresponding cycles (n_i) using the Rainflow algorithm in MATLAB.

2. Use the SN data given in Section 7.2.3 to find the maximum cycles (N_i) in a specific stress range:

$$N_i = \frac{C}{\Delta\sigma^m}. \tag{9.7}$$

3. Calculate the Miner sum for each of the individual simulations:

$$d_i = \frac{\Delta n_i}{N_i}. \tag{9.8}$$

4. Multiply the Miner sum for each simulation by its corresponding probability of occurrence (PO) prior to the summation to obtain the damage for each individual simulation:

$$D_i = d_i \times PO_i. \tag{9.9}$$

5. Scale the calculated Miner sum for each individual simulation to one damage per year:

$$D_{year,i} = D_i \times \frac{365 \times 24 \times 60 \times 60}{t_s}. \tag{9.10}$$

6. Sum the damage per year in each point in the cross-section for all simulations to obtain the total fatigue damage:

$$D_{year} = \sum_{i=1}^{n} D_{year,i}. \tag{9.11}$$

where n is the number of simulations and t_s is the simulation duration after steady state.

10 Case results and discussion

10.1 Static analysis

Figure 10.1 illustrates the seabed profile and the static configuration for the selected shutdown condition at KP value 600m from Table 7.1. The previous assessment was done by actual simulation of the shutdown condition in SIMLA, while these results are based on applying the corresponding effective axial load of 1150kN from the simulation to the new model, in order to replicate the condition. Some deviation can be expected as the applied axial load is limited to one translation direction and might not accurately represent the displacement or static configuration from the original analysis by Reinertsen New Energy. Figure 10.2 displays gaps (free spans) and penetration of the seabed in meters, where positive values indicate a gap and negative values indicate penetration. It is seen that there exist two or three significant spans, where the largest one is of interest in this case. The free span starts at KP value 519m and ends at 705m, giving it a span length of 186m compared to the 189m in the previous analysis. The maximum gap between the span and seafloor is 1.32m located at KP value of 620m.
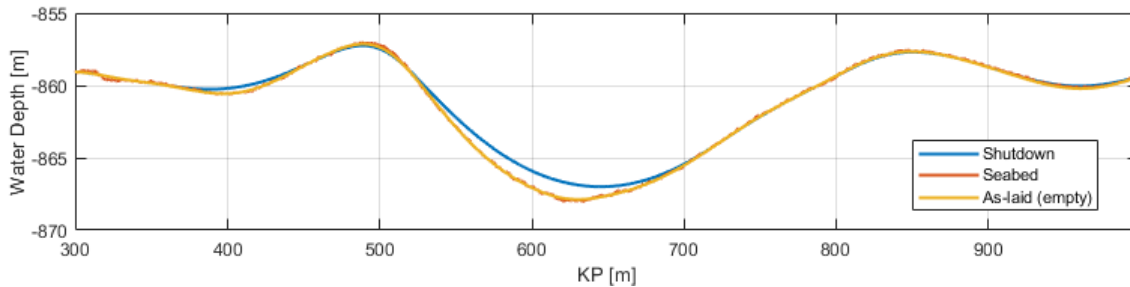
Figure 10.1: Seabed profile and static configuration for shutdown condition for case scenario.
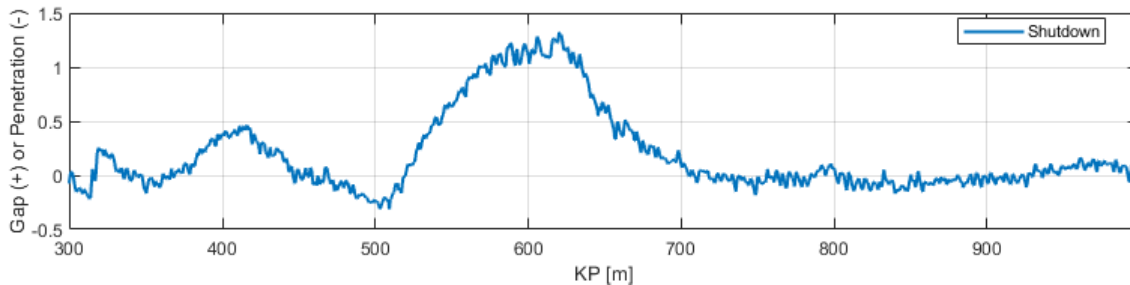
Figure 10.2: Gap/Penetration (in meters) in the static shutdown condition for case scenario. Positive values indicate a gap (free span) while negative values represent seabed penetration

10.2 Modal analysis

A modal analysis has been performed in SIMLA according to Section 9.2. Figure 10.3 and 10.4 display some selected in-line and cross-flow modes respectively, where the span of particular interest has been excited. Table 10.1 and 10.2 give all the possible excited in-line and cross-flow modes to be included in the VIV assessment based on the response model in FatFree. To find which modes from the analysis to include in the VIV assessment, a screening analysis was performed according to DNV-RP-C205 [10] in order to investigate possible excited modes. In-line modes with $1.0 \leq V_R \leq 4.5$ and cross-flow modes with $3 \leq V_R \leq 16$ were used as criteria. There were found 20 possible excited in-line modes ranging

between 0.102-1.24Hz and 6 possible excited cross-flow modes ranging between 0.234-0.398Hz. The purple cells in the tables indicate the modes where the span of particular interest has been excited.
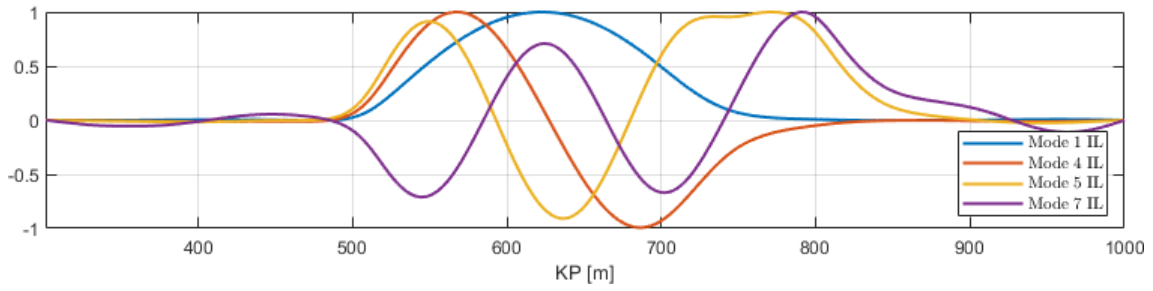
Figure 10.3: Some selected possible excited in-line mode shapes for the response model in FatFree.
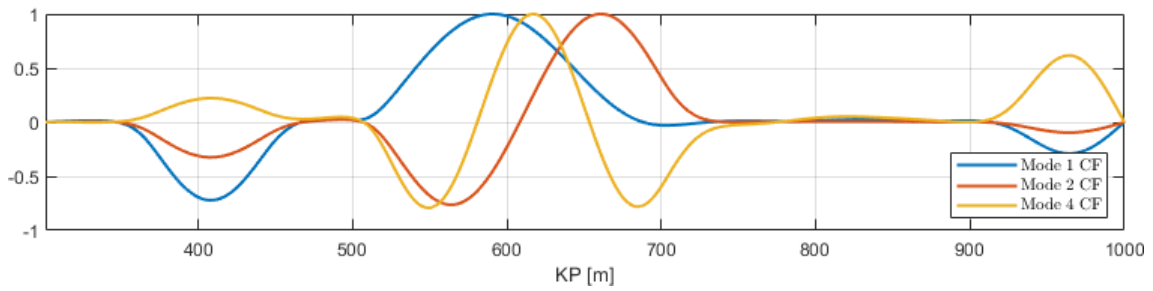
Figure 10.4: Some selected possible excited cross-flow mode shapes for the response model in FatFree.

Mode IL	1	2	3	4	5	6	7	8	9	10
f_n [Hz]	0.102	0.164	0.185	0.202	0.291	0.321	0.325	0.349	0.407	0.439
Mode IL	11	12	13	14	15	16	17	18	19	20
f_n [Hz]	0.453	0.503	0.589	0.809	0.875	0.944	1.01	1.08	1.16	1.24

Table 10.1: All possible excited in-line modal frequencies for the response model in FatFree.

Mode CF	1	2	3	4
f_n [Hz]	0.234	0.258	0.328	0.398

Table 10.2: All possible excited cross-flow modal frequencies for the response model in FatFree.

10.3 FatFree response model

Multiple location analysis has been performed according to DNV-RP-F105 using FatFree software to evaluate the stress amplitudes at various locations along the pipeline free span. The analysis involved the use of the previously obtained mode shapes and eigenfrequencies for in-line and cross-flow direction as inputs to determine the unit stress amplitude per location. The analysis shows that the stress ranges vary significantly at different locations and modes, indicating the importance of considering the multiple modes' effects in the design and analysis of the pipeline. The results obtained from the analysis were used to identify the critical locations and choose the critical element for further investigation.

The in-line stress ranges are shown in Figure 10.5. The highest stress ranges are observed in the modes with higher frequencies, indicating that the structure's response is more sensitive to high-frequency vibrations. The cross-flow stress ranges, shown in Figure 10.6, exhibit similar trends to the in-line stress ranges, with the largest ranges observed in the higher-frequency modes. Equation 5.1 and 5.7 were used in the calculation, and a stress range safety factor of $\gamma_s = 1.3$ was used in FatFree. Additionally, on-set safety factors for both in-line and cross-flow response amplitude were 1.1 and 1.2 respectively for use in the calculation of the unit stress amplitude. Optimally, these safety factors would be disabled or set to unity, to get a more comparative result to the SIMLA force model. Unfortunately, this was not an option in FatFree. However, the remaining safety factors which are not mentioned here were set to unity. Figure 10.7 and 10.8 gives the location-wise annual fatigue damage for in-line and cross-flow direction respectively, and the result shown is the worst between the two SN curves used. The maximum cross-flow fatigue damage/y was 4.72×10^{-5} at KP-value 510m, and the corresponding in-line damage/y was 3.6×10^{-6}. Based on this, element number 342 is used further for the TD-VIV analysis which is at KP-value 510m.
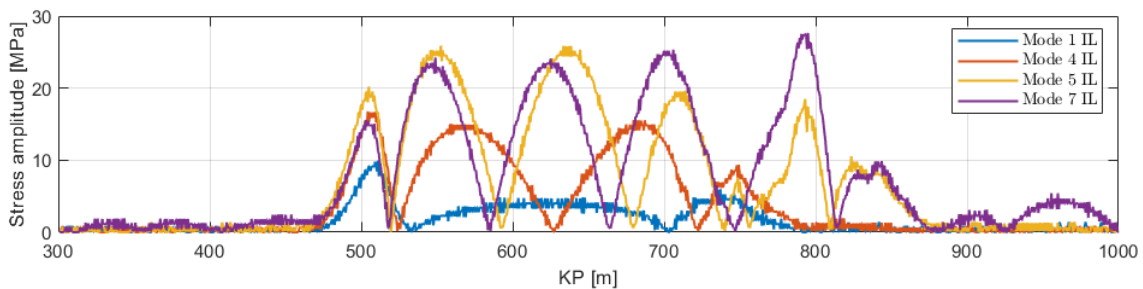
Figure 10.5: Some selected modal in-line stress amplitudes for the response model in FatFree.
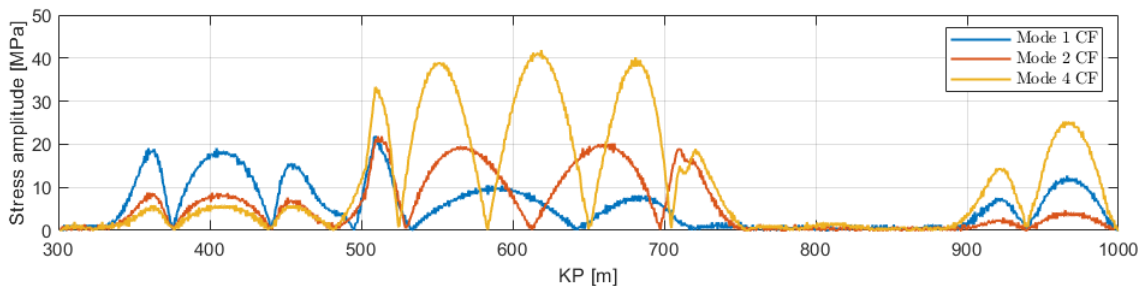
Figure 10.6: Some selected modal cross-flow stress amplitudes for the response model in FatFree.
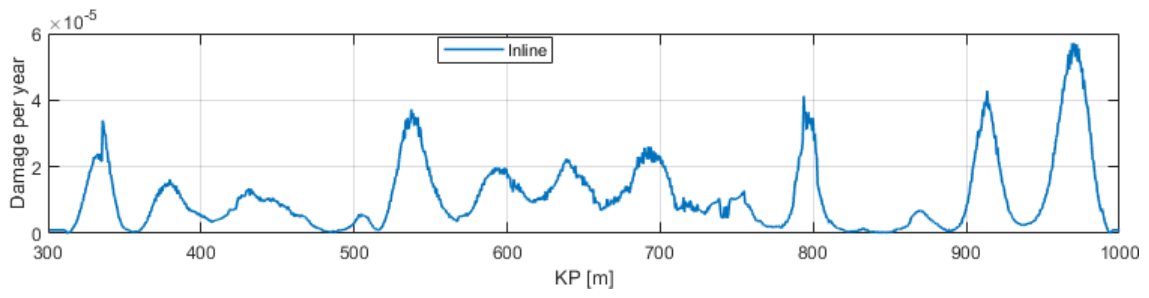
Figure 10.7: FatFree response model damage/y at various locations along the pipeline in the in-line direction.
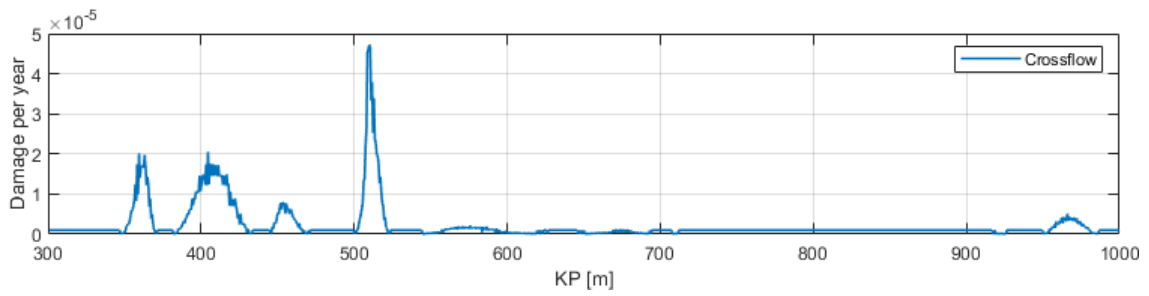
Figure 10.8: FatFree response model damage/y at various locations along the pipeline in the cross-flow direction.
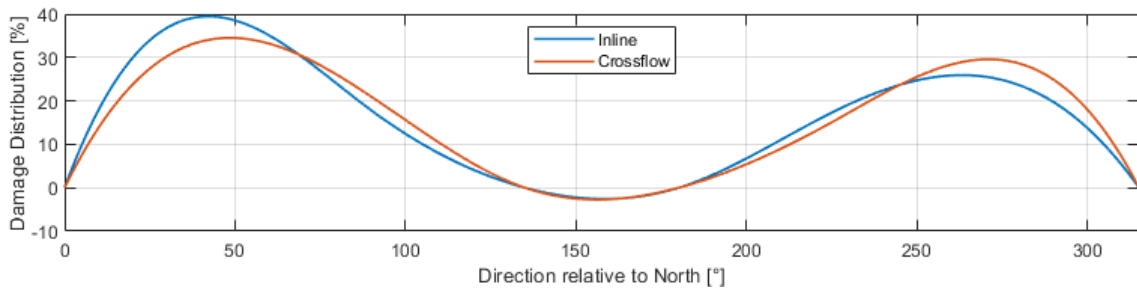
Figure 10.9: Damage distribution vs. direction relative to North for FatFree response model.

10.4 SIMLA TD-VIV force model

In this section, results from the dynamic analysis in SIMLA are presented according to the methodology in Chapter 9. To strike a balance between providing enough information to support arguments without overwhelming excessive data, the most significant and informative results are included. That is the cumulative damage at shoulder element 342, as well as a representative simulation response summary and results. The representative simulation response summary and results will be for currents 90 degrees relative to North, as this is closest to normal on the pipeline free span, and thus the most response is expected (but not necessarily damage due to probability of occurrence). The simulation results for each current in this direction consist of the output data, i.e. the axial forces and bending moments at shoulder element 342, and the in-line and cross-flow response amplitudes at node 512 (at the midspan). Additionally, calculated longitudinal stresses, rainflow counting data, and damage/y results across the cross-section are presented. The results will be for the root position, as the damage was most significant there compared to the cap position. Results for damage/y from other current directions can be found in Appendix B for cap position and Appendix C for root position.

10.4.1 Cumulative damage/y at shoulder

Figure 10.10 and Table 10.3 gives the cumulative damage/y result for the case scenario for element 342 at the shoulder, root position. That is, the cumulative damage/y for each current direction and velocity, for different θ-angles across the cross-section. As expected and similar to the result from FatFree in Figure 10.9, currents from 45, 90, 225 and 270° relative to the geographic North contributes most significantly to the damage/y. The area in the cross-section with the largest sum of cumulative damage/y is located at $\theta = 180°$, with a damage/y of 4.16×10^{-6}. This represents the in-line direction and is in the same order of magnitude as the in-line damage/y from the FatFree result, which was 3.6×10^{-6}. The largest damage/y in the cross-section that can be related to the cross-flow response, is located at $\theta = 270°$ and has a value of 3.14×10^{-6}. This is one order of magnitude less than the predicted damage/y in FatFree, which was 4.72×10^{-5}. These results are summarized in Table 10.4 and are the final result for the cumulative damage/y at shoulder element 342. Later, a sensitivity study performed will show that SIMLA and FatFree damage/y results correlate well for lower current velocities, as is the case for this case scenario. Additionally, we will see that FatFree is more conservative regarding the cross-flow damage/y compared to SIMLA, as in the case scenario.
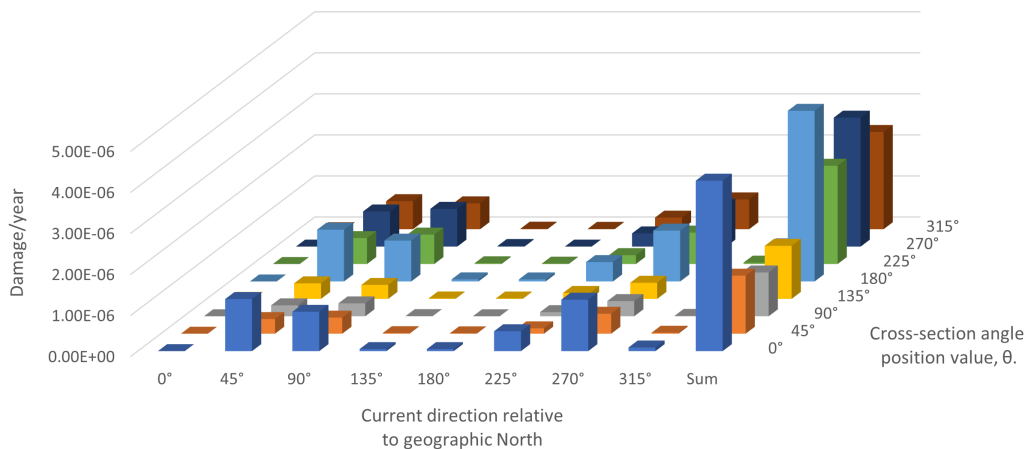
Figure 10.10: Root cumulative damage/y at shoulder element 342 for all current directions and θ-angles.

		Cross-section angular position, θ.							
		0°	45°	90°	135°	180°	225°	270°	315°
Current direction	0°	3.11E-18	8.64E-19	2.76E-19	3.84E-19	3.28E-18	9.84E-19	4.95E-19	3.64E-19
	45°	1.27E-06	3.57E-07	2.68E-07	3.79E-07	1.26E-06	6.31E-07	8.57E-07	6.83E-07
	90°	9.59E-07	3.93E-07	3.15E-07	3.40E-07	9.95E-07	7.18E-07	9.21E-07	6.30E-07
	135°	5.01E-08	1.27E-08	5.12E-09	9.80E-09	5.07E-08	1.83E-08	1.52E-08	1.34E-08
	180°	4.94E-08	9.45E-09	3.12E-13	8.41E-09	4.95E-08	9.66E-09	9.04E-13	8.52E-09
	225°	4.85E-07	1.31E-07	1.01E-07	1.45E-07	4.72E-07	2.17E-07	3.22E-07	2.83E-07
	270°	1.25E-06	4.87E-07	3.70E-07	3.93E-07	1.24E-06	7.67E-07	1.00E-06	7.27E-07
	315°	8.91E-08	2.38E-08	9.99E-09	1.76E-08	8.96E-08	3.37E-08	2.82E-08	2.58E-08
	Sum	4.15E-06	1.41E-06	1.07E-06	1.29E-06	4.16E-06	2.39E-06	3.14E-06	2.37E-06

Table 10.3: TD-VIV model root cumulative damage/y at shoulder element 342 for case scenario. Each column represents an angular position in the cross-section, and each row represents a current direction.

	FatFree	SIMLA
In-line damage/y	3.6×10^{-6}	4.16×10^{-6}
Cross-flow damage/y	4.72×10^{-5}	3.14×10^{-6}

Table 10.4: Cumulative damage/y final result at shoulder element 342. FatFree vs. SIMLA.

10.4.2 Response & damage/y summary for currents 90° relative to geographic North

The normalized with respect to diameter response amplitude in SIMLA compared to the response model in FatFree is shown in Figure 10.11 for the in-line direction, while Figure 10.12 displays the corresponding frequency content. Further, Figure 10.13 and 10.14 do the same for the cross-flow direction. Figure 10.15 illustrates the damage/y across the cross-section for each current velocity from the simulations, accounting for the current probability of occurrence. For other current directions. Response amplitudes (nodal displacements) were extracted from node 512 which is located approximately at the 1/2 of the span length, i.e. at the midspan. This implies that it is more prone to accurately capture the maximum response amplitudes of symmetric vibrations rather than antisymmetric, where the maximum response amplitudes usually are located at 1/3 and 2/3 of the span length. FatFree response models are empirical models providing the maximum steady state VIV amplitude for each mode, hence only the symmetric modes of the span of interest are included in order to compare the responses with SIMLA. The mode shapes were presented in Section 10.2. For the in-line response amplitude, there seems to be a good correlation between SIMLA and FatFree RM, while cross-flow synchronization happens at lower velocities and has a narrower bandwidth in the TD-VIV model compared to FatFree RM.
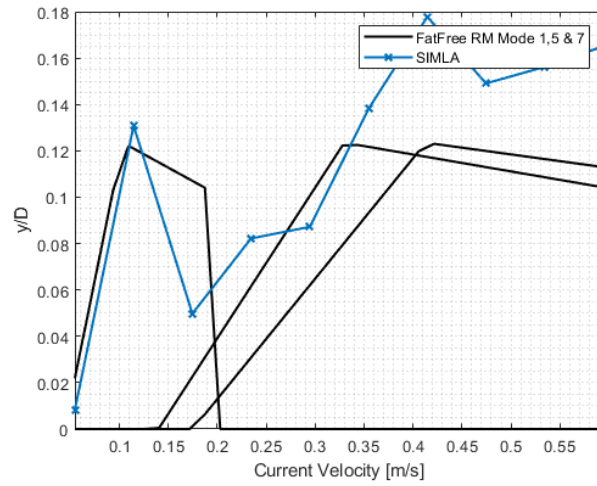
Figure 10.11: IL response amplitude vs. current velocity. RM vs. TD-VIV model.
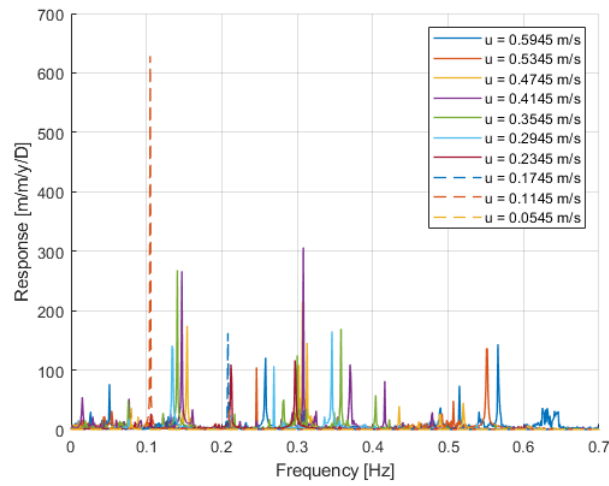
Figure 10.12: IL response frequency content for TD-VIV model.
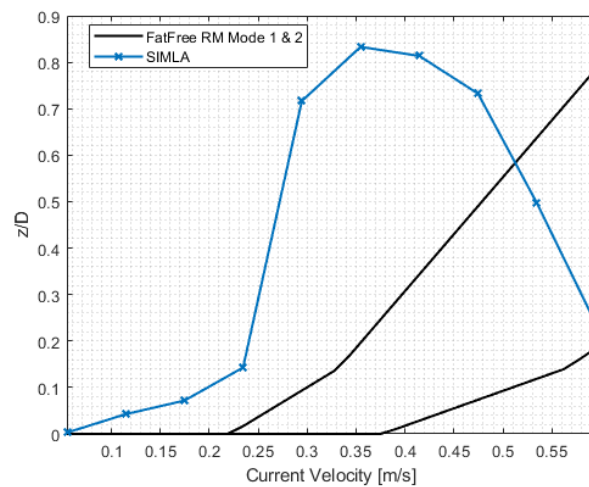
Figure 10.13: CF response amplitude vs. current velocity. RM vs. TD-VIV model.
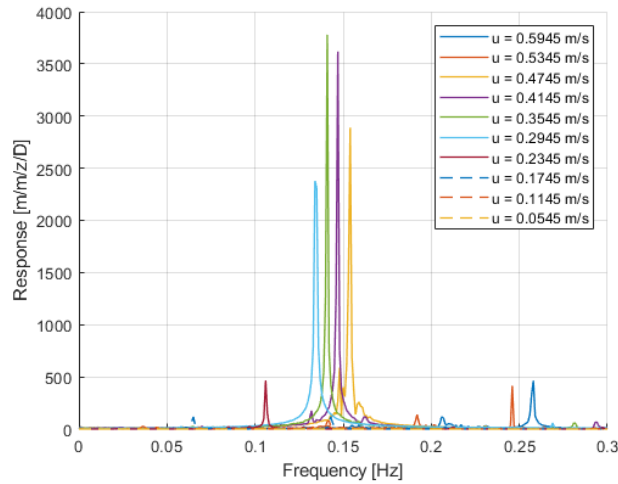
Figure 10.14: CF response frequency content for TD-VIV model.
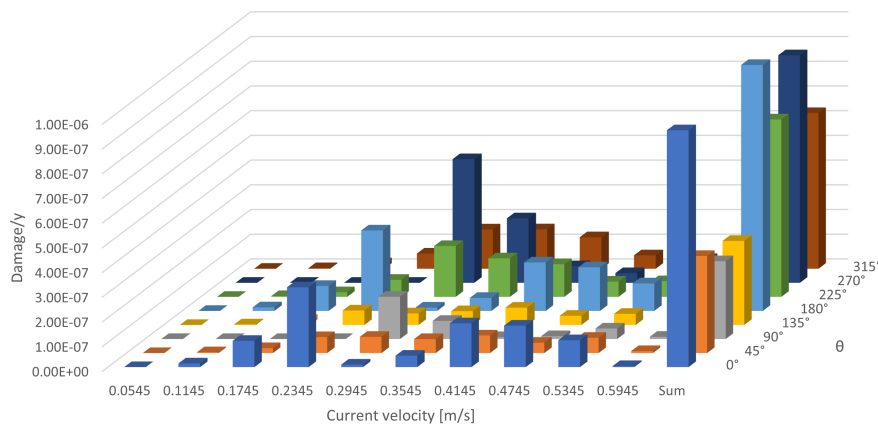
Figure 10.15: Root damage/y from currents 90° relative to geographic North. TD-VIV model.

The response in the figures above can be summarized as follows:

- At 0.0545 m/s current velocity there is a negligible response in both in-line and cross-flow directions, indicating that the VIV frequency is not close to one of the natural frequencies of the system. If the frequency of the applied load is not close to one of the natural frequencies of the system, the response will be less pronounced. This is because the system is less sensitive to the applied load and its ability to absorb or dissipate the energy from the load is greater. The damage/y is 0 at this velocity for all θ-angles across the cross-section.

- At 0.1145 m/s a significant in-line response can be seen, with a maximum response amplitude of 0.13D. The VIV frequency is 0.105Hz, which is close to the first natural frequency of the system from the modal analysis, which was 0.102Hz, implying that lock-in has occurred causing large amplitude vibrations. The cross-flow response is still negligible. The damage/y slightly increases as a result and is the largest at θ-angles 0, and 180°.

- At 0.1745 m/s the maximum in-line response amplitude has decreased to 0.05D, with a VIV frequency of 0.208Hz. This is close to the 2nd harmonic in-line vibration from the modal analysis,

which was 0.202Hz. Again, lock-in has occurred causing large amplitude vibrations. Keep in mind that the response amplitude was measured at the midspan, which is not necessarily giving the maximum response amplitude across the span. Cross-flow vibrations are still negligible. The damage/y slightly increases again and is the largest at θ-angles 0, and 180°.

- At 0.2345 m/s the maximum in-line response amplitude increases to 0.08D, and with two significant pure in-line VIV frequencies of 0.212Hz and 0.297Hz, indicating a multimodal IL response, where both the 2nd harmonic component from the previous current condition and a new component has been excited. From the modal analysis, the 3rd harmonic was found to be 0.291Hz, which is close to the new VIV frequency component. Thus, it can be concluded that there exists a multimodal response where lock-in has occurred for 2nd and 3rd harmonic. Additionally, a smaller response starts to develop for the cross-flow direction. The damage/y reaches its maximum for the IL direction at this current velocity and is the largest at θ-angles 0, and 180°. Both sides experiences approximately the same damage/y 3.23×10^{-7} and 3.25×10^{-7} respectively.

- At 0.2945 m/s the response increases in complexity. First off, the maximum in-line response amplitude has increased to 0.09D, with two dominant pure IL VIV frequencies of 0.269Hz and 0.346Hz, again indicating a multimodal IL response. The closest harmonics from the modal analysis are the 3rd harmonic as in the previous current condition, and the 4th harmonic from the modal analysis which were found to be 0.325Hz. What is more, a larger cross-flow response amplitude of 0.72D is evident now. The CF VIV frequency is 0.134Hz, which is below the first CF natural frequency of 0.234Hz from the modal analysis. Still, due to large amplitude vibrations and the vibration pattern, lock-in seems to have occurred in this direction. The vibration additionally causes CF-induced IL vibrations at the same frequency, adding a third IL component to the IL response. A larger deviation is seen between the natural frequencies from the modal analysis and the responses from the dynamic analysis. There can be several reasons for this, i.g., shifts in natural frequencies due to added mass effects, non-linear soil properties; the stiffness and damping of the soil can vary significantly with the amplitude of vibration, the influence by several non-uniform current profiles and other non-linear effects on the model, or chosen TD-VIV model parameters. Additionally, modal frequencies also tend to become more inaccurate at higher modes. While lock-in/resonance is one possible cause of vibrations in the system, vibrations can also be caused by other sources such as external excitation and damping forces, and lock-in has not necessarily occurred for the IL direction. Only intensive parameter studies and experiments can validate the response. The damage/y decreases significantly at θ-angles 0, and 180° and is close to 0. At θ-angles 45, 90, 135, 225 and 315° the damage/y has increased, especially at 225, 270 and 315°. The maximum damage/y is found at θ-angle 270°, where 270° has the largest cross-flow damage/y for all current conditions (5×10^{-7}). This is on the compression side of the pipeline (negative bending moment), where there is contact between the pipeline and the seafloor.

- At 0.3545 m/s the maximum in-line response amplitude increases significantly to 0.14D. This time, one dominant pure IL frequency of 0.358Hz is present. Additionally, the first mode lock-in for the cross-flow direction continues and the maximum response amplitude has increased to 0.83D, with a vibration frequency of 0.141Hz, again causing CF-induced IL vibrations at the same frequency. As for the previous current condition, deviations between the natural frequencies from the modal analysis and the VIV frequencies exist. The damage/y for θ-angles 0 and 180° slightly increases again, decreases at θ-angles 90, and 270°, but are still largest at 270°.

- 0.4145 m/s the maximum in-line response amplitude increases to 0.18D. There exists one dominating pure in-line frequency of 0.307Hz and one less significant of 0.370Hz. The dominating frequency is close to the 3rd harmonic, indicating that lock-in has occurred, while the less significant is more uncertain as it lies between the 4th and 5th harmonic. The maximum cross-flow

response amplitude has decreased to 0.81D, but still experiences first-mode lock-in with a vibration frequency of 0.147Hz. Again, this response can be seen in the IL response frequency content, implying that it is still causing CF-induced IL vibrations. The damage/y for θ-angles 0 and 180° slightly increases, and decreases significantly to a negligible level at θ-angles 90, and 270°. From here and outward, the damage/y slightly decreases for increasing current velocities due to lower probabilities of occurrence.

- At 0.4745 m/s the maximum in-line response amplitude decreases to 0.15D. The same dominating pure IL frequency (0.307Hz) as for the previous current condition is present, but two additional and not-so-insignificant frequencies lie in the vicinity of it, at 0.302Hz and 0.313Hz. The maximum cross-flow vibration amplitude decreases to 0.73D, with a VIV frequency of 0.154Hz. Thus, it still experiences first-mode lock-in, causing CF-induced IL vibrations.

- At 0.5345 m/s the maximum in-line response amplitude increases to 0.16D, with two dominant pure IL VIV frequencies of 0.246Hz and 0.551Hz present. Both lie between two eigenfrequencies from the modal analysis, thus lock-in has not necessarily occurred and the vibration might be due to other sources. The maximum cross-flow response amplitude decreases significantly to 0.50D, now responding with a VIV frequency of 0.246Hz. This implies that it has left the first mode synchronization range, and has entered for the second. This is clearly visible when visualizing the response in SIMLA, where the span of interest changes vibration pattern from 1st harmonic to 2nd as the velocity is increased. Again, the maximum response amplitude is measured at the midspan, which assumingly does not give the maximum amplitude across the span for the second harmonic. CF-induced IL vibrations at the same frequency are present in the in-line frequency content.

- At 0.5945 m/s the maximum in-line response amplitude increases to 0.17D. The two dominant pure IL VIV frequencies from the previous current condition are still present, but responding at slightly higher frequencies (approximately 0.10Hz higher). The maximum cross-flow response amplitude decreases to 0.24D, and regarding the response, it is also similar to the previous. By summing the damage/y at each θ-angle for all current velocities, it becomes evident that the cumulative damage/y for this current direction is the largest θ-angle 180 and 270°with a value of 9.95×10^{-7} and 9.21×10^{-7}.

10.4.3   Simulation results for currents 90° relative to geographic North

0.0545 m/s
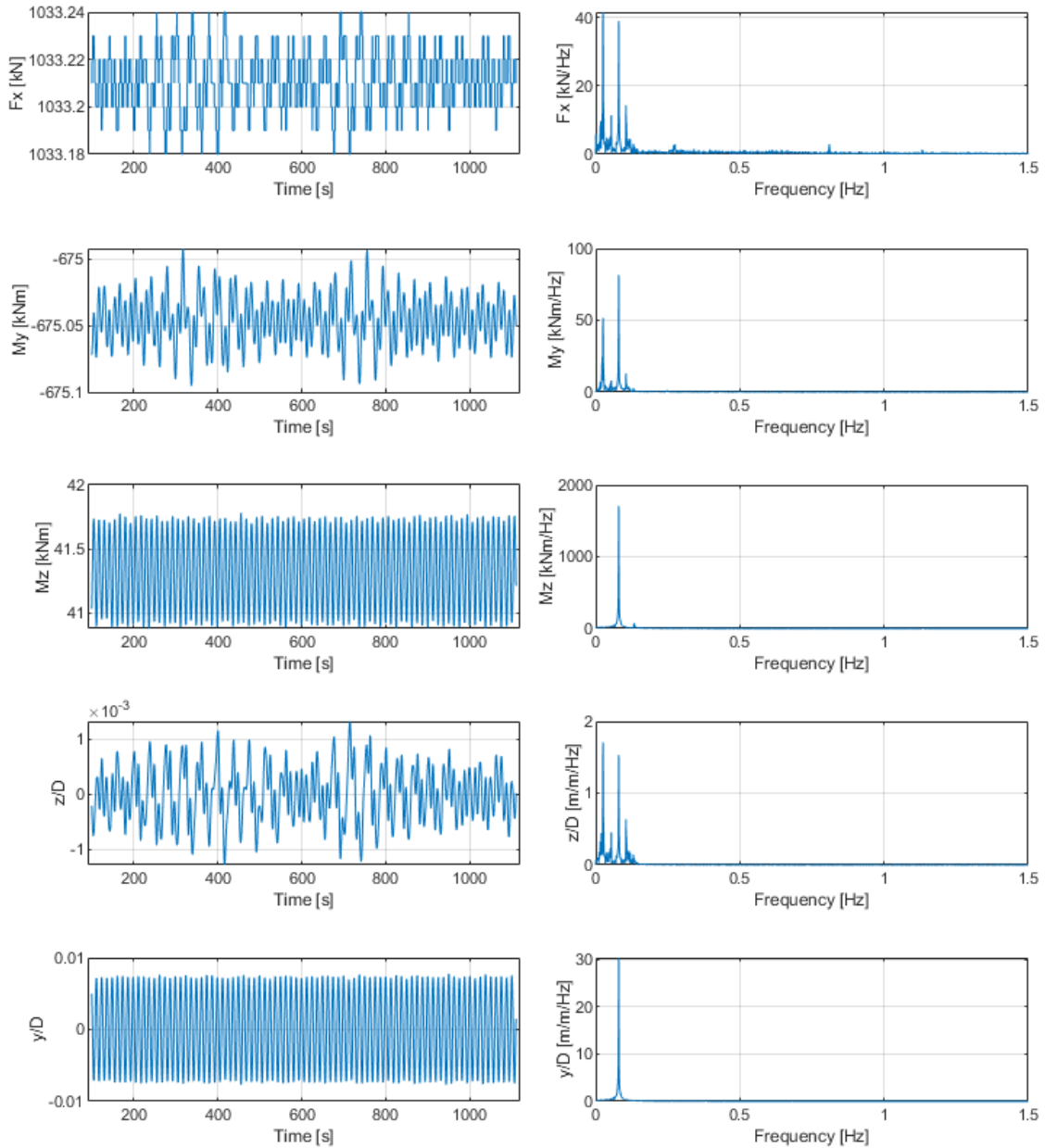
Figure 10.16: Time histories and FFT of axial force, Fx, cross-flow bending moment, My, and in-line bending moment, Mz, at shoulder element 342. z/D and y/D are n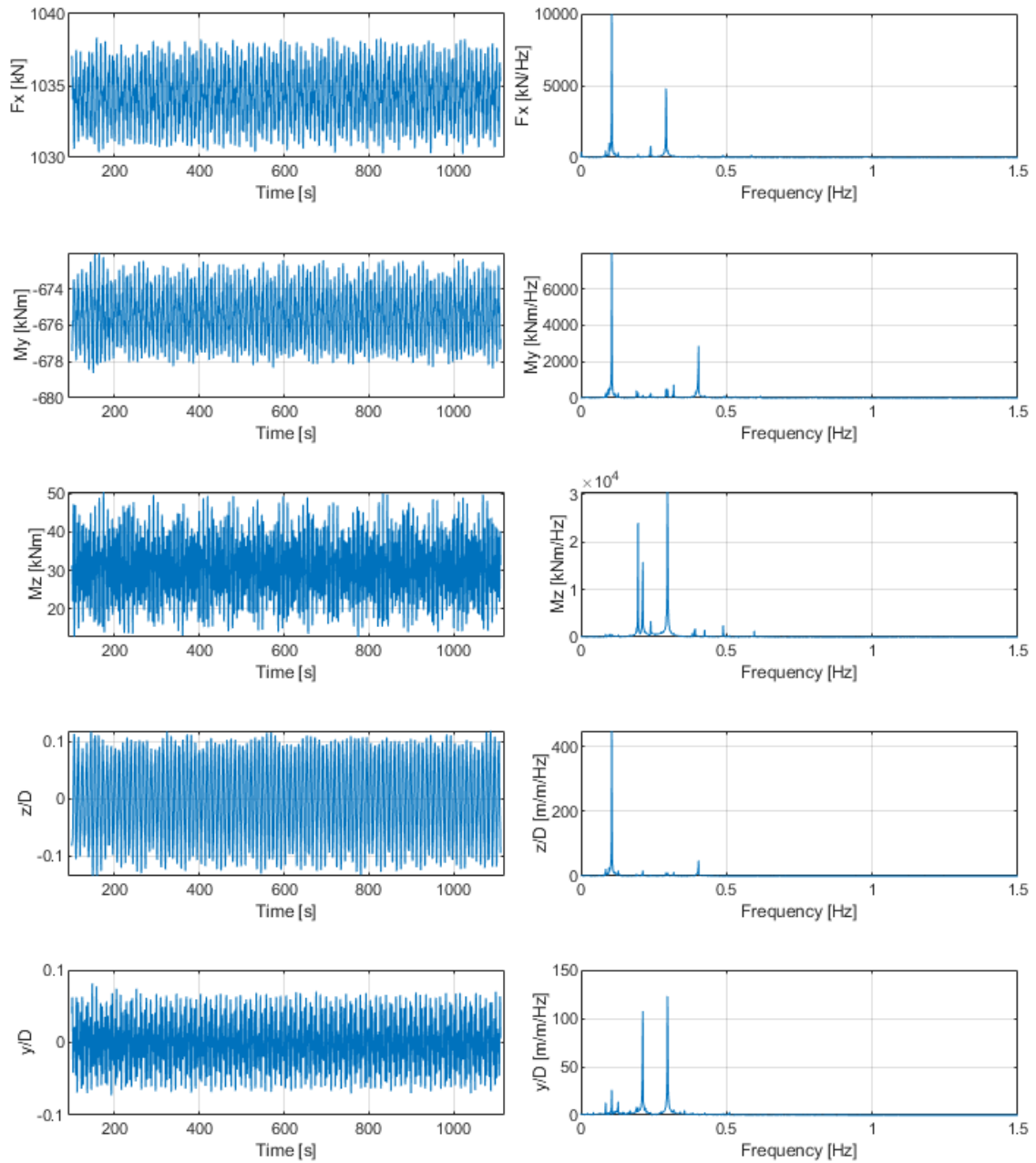ormalized with respect to diameter cross-flow and in-line response amplitude at node 512 (midspan), respectively. 0.0545 m/s current velocity 90° relative to geographic North.
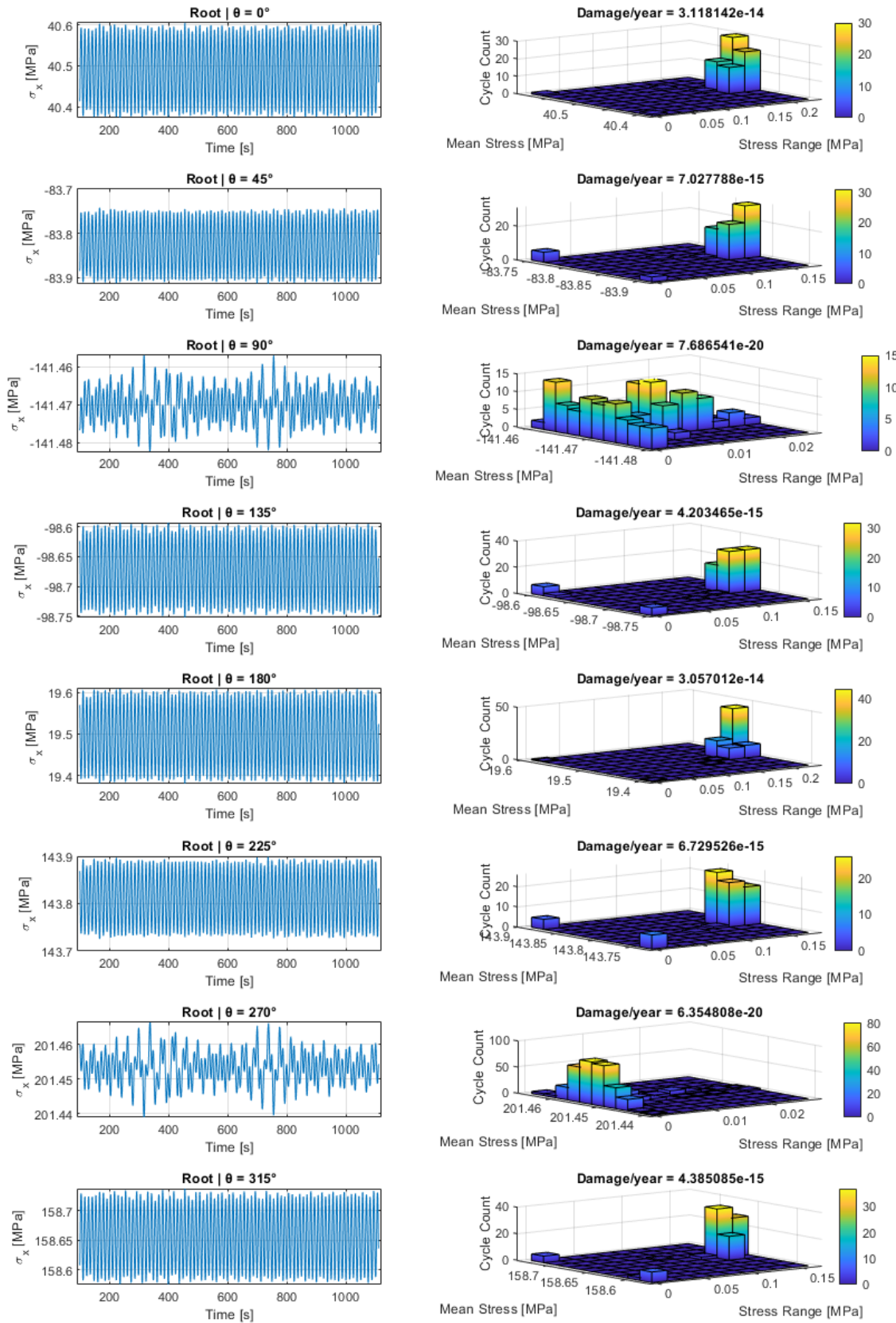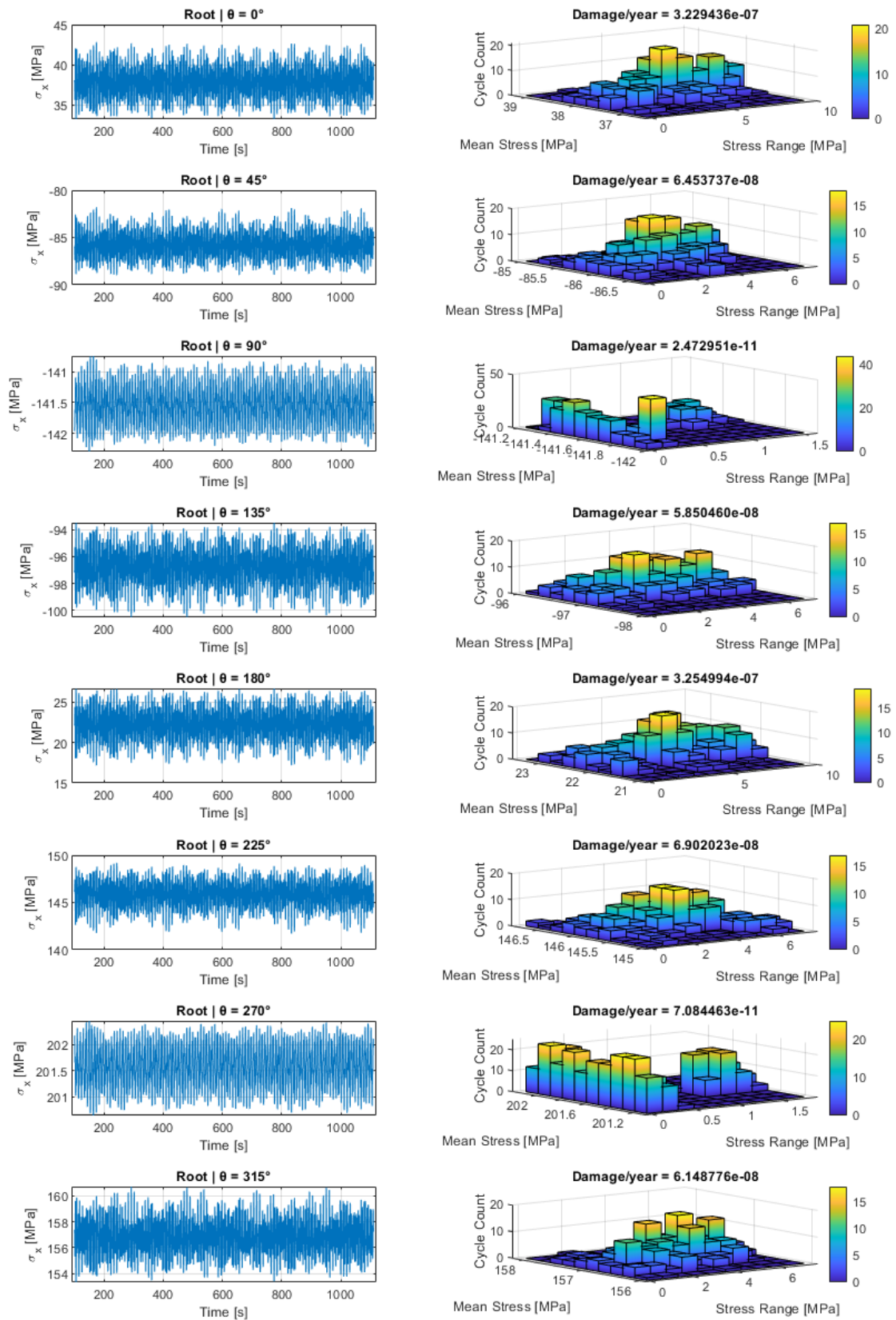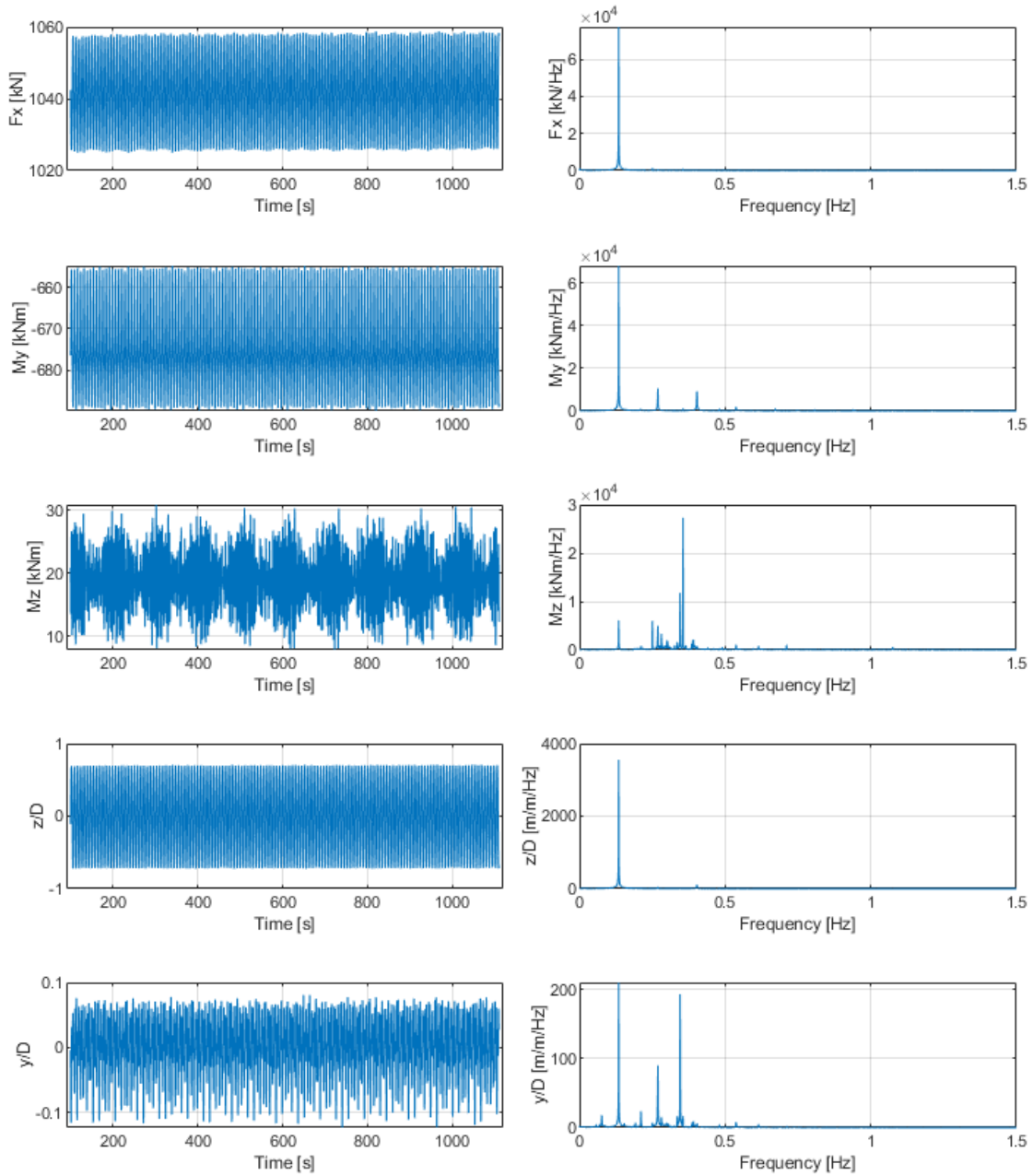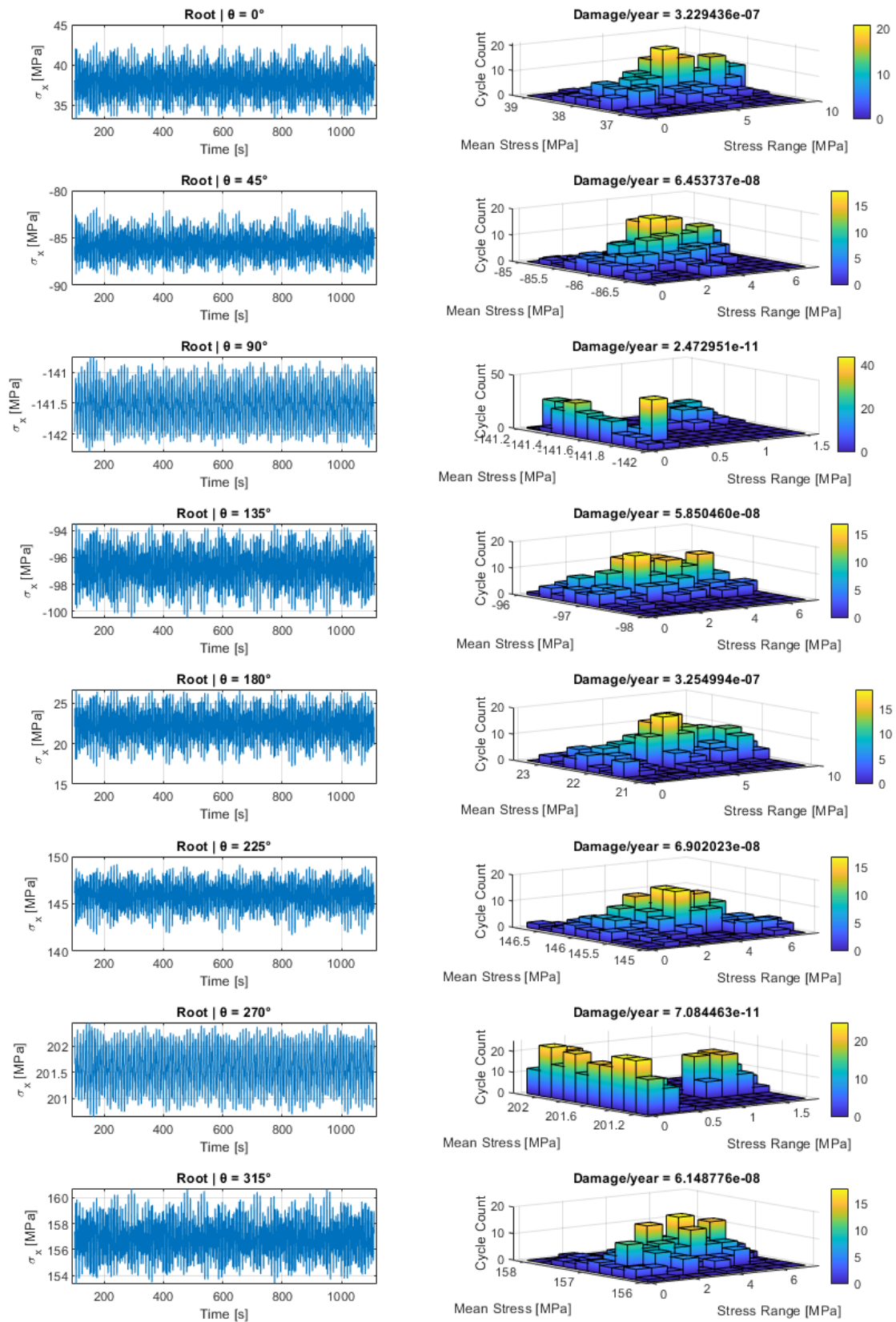
Figure 10.17: Longitudinal stress history at root position for different θ-angles around the pipeline cross-section to the left. Corresponding Rainflow counting and fatigue damage/y (current probability of occurrence included) to the right. 0.0545 m/s current velocity 90° relative to geographic North.
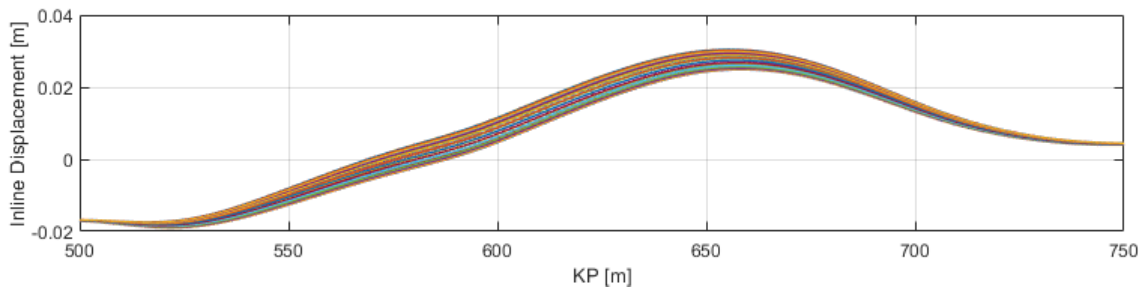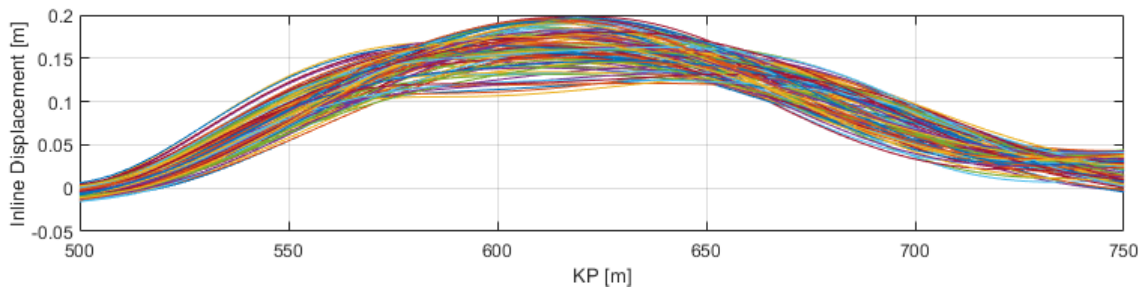
Figure 10.18: In-line displacement pattern. 0.0545 m/s current velocity 90° relative to geographic North.
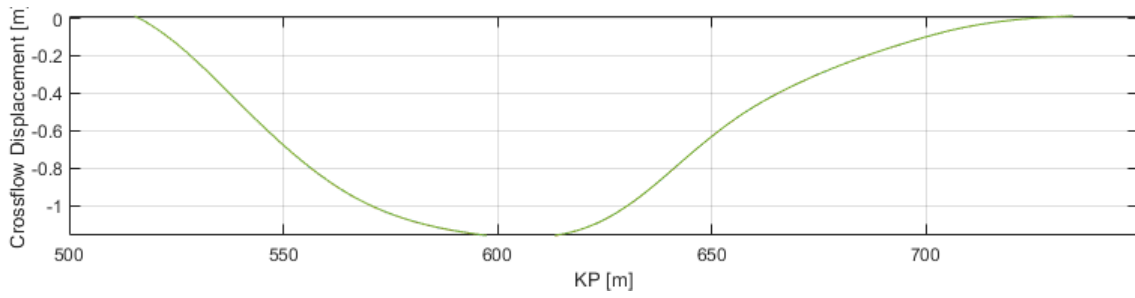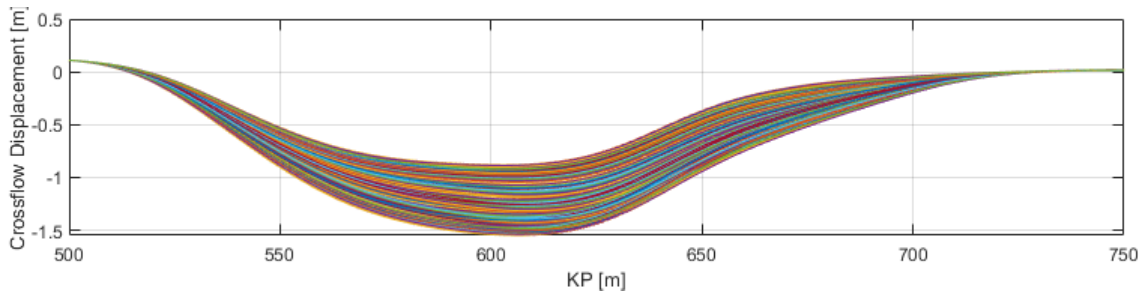

Figure 10.19: Cross-flow displacement pattern. 0.0545 m/s current velocity 90° relative to geographic North.
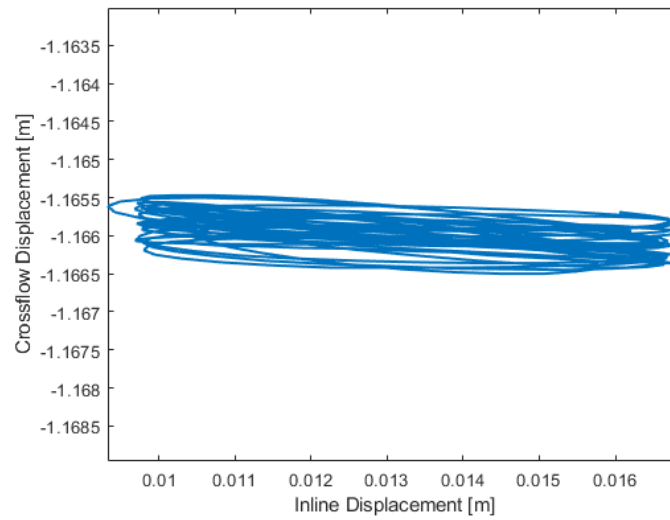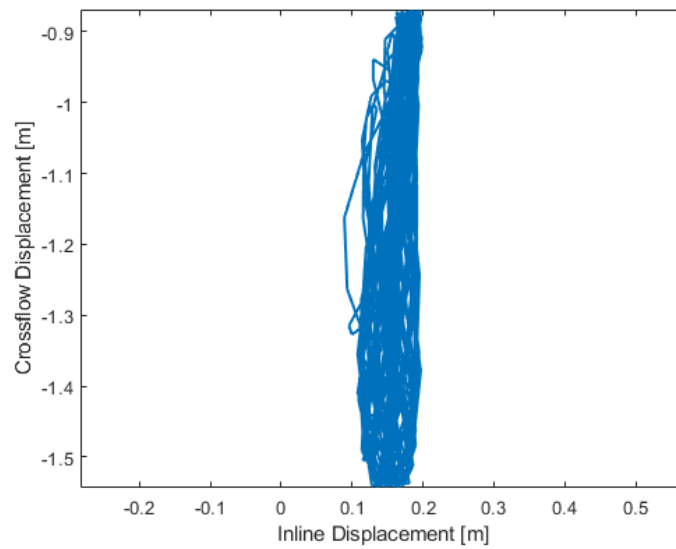

Figure 10.20: Combined in-line and cross-flow displacement pattern at midspan. 0.0545 m/s current velocity 90° relative to geographic North.

0.1145 m/s
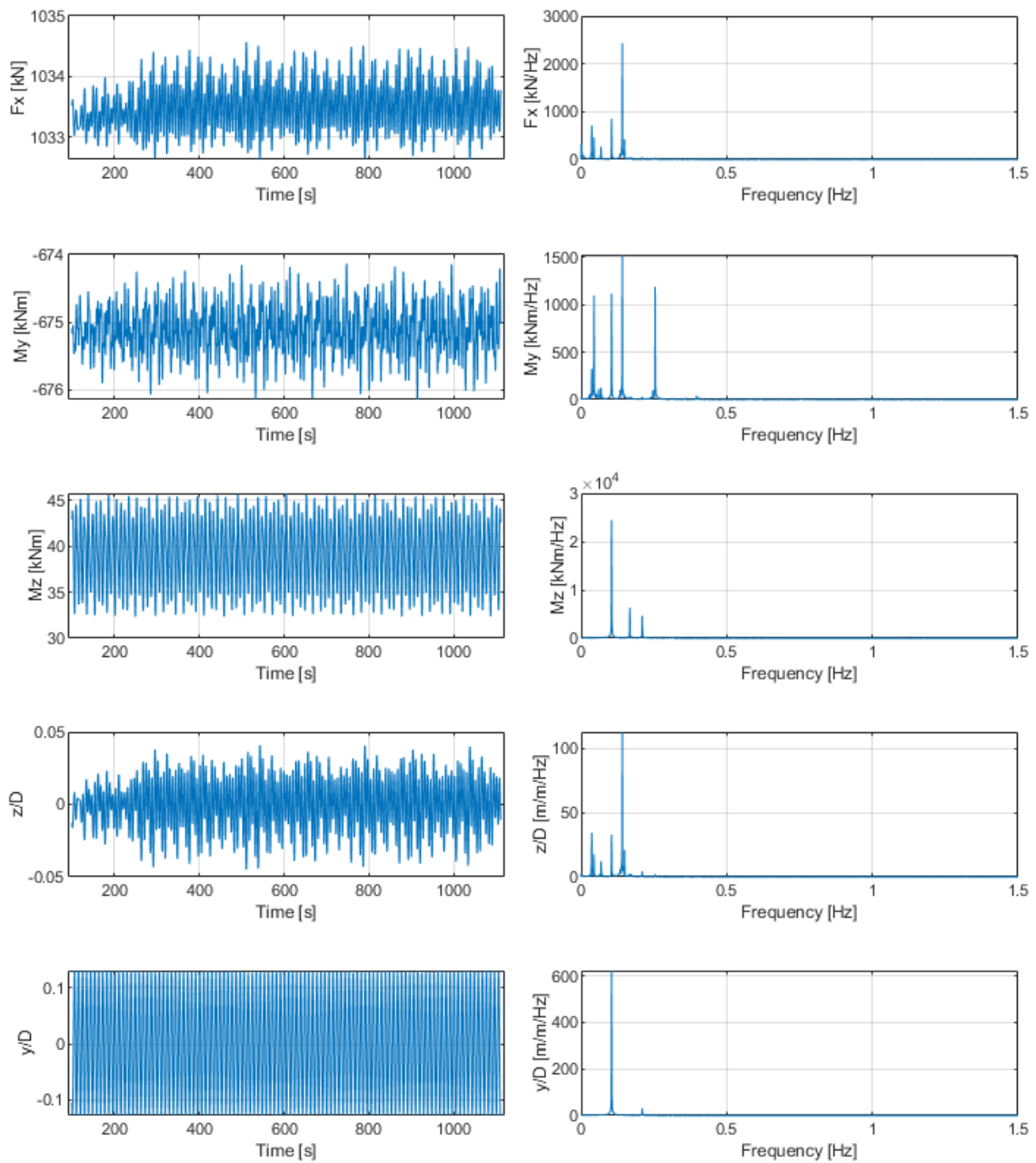
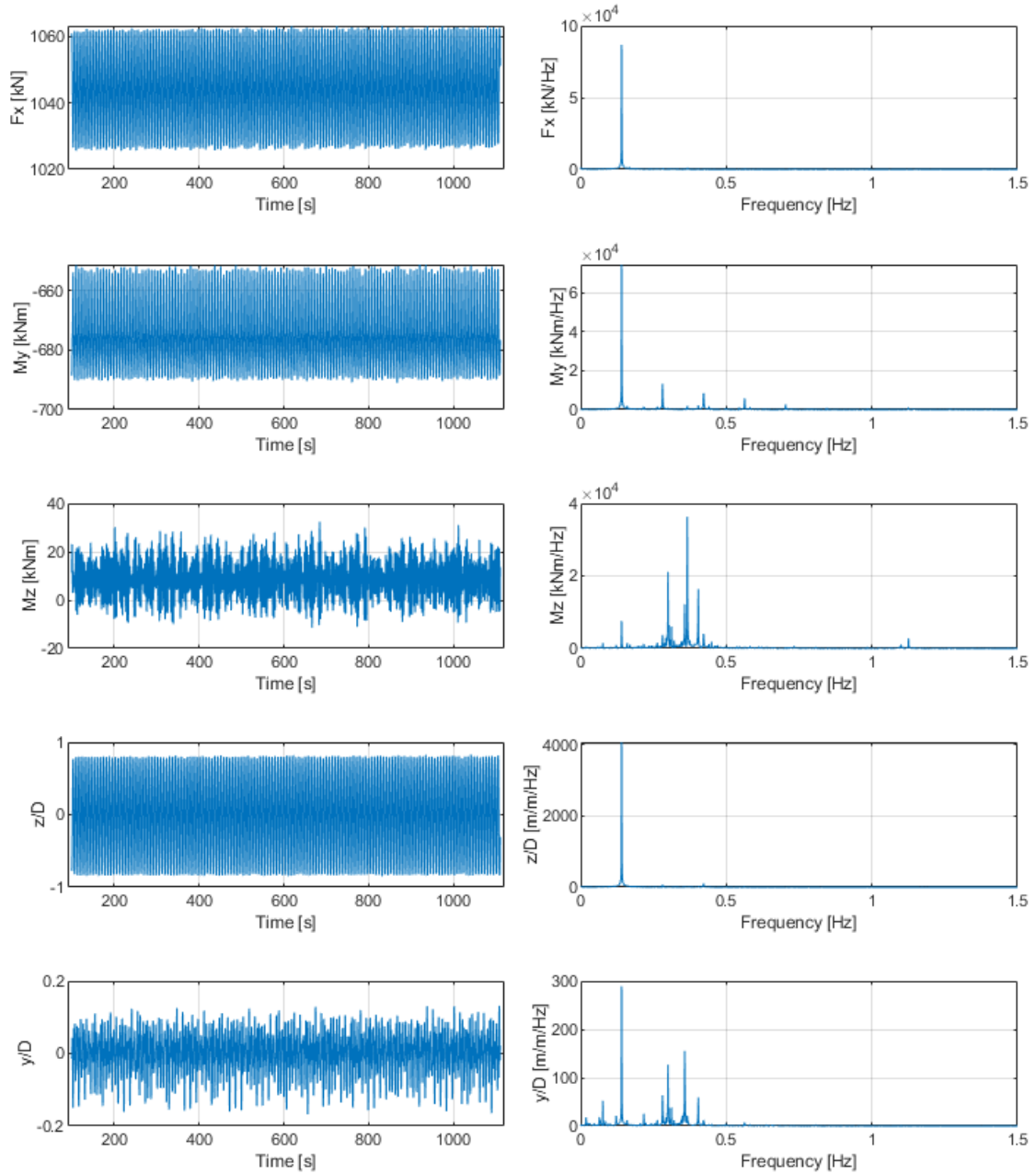Figure 10.21: Time histories and FFT of axial force, Fx, cross-flow bending moment, My, and in-line bending moment, Mz, at shoulder element 342. z/D and y/D are normalized with respect to diameter cross-flow and in-line response amplitude at node 512 (midspan), respectively. 0.1145 m/s current velocity 90° relative to geographic North.
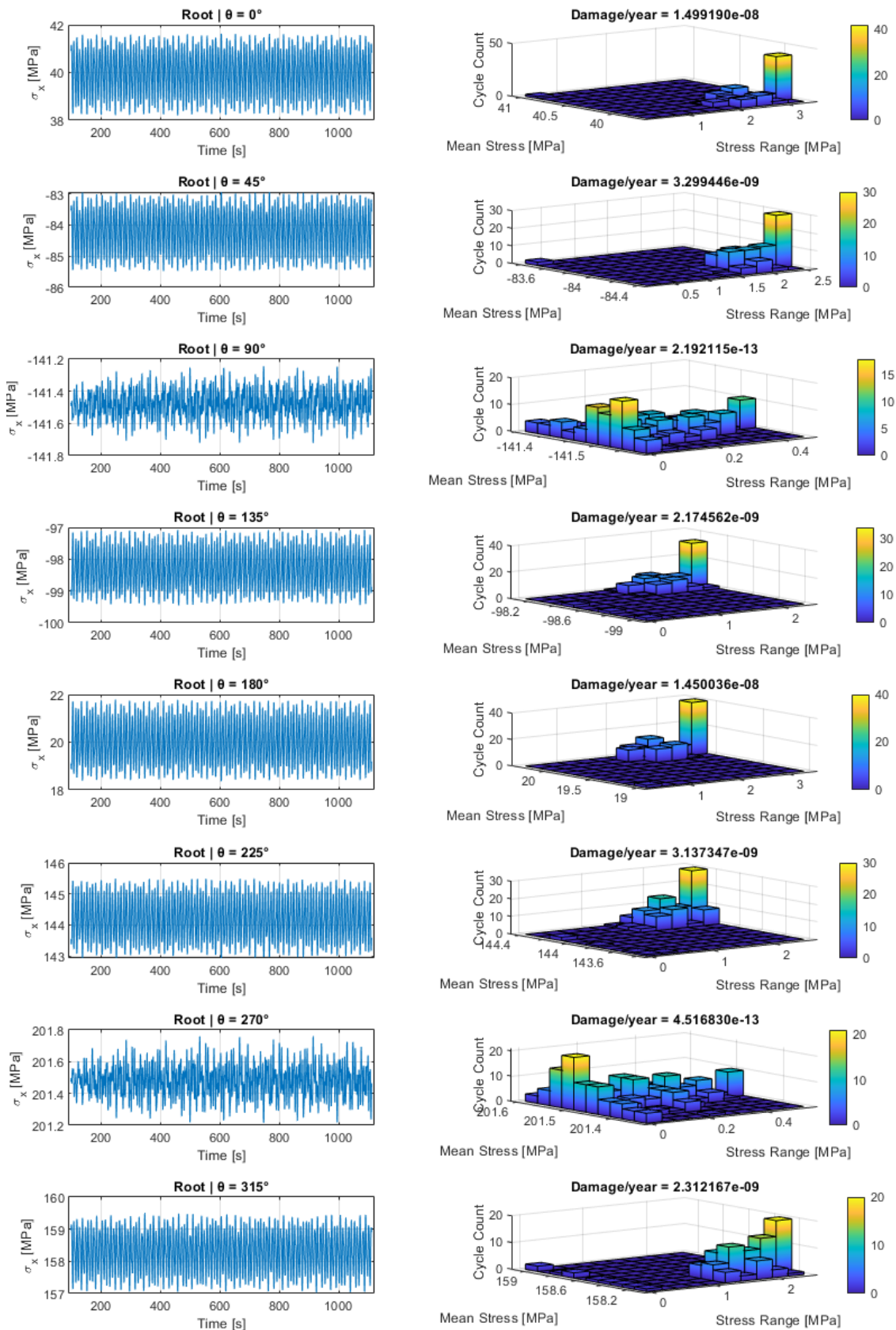
Figure 10.22: Longitudinal stress history at root position for different θ-angles around the pipeline cross-section to the left. Corresponding Rainflow counting and fatigue damage/y (current probability of occurrence included) to the right. 0.1145 m/s current velocity 90° relative to geographic North.
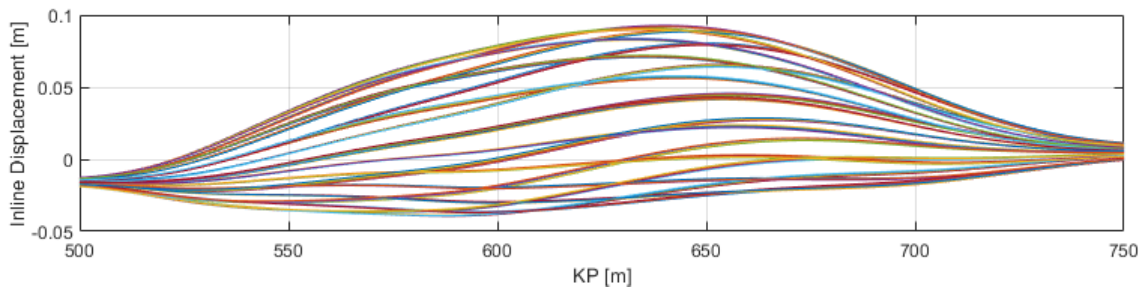
Figure 10.23: In-line displacement pattern. 0.1145 m/s current velocity 90° relative to geographic North
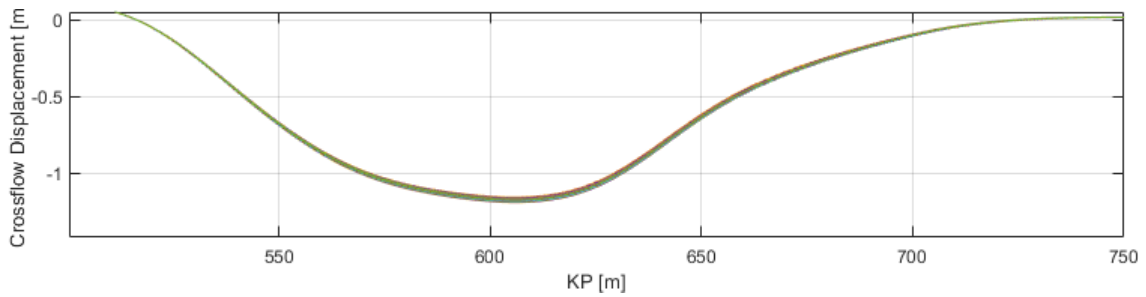
Figure 10.24: Cross-flow displacement pattern. 0.1145 m/s current velocity 90° relative to geographic North.
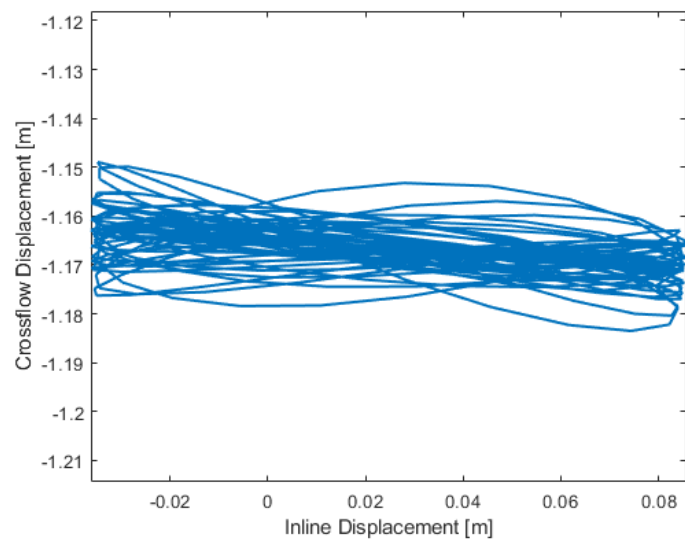
Figure 10.25: Combined in-line and cross-flow displacement pattern at midspan. 0.1145 m/s current velocity 90° relative to geographic North.

0.1745 m/s
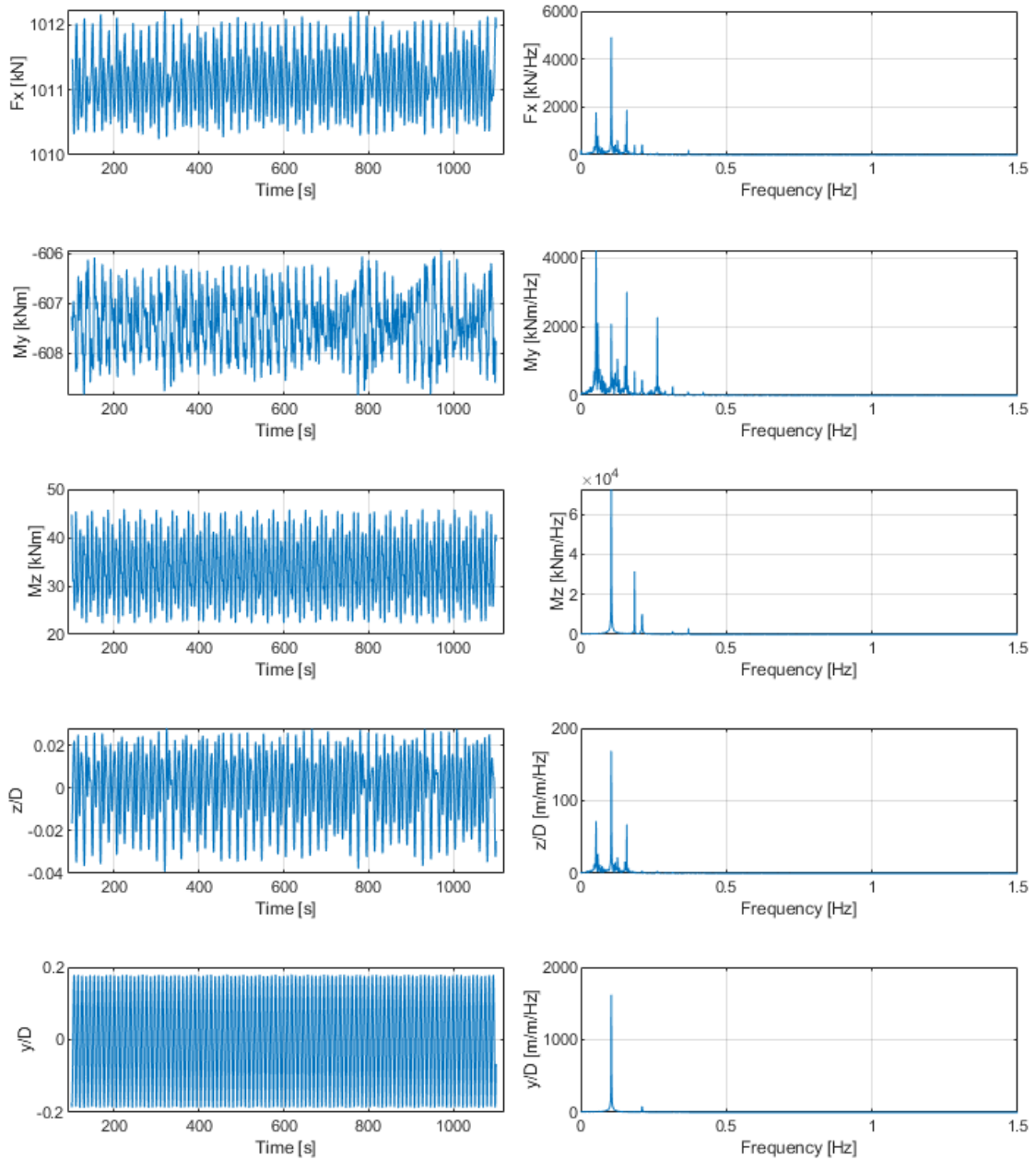
Figure 10.26: Time histories and FFT of axial force, Fx, cross-flow bending moment, My, and in-line bending moment, Mz, at shoulder element 342. z/D and y/D are normalized with respect to diameter cross-flow and in-line response amplitude at node 512 (midspan), respectively. 0.1745 m/s current velocity 90° relative to geographic North.
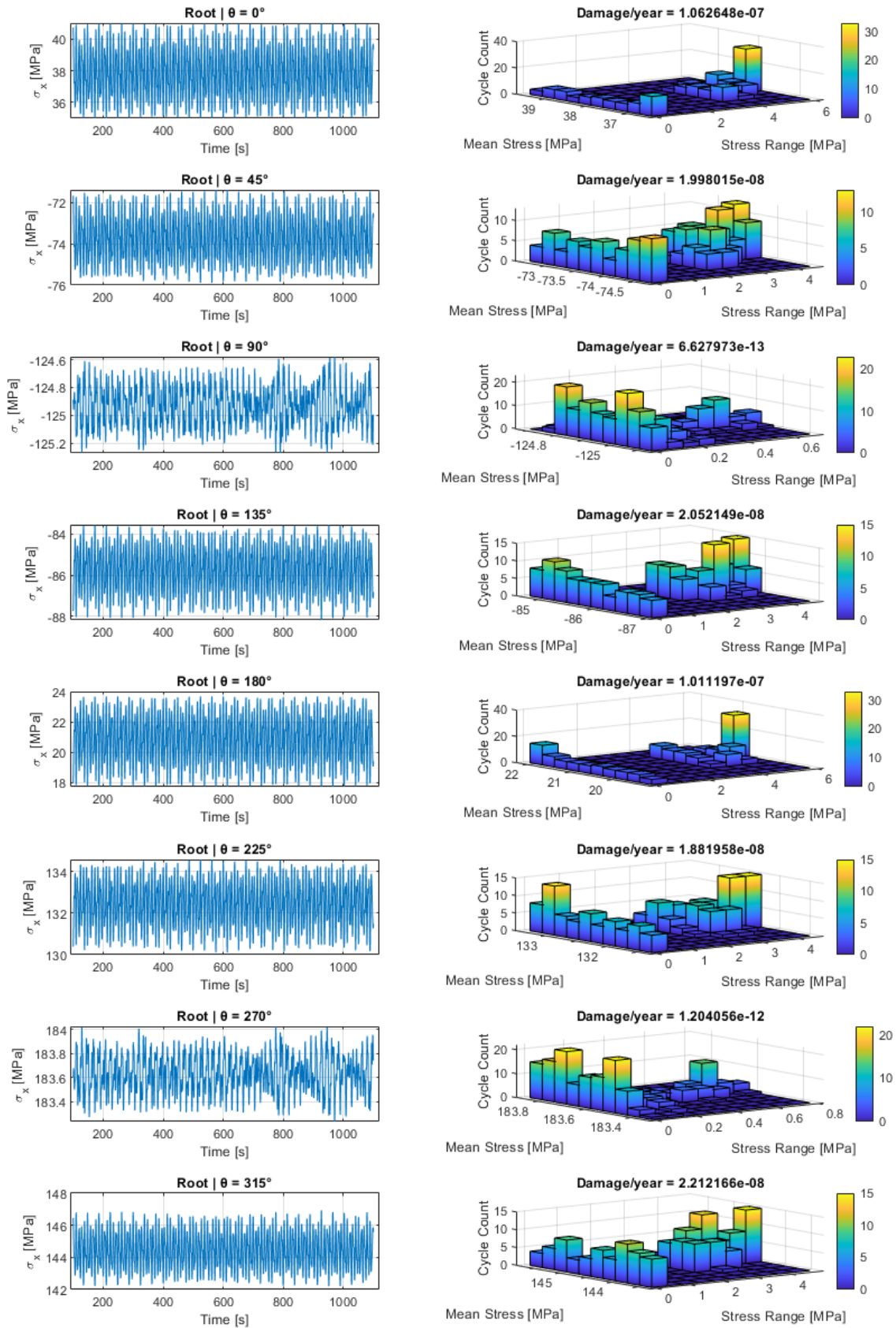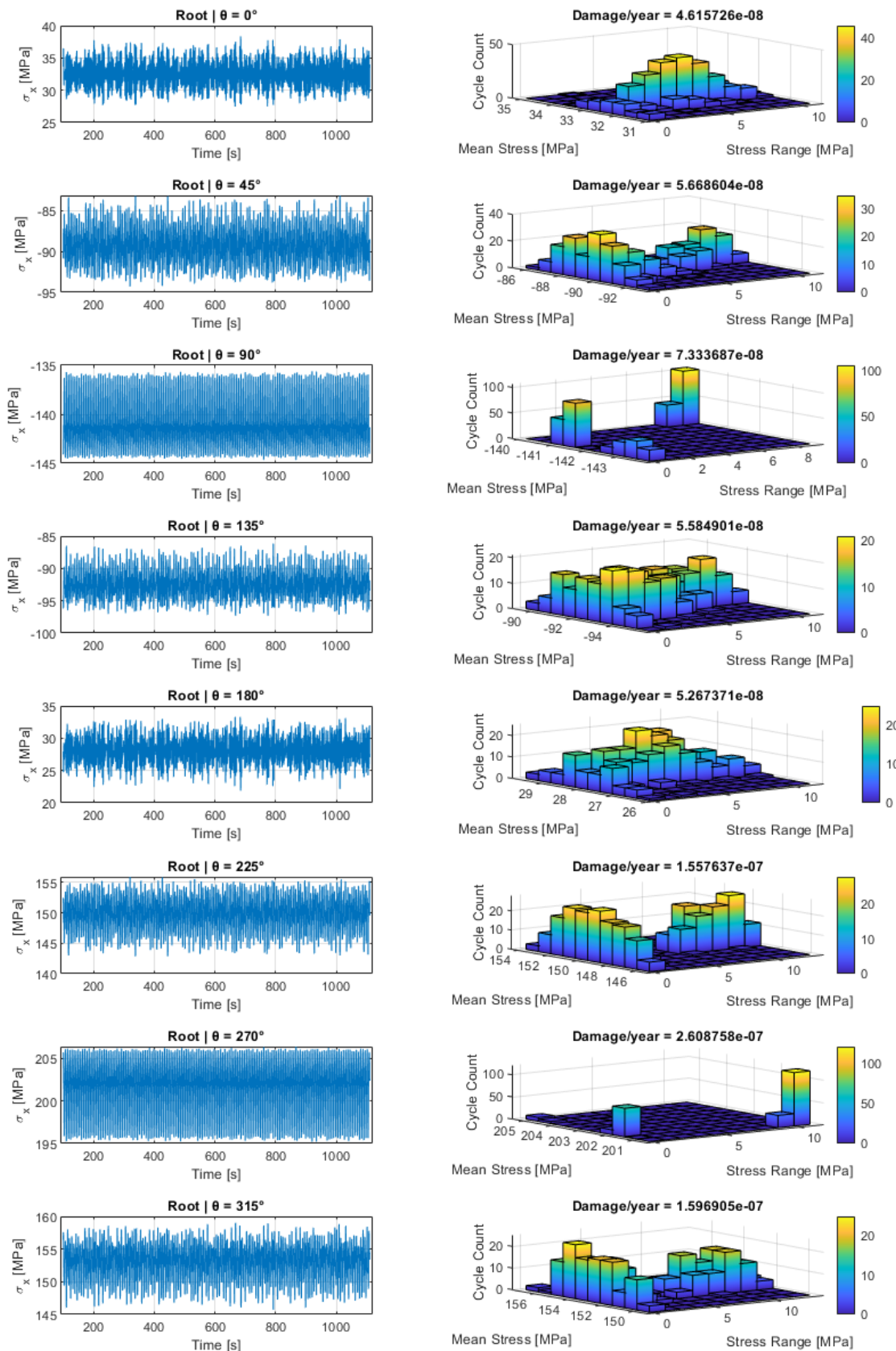
Figure 10.27: Longitudinal stress history at root position for different θ-angles around the pipeline cross-section to the left. Corresponding Rainflow counting and fatigue damage/y (current probability of occurrence included) to the right. 0.1745 m/s current velocity 90° relative to geographic North.
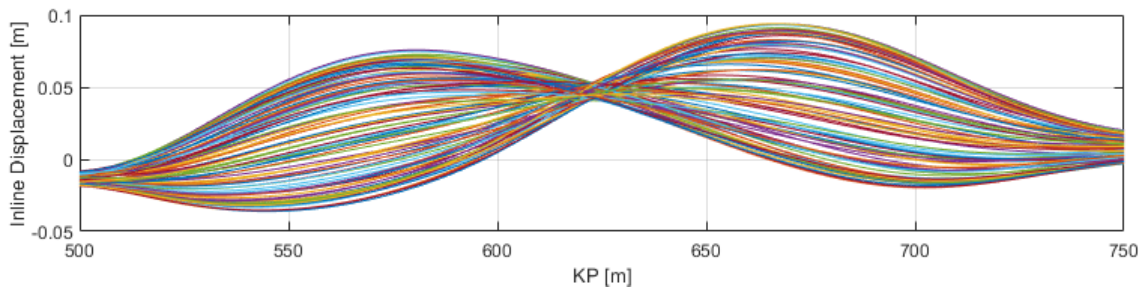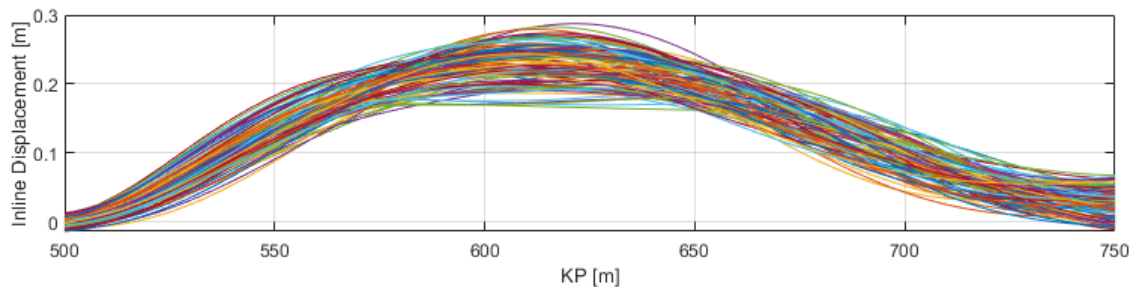
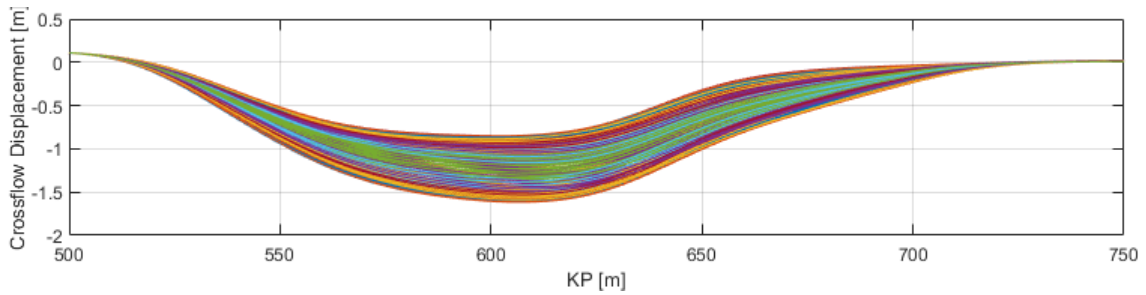Figure 10.28: In-line displacement pattern. 0.1745 m/s current velocity 90° relative to geographic North
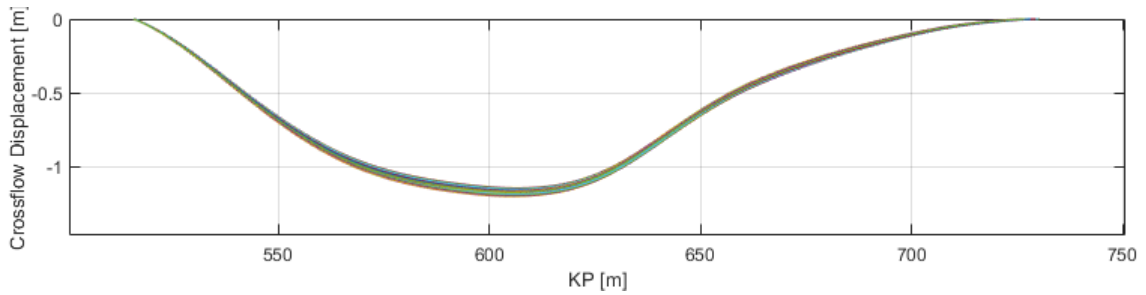
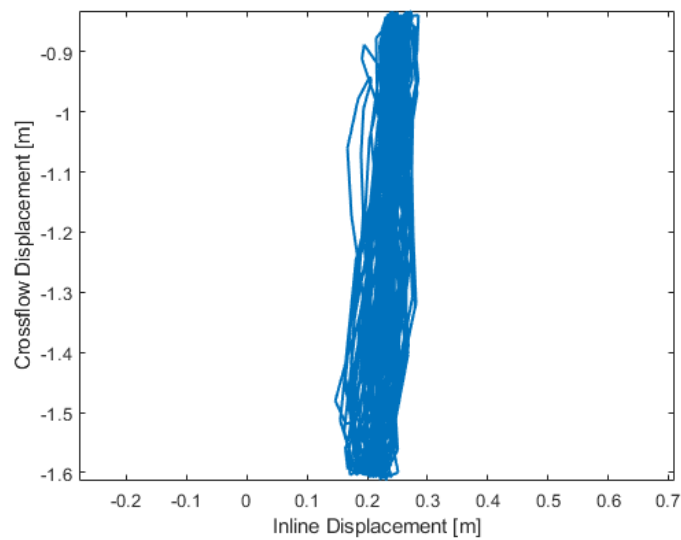Figure 10.29: Cross-flow displacement pattern. 0.1745 m/s current velocity 90° relative to geographic North.
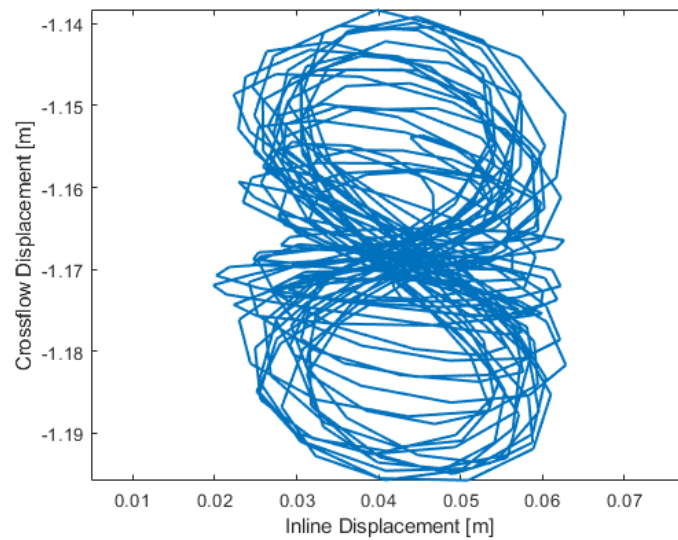
Figure 10.30: Combined in-line and cross-flow displacement pattern at midspan. 0.1745 m/s current velocity 90° relative to geographic North.

0.2345 m/s
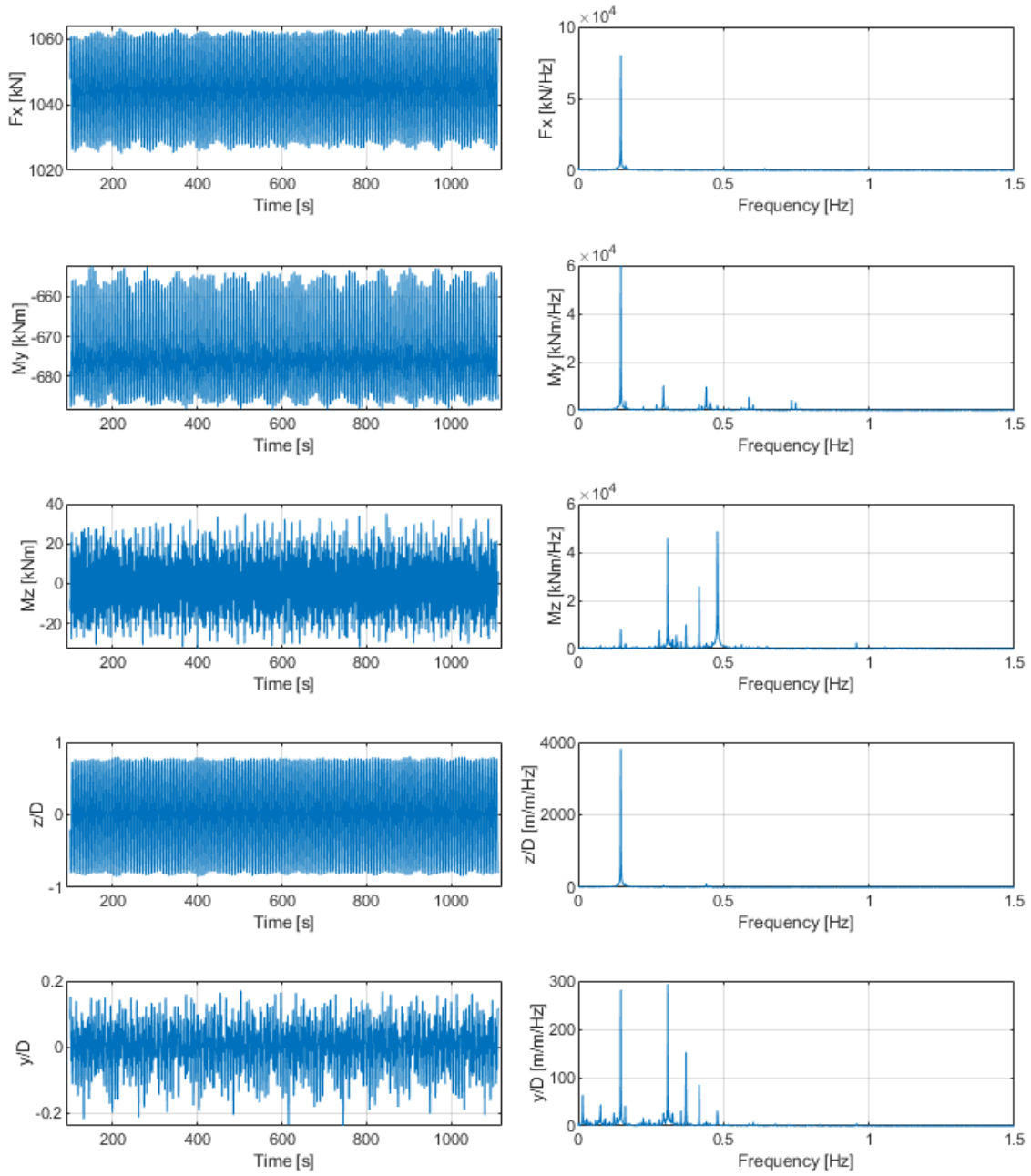

Figure 10.31: Time histories and FFT of axial force, Fx, cross-flow bending moment, My, and in-line bending moment, Mz, at shoulder element 342. z/D and y/D are normalized with respect to diameter cross-flow and in-line response amplitude at node 512 (midspan), respectively. 0.2345 m/s current velocity 90° relative to geographic North.
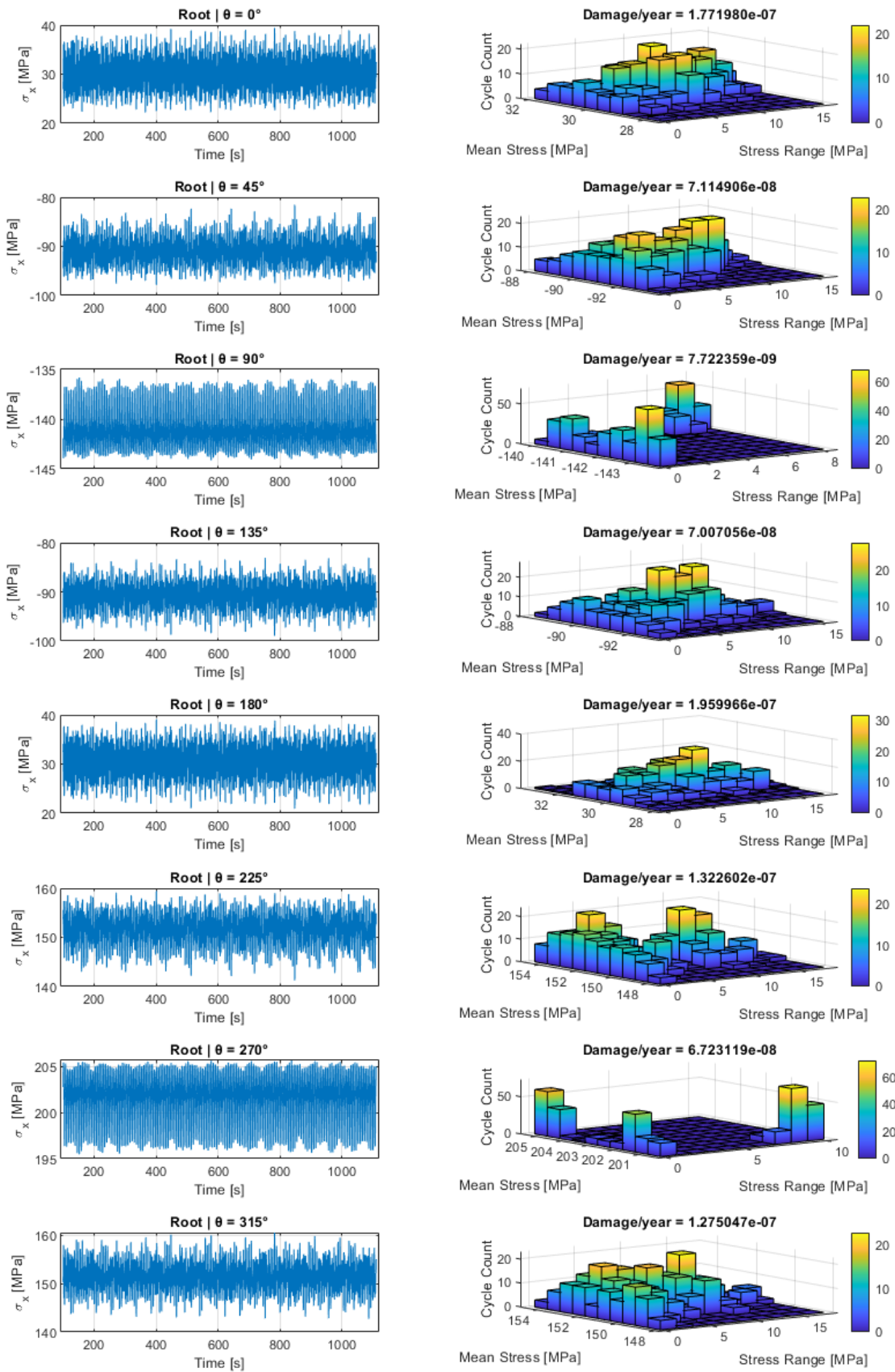
Figure 10.32: Longitudinal stress history at root position for different θ-angles around the pipeline cross-section to the left. Corresponding Rainflow counting and fatigue damage/y (current probability of occurrence included) to the right. 0.2345 m/s current velocity 90° relative to geographic North.
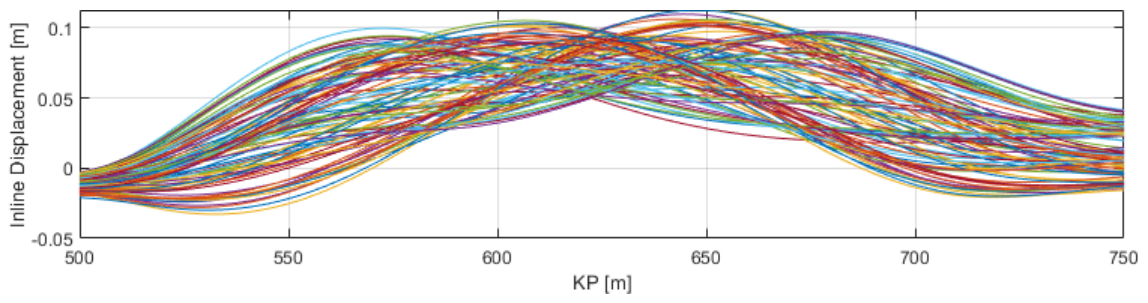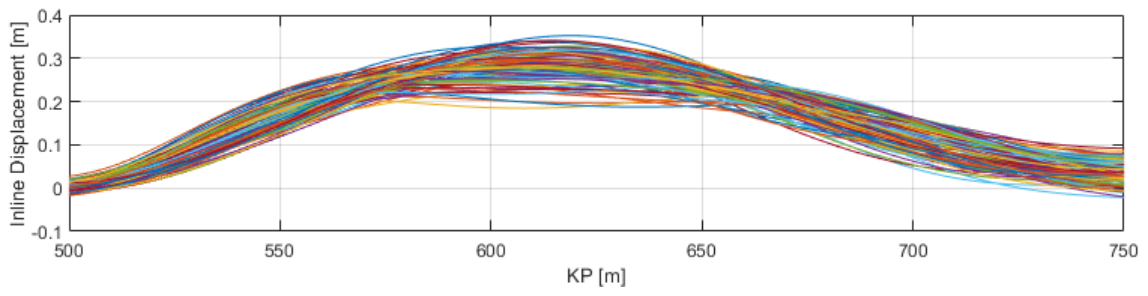
Figure 10.33: In-line displacement pattern. 0.2345 m/s current velocity 90° relative to geographic North.
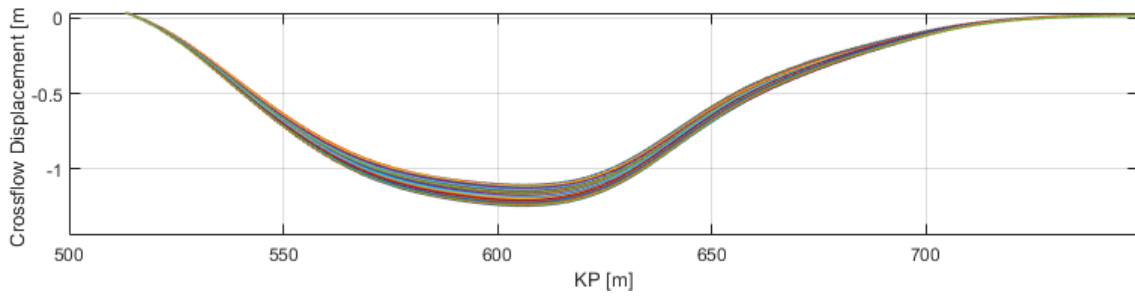
Figure 10.34: Cross-flow displacement pattern. 0.2345 m/s current velocity 90° relative to geographic North.
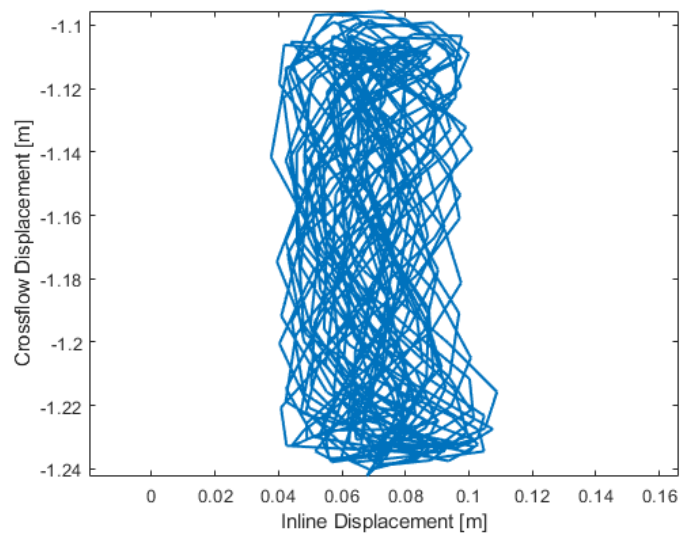
Figure 10.35: Combined in-line and cross-flow displacement pattern at midspan. 0.2345 m/s current velocity 90° relative to geographic North.

0.2945 m/s

Figure 10.36: Time histories and FFT of axial force, Fx, cross-flow bending moment, My, and in-line bending moment, Mz, at shoulder element 342. z/D and y/D are normalized with respect to diameter cross-flow and in-line response amplitude at node 512 (midspan), respectively. 0.2945 m/s current velocity 90° relative to geographic North.

Figure 10.37: Longitudinal stress history at root position for different θ-angles around the pipeline cross-section to the left. Corresponding Rainflow counting and fatigue damage/y (current probability of occurrence included) to the right. 0.2945 m/s current velocity 90° relative to geographic North.

Figure 10.38: In-line displacement pattern. 0.2945 m/s current velocity 90° relative to geographic North.
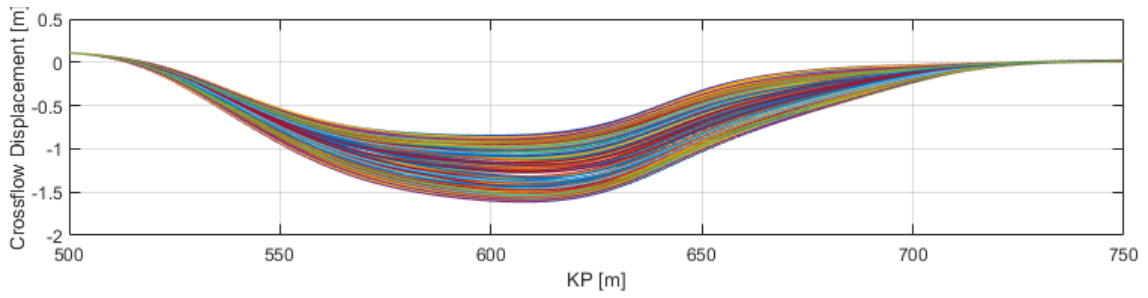

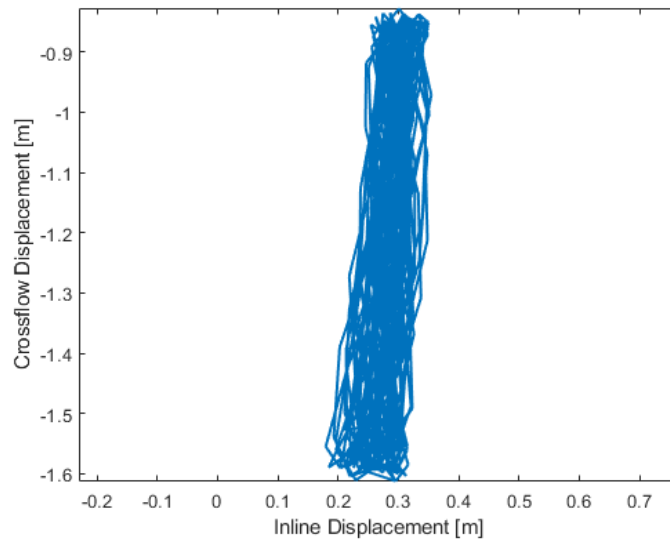Figure 10.39: Cross-flow displacement pattern. 0.2945 m/s current velocity 90° relative to geographic North.

Figure 10.40: Combined in-line and cross-flow displacement pattern at midspan. 0.2945 m/s current velocity 90° relative to geographic North.

0.3545 m/s

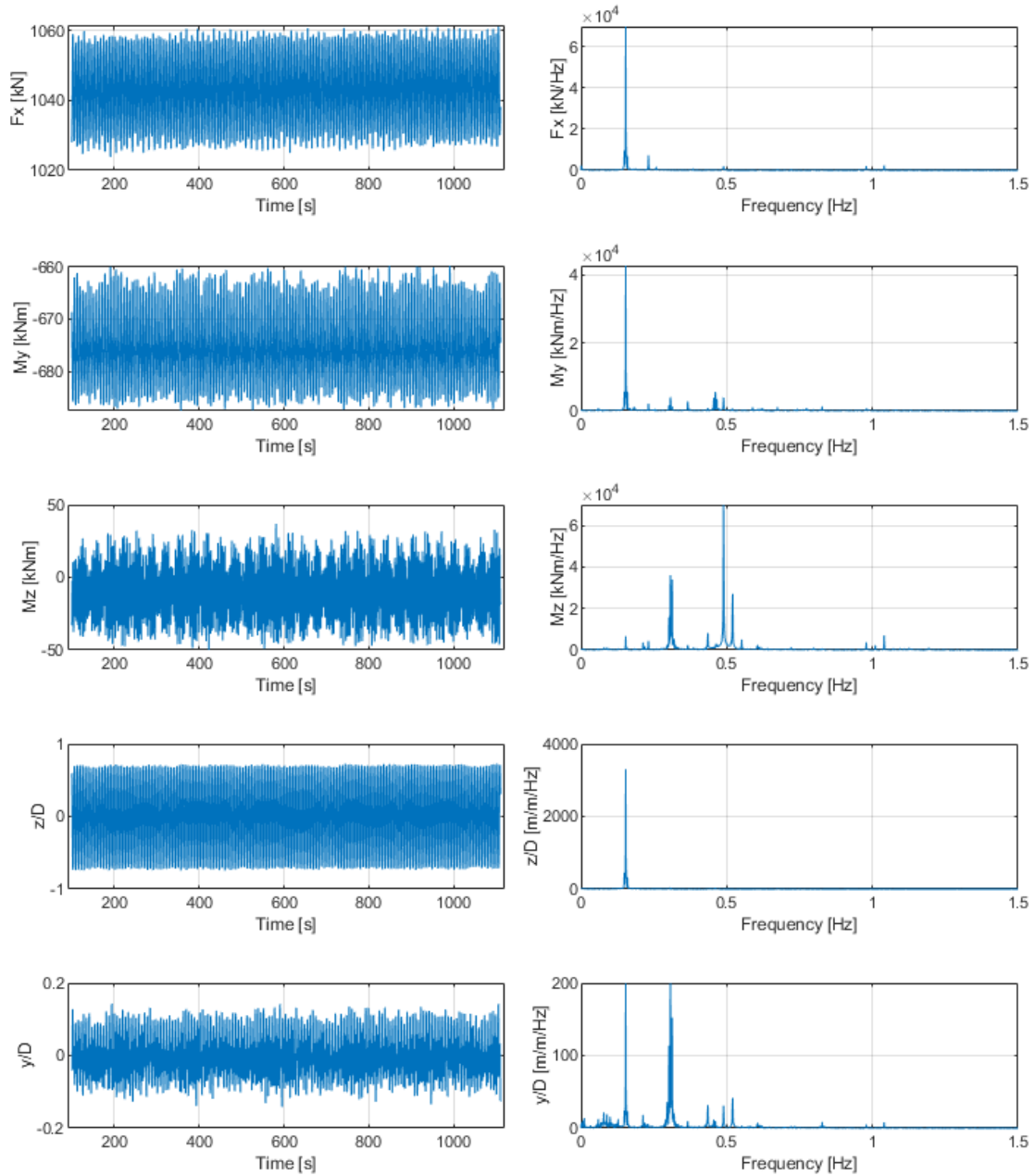Figure 10.41: Time histories and FFT of axial force, Fx, cross-flow bending moment, My, and in-line bending moment, Mz, at shoulder element 342. z/D and y/D are normalized with respect to diameter cross-flow and in-line response amplitude at node 512 (midspan), respectively. 0.3545 m/s current velocity 90° relative to geographic North.
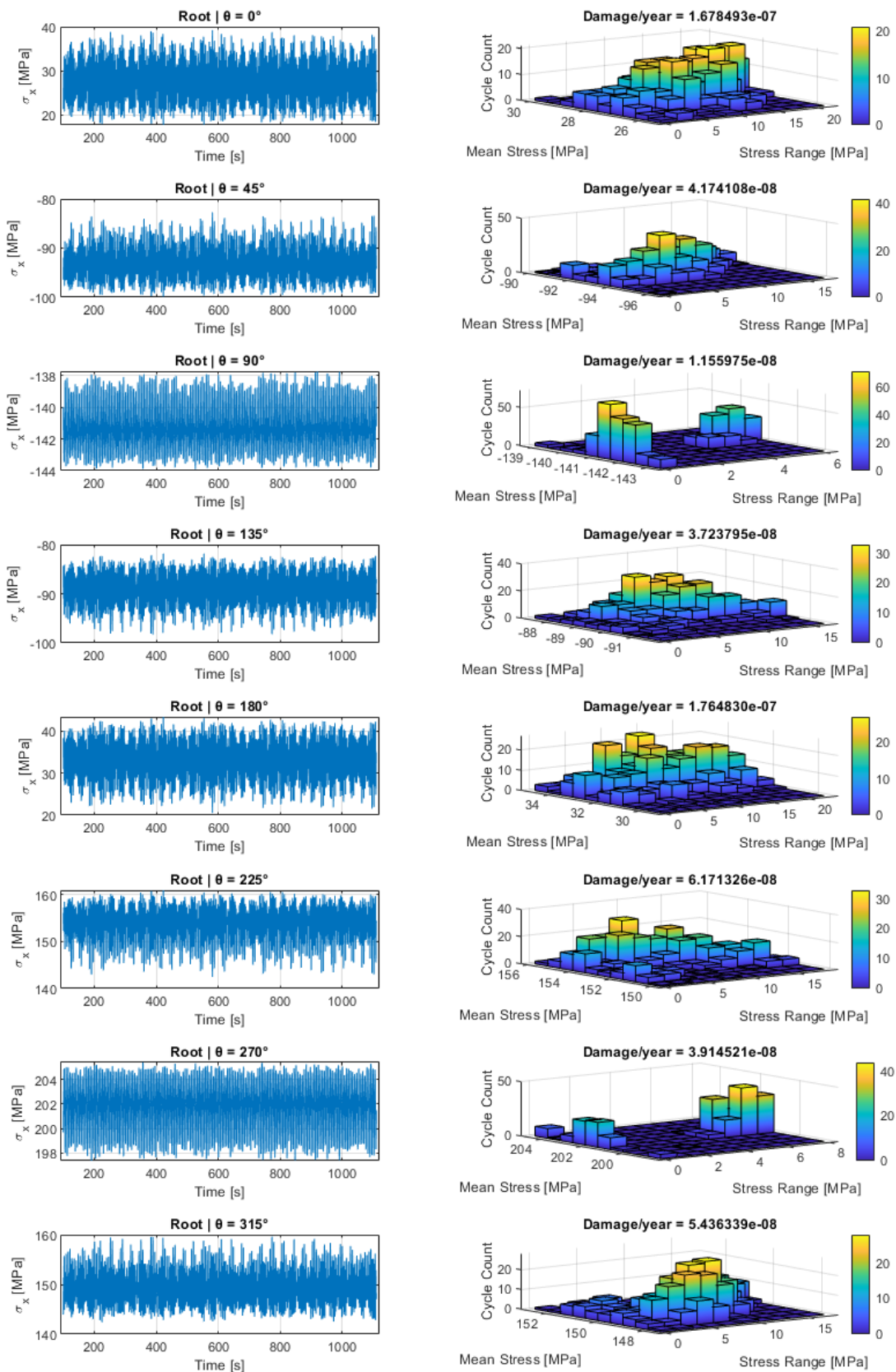
Figure 10.42: Longitudinal stress history at root position for different θ-angles around the pipeline cross-section to the left. Corresponding Rainflow counting and fatigue damage/y (current probability of occurrence included) to the right. 0.3545 m/s current velocity 90° relative to geographic North.
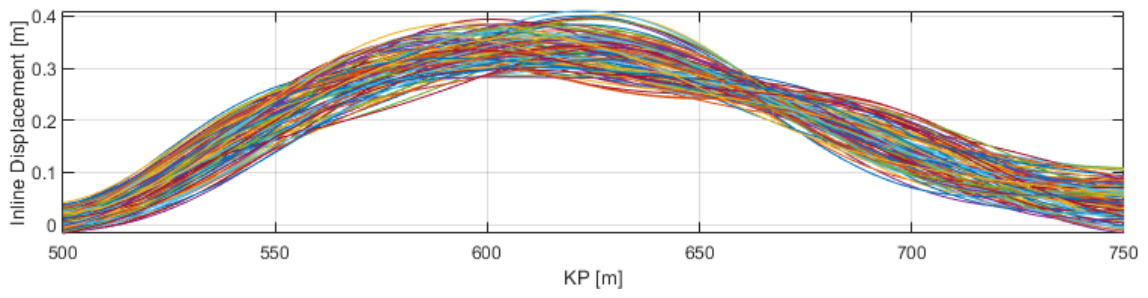
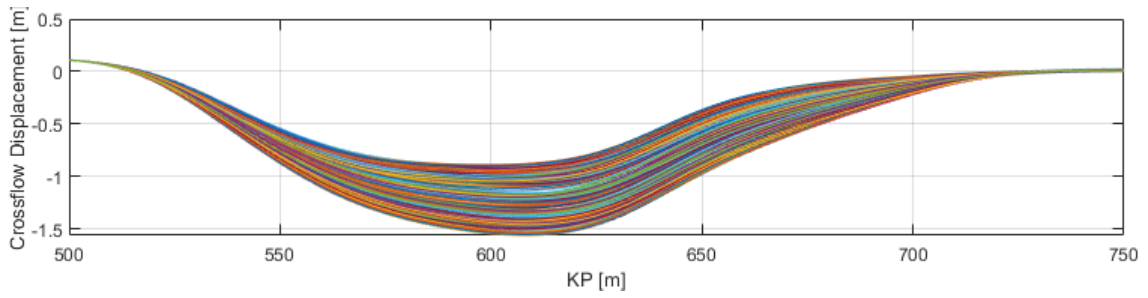Figure 10.43: In-line displacement pattern. 0.3545 m/s current velocity 90° relative to geographic North.

Figure 10.44: Cross-flow displacement pattern. 0.3545 m/s current velocity 90° relative to geographic North.
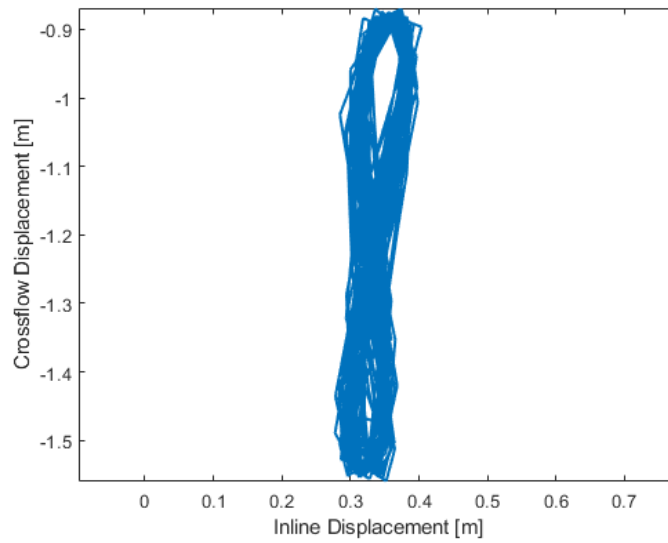

Figure 10.45: Combined in-line and cross-flow displacement pattern at midspan. 0.3545 m/s current velocity 90° relative to geographic North.

0.4145 m/s
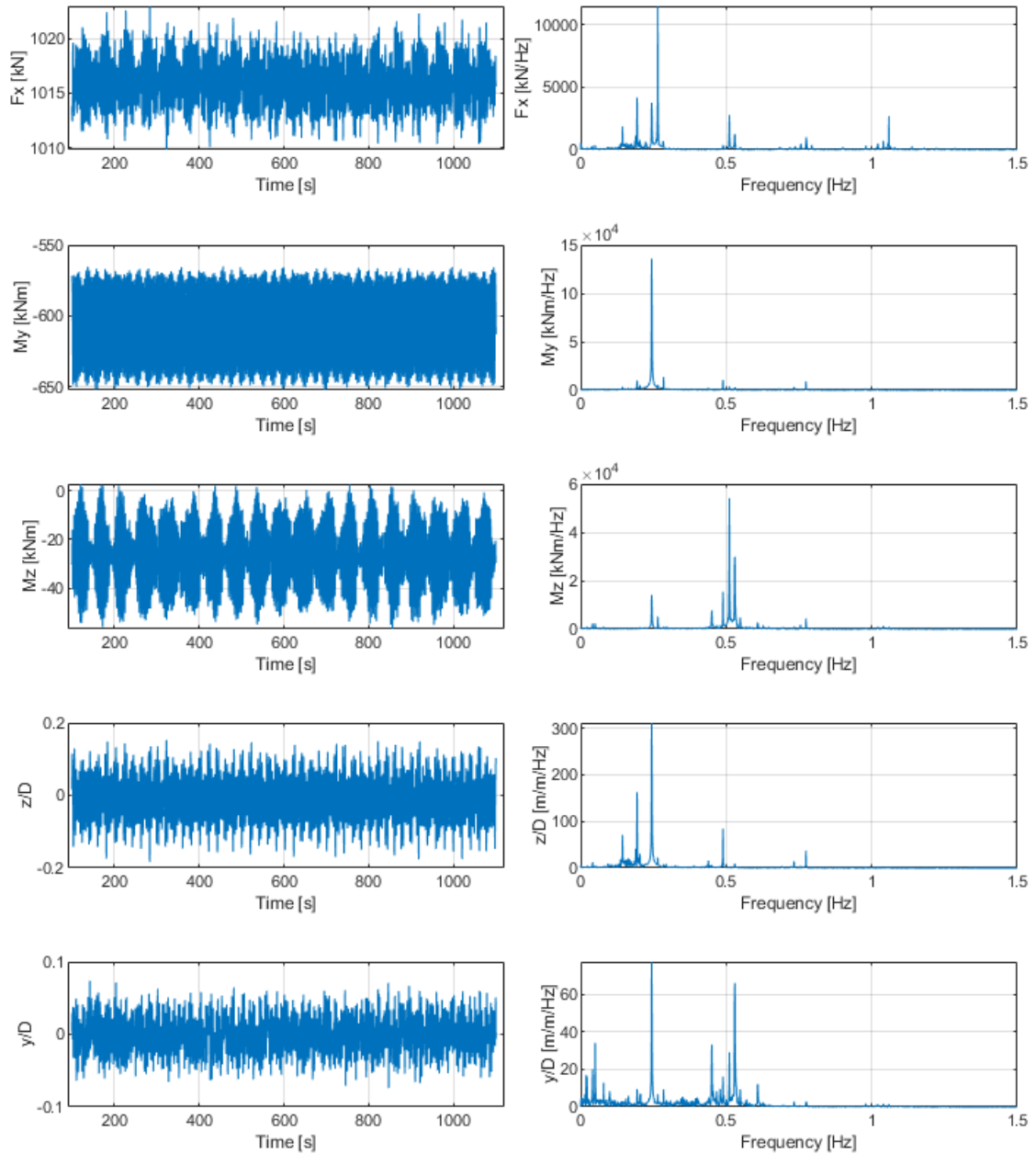

Figure 10.46: Time histories and FFT of axial force, Fx, cross-flow bending moment, My, and in-line bending moment, Mz, at shoulder element 342. z/D and y/D are normalized with respect to diameter cross-flow and in-line response amplitude at node 512 (midspan), respectively. 0.4145 m/s current velocity 90° relative to geographic North.

Figure 10.47: Longitudinal stress history at root position for different θ-angles around the pipeline cross-section to the left. Corresponding Rainflow counting and fatigue damage/y (current probability of occurrence included) to the right. 0.4145 m/s current velocity 90° relative to geographic North.

Figure 10.48: In-line displacement pattern. 0.4145 m/s current velocity 90° relative to geographic North.

Figure 10.49: Cross-flow displacement pattern. 0.4145 m/s current velocity 90° relative to geographic North.

Figure 10.50: Combined in-line and cross-flow displacement pattern at midspan. 0.4145 m/s current velocity 90° relative to geographic North.

0.4745 m/s

Figure 10.51: Time histories and FFT of axial force, Fx, cross-flow bending moment, My, and in-line bending moment, Mz, at shoulder element 342. z/D and y/D are normalized with respect to diameter cross-flow and in-line response amplitude at node 512 (midspan), respectively. 0.4745 m/s current velocity 90° relative to geographic North.
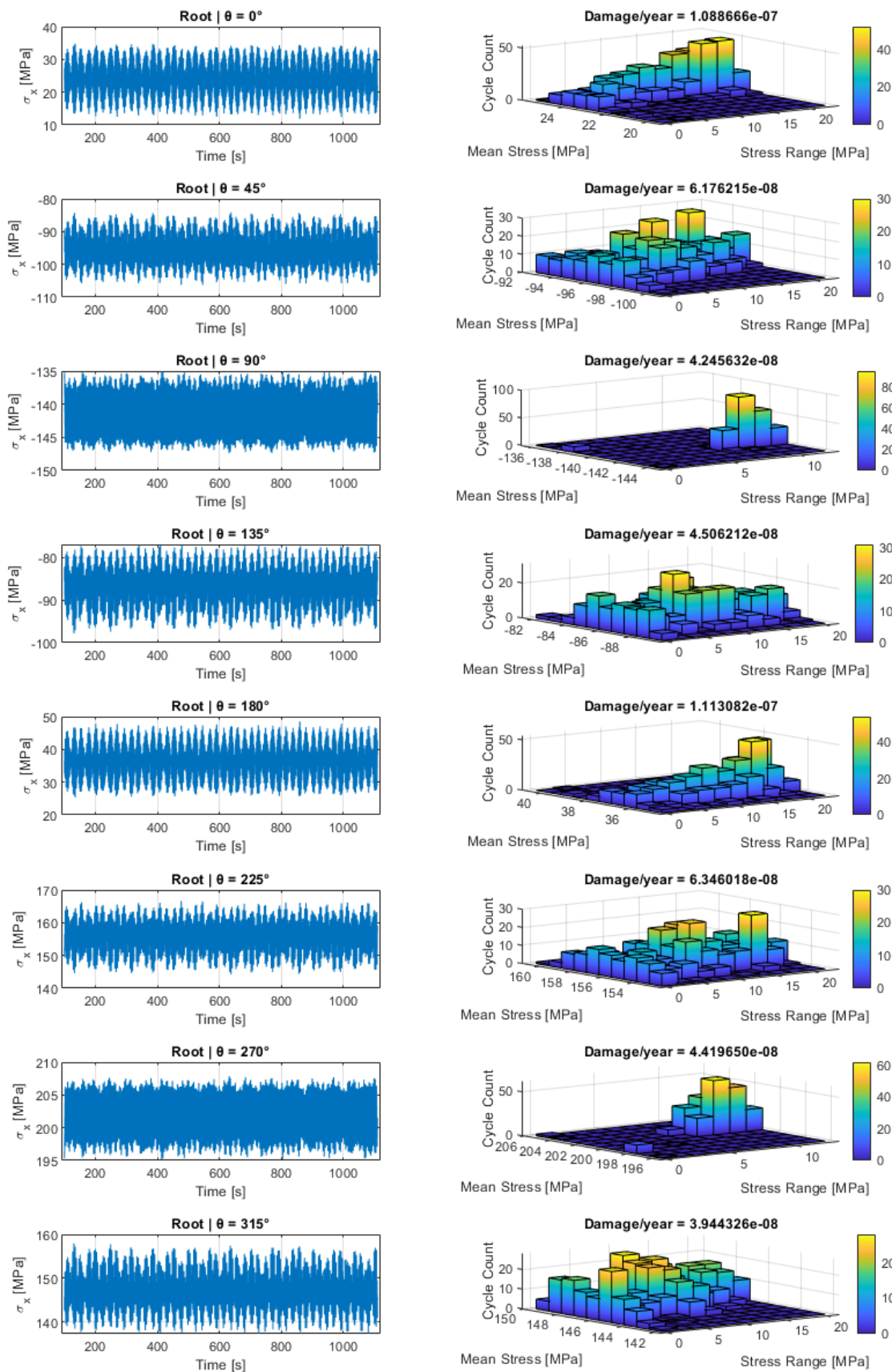
Figure 10.52: Longitudinal stress history at root position for different θ-angles around the pipeline cross-section to the left. Corresponding Rainflow counting and fatigue damage/y (current probability of occurrence included) to the right. 0.4745 m/s current velocity 90° relative to geographic North.
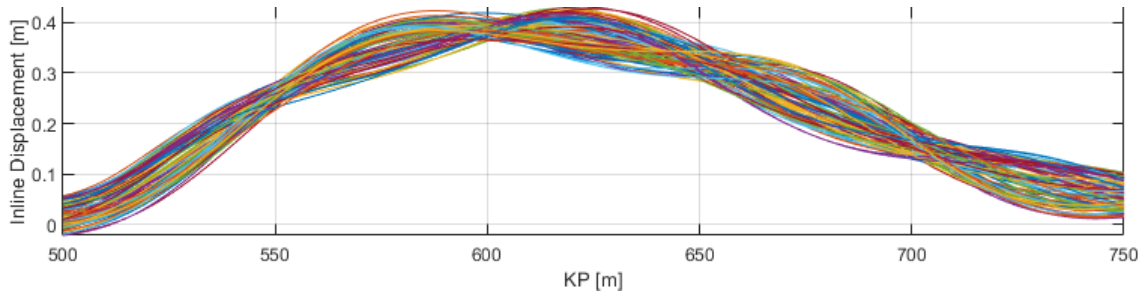
Figure 10.53: In-line displacement pattern. 0.4745 m/s current velocity 90° relative to geographic North.
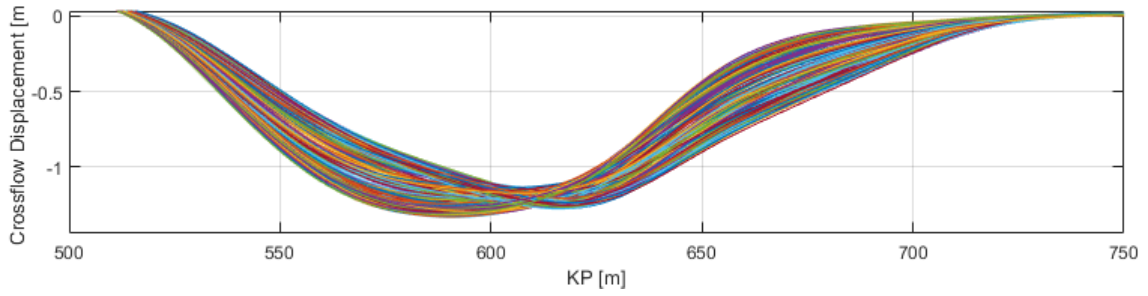

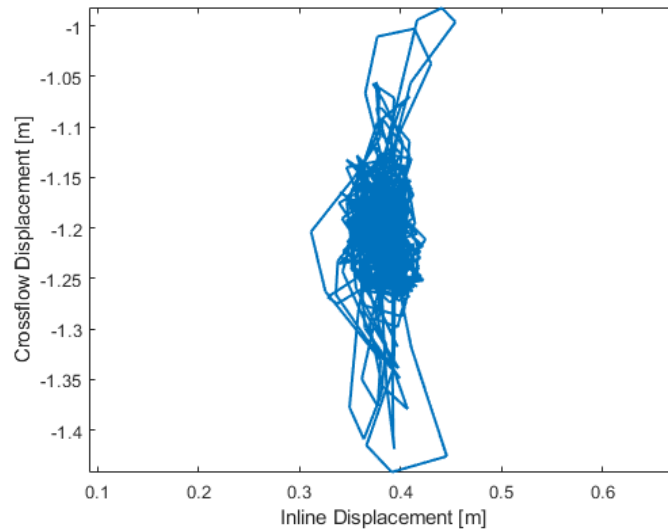Figure 10.54: Cross-flow displacement pattern. 0.4745 m/s current velocity 90° relative to geographic North.

Figure 10.55: Combined in-line and cross-flow displacement pattern at midspan. 0.4145 m/s current velocity 90° relative to geographic North.

0.5345 m/s

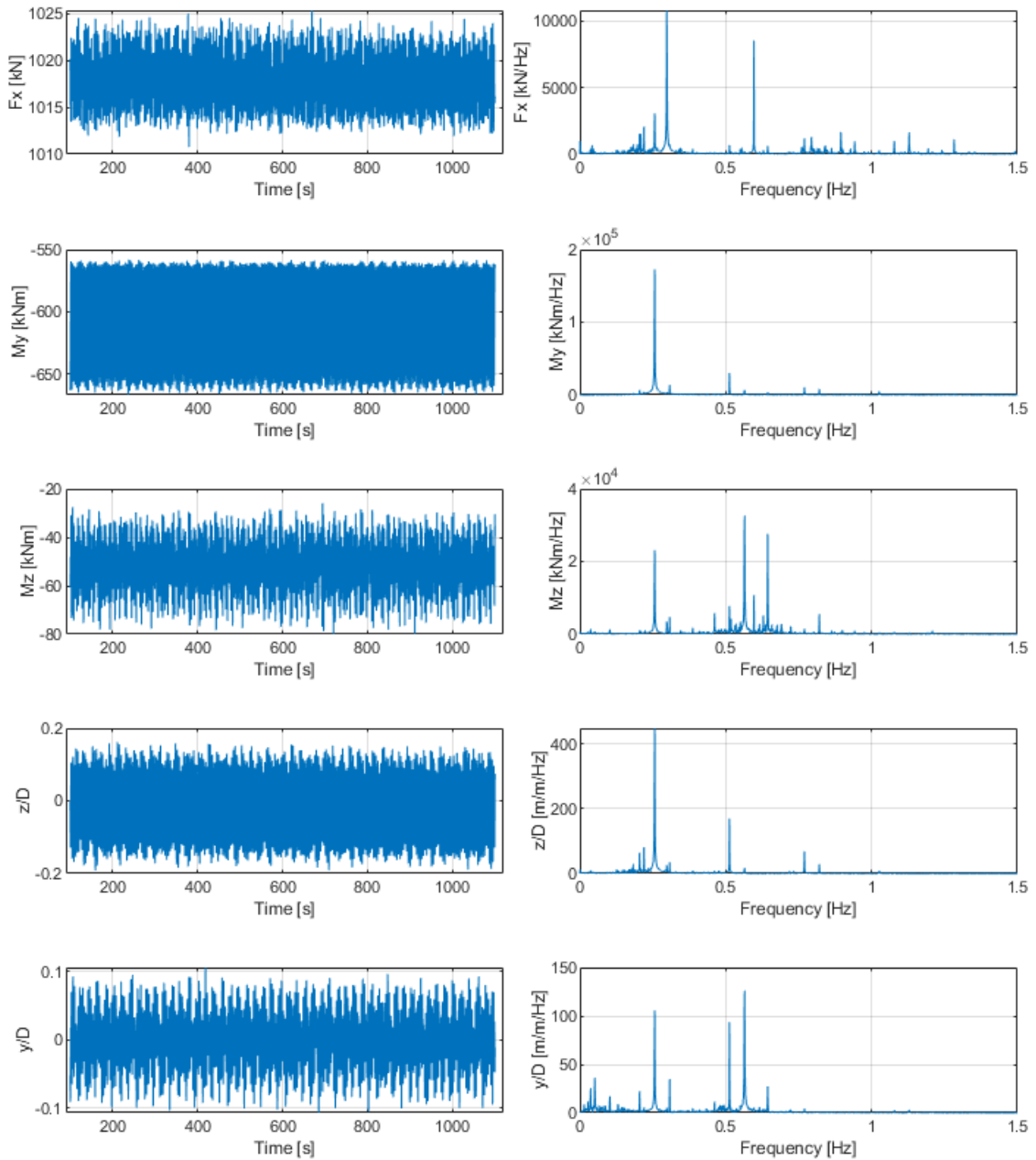Figure 10.56: Time histories and FFT of axial force, Fx, cross-flow bending moment, My, and in-line bending moment, Mz, at shoulder element 342. z/D and y/D are normalized with respect to diameter cross-flow and in-line response amplitude at node 512 (midspan), respectively. 0.5345 m/s current velocity 90° relative to geographic North.
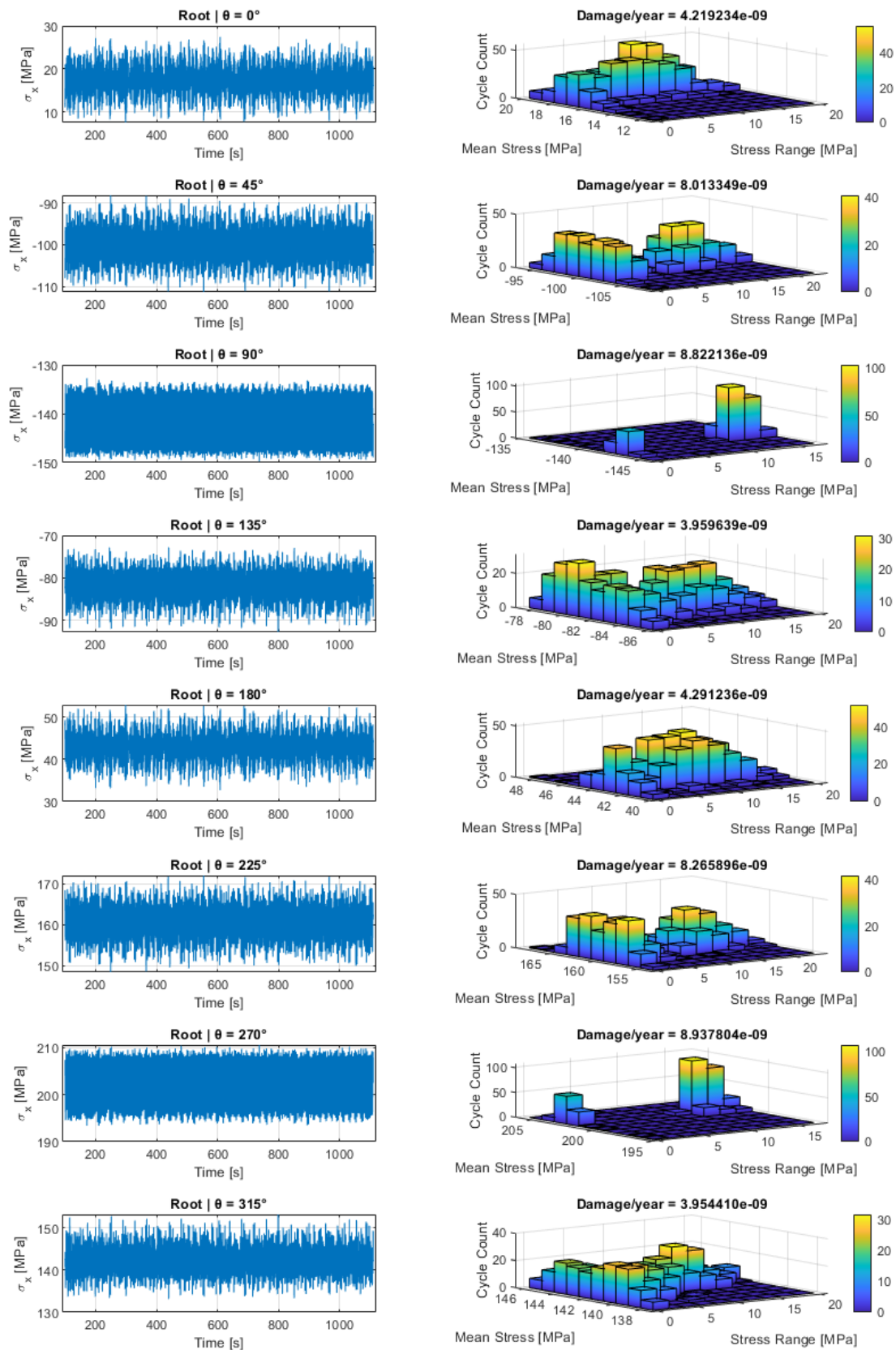
Figure 10.57: Longitudinal stress history at root position for different θ-angles around the pipeline cross-section to the left. Corresponding Rainflow counting and fatigue damage/y (current probability of occurrence included) to the right. 0.5345 m/s current velocity 90° relative to geographic North.
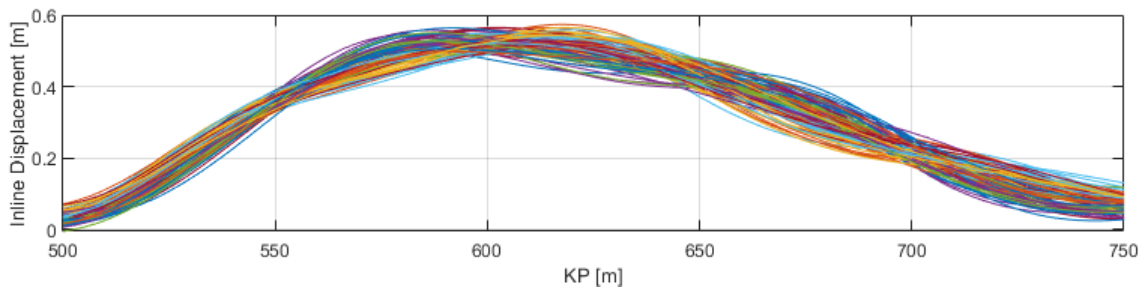
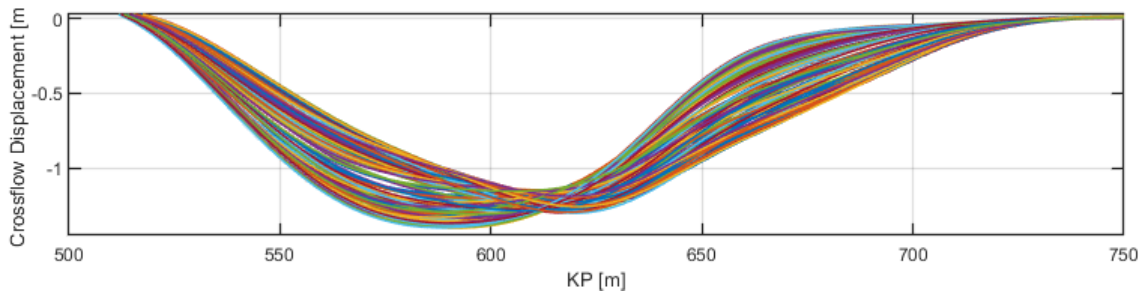Figure 10.58: In-line displacement pattern. 0.5345 m/s current velocity 90° relative to geographic North.

Figure 10.59: Cross-flow displacement pattern. 0.5345 m/s current velocity 90° relative to geographic North.
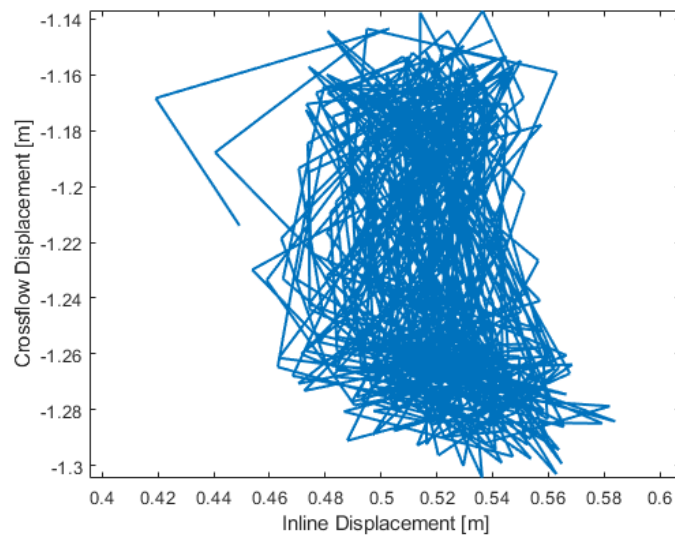

Figure 10.60: Combined in-line and cross-flow displacement pattern at midspan. 0.5345 m/s current velocity 90° relative to geographic North.

0.5945 m/s

Figure 10.61: Time histories and FFT of axial force, Fx, cross-flow bending moment, My, and in-line bending moment, Mz, at shoulder element 342. z/D and y/D are normalized with respect to diameter cross-flow and in-line response amplitude at node 512 (midspan), respectively. 0.5945 m/s current velocity 90° relative to geographic North.

Figure 10.62: Longitudinal stress history at root position for different θ-angles around the pipeline cross-section to the left. Corresponding Rainflow counting and fatigue damage/y (current probability of occurrence included) to the right. 0.5945 m/s current velocity 90° relative to geographic North.

Figure 10.63: In-line displacement pattern. 0.5945 m/s current velocity 90° relative to geographic North.

Figure 10.64: Cross-flow displacement pattern. 0.5945 m/s current velocity 90° relative to geographic North.

Figure 10.65: Combined in-line and cross-flow displacement pattern at midspan. 0.5945 m/s current velocity 90° relative to geographic North.

11 Sensitivity study

11.1 Shoulder element

A sensitivity study on the shoulder element was performed in order to investigate the importance of choosing the correct element where maximum cross-flow fatigue damage/y is anticipated. In this study, all the elements at the shoulder of the free span were investigated by extracting the axial force and bending moments of each element and then calculating the bending stress at $\theta = 270$. Figure 10.15 displays that a current velocity of 0.2945 m/s from 90 degrees relative to the geographic North gave the largest damage/y at the shoulder, thus this current condition was used as the environmental load for this sensitivity study. The simulation length used was the same as for previous runs, and Figure 11.1 gives the axial load and moment outputs as well as the calculated stress for elements 340-350. Further, the rainflow counting algorithm together with the root SN curve was used to find the cross-flow damage/y for each element as shown in Figure 11.2. It becomes evident from the figure that the element used in the case scenario (element 342) has less damage/y compared to element 345, which has the maximum damage/y. The damage/y for element 345 is 6.9×10^{-4}, which is close to 3 times larger than for element 342 which is 2.47×10^{-4}.

The maximum fatigue damage/y occurring at a different element in the TD-VIV model compared to the response model can be attributed to the presence of non-linearities and shifting constraints in the former. The TD-VIV model incorporates these non-linear effects, such as material yielding and varying contact conditions, which cause the stress and strain distribution to dynamically change as the pipeline moves. In contrast, the response model uses linear approximations for the modal response, neglecting shifting constraints and non-linear effects. As a result, it underestimates the influence of these factors, leading to a different prediction of the element experiencing maximum damage/y. In the cross-flow direction, the pipeline is subjected to alternating lift forces caused by vortex shedding. These forces induce bending moments and vertical displacements, leading to complex interactions between the pipeline and its surrounding environment. The non-linear effects, such as shifting constraints and soil contact interactions, play as mentioned a significant role in redistributing stresses and strains along the pipeline. As a result, the location of maximum damage/y dynamically changes as the pipeline responds to varying cross-flow conditions. On the other hand, in the in-line direction, the pipeline experiences predominantly axial loading and elongation due to internal pressure and thermal expansion, as well as alternating drag forces caused by vortex shedding. These forces induce bending moments and lateral displacements that are smaller in amplitude compared to CF direction, and the linear approximations used in the response model are generally more accurate in capturing the behaviour of the pipeline under such conditions. Hence, the shifting constraints and non-linear effects are generally more pronounced in the CF direction and have a relatively larger impact on the distribution of fatigue damage compared to the IL direction.

The difference in damage/y between these two elements highlights the sensitivity of the results to the choice of element. In other words, the results are highly dependent on selecting the correct element. Therefore, future studies and post-processing methods should account for this sensitivity and ensure that the correct element is chosen to obtain accurate results. To improve the accuracy of the results, it is recommended to perform further studies using different environmental loads to confirm the sensitivity of the results to the choice of element. Additionally, the study could be expanded to include a larger number of elements to get a more comprehensive understanding of the stresses in the shoulder region and/or across the whole free spanning pipeline. Finally, the results could be compared to experimental data to validate the simulation approach and ensure that the results are reliable.
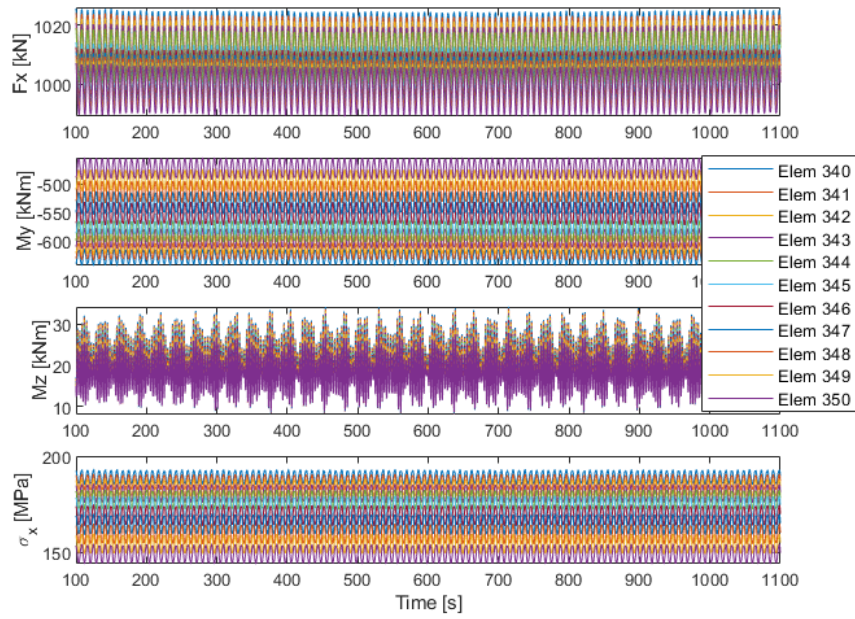
Figure 11.1: TD-VIV output data and longitudinal stress calculations for element 340-350.
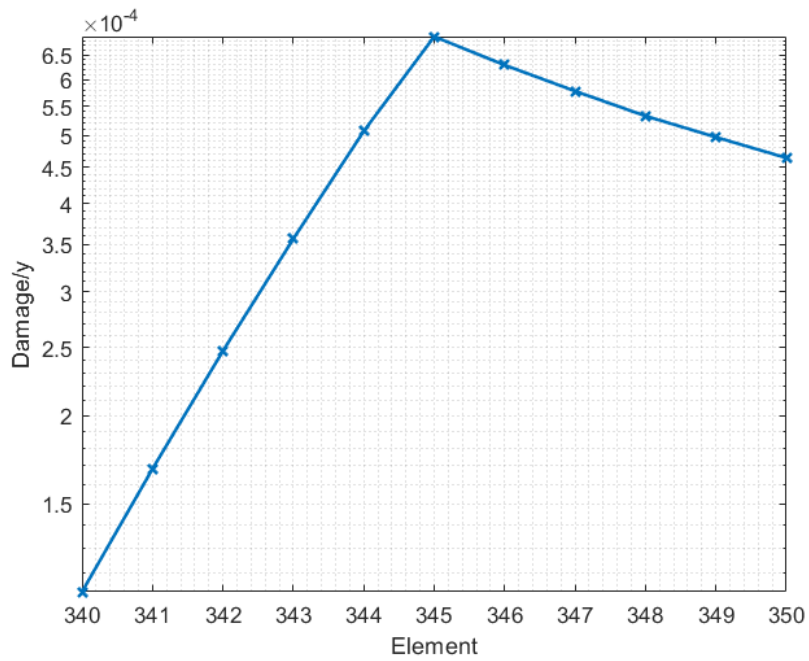

Figure 11.2: TD-VIV model damage/y vs. element number.

11.2 Hydrodynamic coefficients

The hydrodynamic coefficients used in the case study were directly taken from the SIMLA user manual [25]. The parameters there have been intensively studied and optimised focusing specifically on risers, and might not accurately be representable for a free spanning pipeline scenario. A study performed by Farantos [28] aimed to validate and calibrate the TD VIV prediction tool for free spanning pipelines, focusing on both pure IL and combined IL and CF VIV. The study used a calibration procedure to find one set of empirical hydrodynamic coefficients that produced results in good agreement with reference data. The study varied the non-dimensional frequency of maximum energy transfer in the two directions to account for both pure IL and CF-induced IL vibrations simultaneously. The reduction of the values of these frequencies resulted in the prediction of smaller values for the dominant vibration frequencies in both directions and a small increase in the obtained results for the response amplitudes. The study found that reducing the values of these frequencies leads to the prediction of the transition from pure IL to the combined CF and IL phenomenon at slightly higher current velocities. The study concluded that *Parameter Set No. 8* which is given in Table 11.1 as *Set 2* is the overall optimum parameter set with regard to all three investigated test series, as it was able to predict the experimentally captured VIV response accurately or to give slightly more conservative results.

In this section, the parameter set from the study is used in a sensitivity and correlation study for the realistic free spanning pipeline case given. The in-line and cross-flow response amplitude, stress and fatigue damage/y are presented and compared with the response model in FatFree for individual current velocities from 90 degrees relative to geographic North. Note that in this study, the damage/y is not influenced by the probability of occurrence, as it is set to unity for each individual current. A parameter *Set 3* was introduced as the response amplitude for sets 1 and 2 in the cross-flow direction was less compared to the response model in FatFree. The set is similar to *Set 1* but with a lower value for the quadratic drag coefficient in the normal direction.

Description	Symbol	Unit	Set 1	Set 2	Set 3
Quadratic drag coefficient in normal direction	C_{Dn}	-	1.2	1.2	0.7
Quadratic drag coefficient in tangential direction	C_{Dt}	-	0.1	0.1	0.1
Added mass coefficient in normal direction	C_{An}	-	1.0	1.0	1.0
Added mass coefficient in tangential direction	C_{At}	-	0.1	0.1	0.1
Cross-flow vortex shedding coefficient	$C_{v,y}$	-	1.0	0.85	1.0
In-line vortex shedding coefficient	$C_{v,x}$	-	0.8	0.75	0.8
Maximum cross-flow energy transfer frequency	$\hat{f}_{0,y}$	-	0.18	0.144	0.18
Minimum cross-flow synchronization range	$\hat{f}_{min,y}$	-	0.125	0.08	0.125
Maximum cross-flow synchronization range	$\hat{f}_{max,y}$	-	0.3	0.208	0.3
Maximum in-line energy transfer frequency	$\hat{f}_{0,x}$	-	0.5	0.36	0.5
Minimum in-line synchronization range	$\hat{f}_{min,x}$	-	0.3	0.1	0.3
Maximum in-line synchronization range	$\hat{f}_{max,x}$	-	0.7	0.9	0.7

Table 11.1: *Set 1* is the default hydrodynamic parameters used in the TD-VIV model in SIMLA and *Set 2* is from the study from Farantos [28]. *Set 3* is similar to 1 but with a reduced quadratic drag coefficient in the normal direction.

11.2.1 Effect on response amplitude

The normalized with respect to diameter in-line response for the different parameter sets compared to the response model in FatFree is shown in Figure 11.3. As mentioned in the case scenario results, response amplitudes (nodal displacements) from SIMLA were extracted from node 512 which is located approximately at 1/2 of the span length, i.e. at the midspan. This implies that it is more prone to accurately capture the maximum response amplitude of symmetric vibrations rather than antisymmetric, where the maximum response amplitude usually are located at 1/3 and 2/3 of the span length. FatFree response models are empirical models providing the maximum steady state VIV amplitude for each mode, hence only the symmetric modes of the span of interest are included in order to compare the responses with SIMLA. The mode shapes were presented in Section 10.2.

The in-line vortex shedding coefficient, $C_{v,x}$ was changed from 0.8 to 0.75 between sets 1 and 2 respectively. This coefficient mainly affects the response amplitude in this direction, but might also affect the cross-flow response as well due to coupling. The mean response amplitude for parameter *Set 1* was 0.14D, and 0.11D for *Set 2*. The maximum in-line energy transfer frequency, $\hat{f}_{0,x}$ was changed from 0.5 to 0.36 between *Set 1* and *Set 2* respectively. This can also affect the response amplitude, and it appears that decreasing the maximum energy transfer frequency generally leads to lower response amplitudes, especially at higher current velocities. This is consistent with the theoretical understanding that a lower maximum energy transfer frequency reduces the sensitivity of a vibrating structure to higher frequency excitations, while a higher maximum energy transfer frequency increases this sensitivity. In the context of the TD-VIV model, the lower value reduces the instantaneous vortex shedding frequency. The synchronization range is 0.4 and 0.8 for *Set 1* and *Set 2* respectively, which means that the system can maintain its vibration frequency and amplitude over a broader range for *Set 2*. This might explain why the response of *Set 1* has a more non-monotonic behaviour than *Set 2*, which assumingly is more realistic for the free span scenario if compared to the response in FatFree. At last, we see that the response for parameter *Set 3* resembles *Set 1*, but with significantly larger response amplitudes with a mean value of 0.17D, and broader response intervals. This is the effect of decreasing the quadratic drag coefficient, C_{Dn}, from 1.2 to 0.7. The quadratic drag force is proportional to the square of the velocity, and reducing the coefficient means that the drag force will decrease at a slower rate with increasing velocity. As a result, the object will experience less resistance as it moves faster, allowing it to reach higher velocities before the drag force becomes significant enough to slow it down. This can lead to larger response amplitudes and broader response intervals, as the object is able to maintain higher velocities for longer periods of time before being slowed down by the drag force.
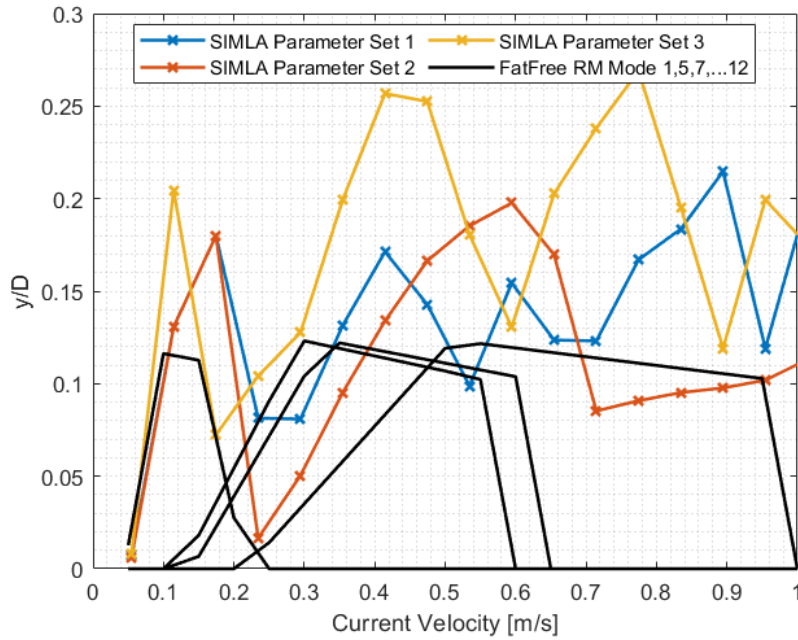
Figure 11.3: Response amplitude vs. current velocity for in-line direction. Response model vs. TD-VIV model.

The normalized with respect to diameter cross-flow response for the different parameter sets compared to the response model in FatFree is shown in Figure 11.4. The cross-flow vortex shedding coefficient, $C_{v,y}$ was changed from 1.0 to 0.85 between sets 1 and 2 respectively. This coefficient mainly affects the response amplitude in this direction, but might also affect the in-line response as well due to coupling. The mean response amplitude for parameter *Set 1* was 0.34D, and 0.36D for *Set 2*. The maximum cross-flow energy transfer frequency, $\hat{f}_{0,y}$ was changed from 0.18 to 0.144 between *Set 1* and *Set 2* respectively. This can also affect the response amplitude, and it appears that decreasing the maximum energy transfer frequency leads to lower response amplitudes at higher current velocities. This is consistent with the theoretical understanding that a lower maximum energy transfer frequency reduces the sensitivity of a vibrating structure to higher frequency excitations, while a higher maximum energy transfer frequency increases this sensitivity. In the context of the TD-VIV model, the lower value reduces the instantaneous vortex shedding frequency. The synchronization range is 0.175 and 0.2 for *Set 1* and *Set 2* respectively, which means that the system can maintain its vibration frequency and amplitude over a broader range for *Set 2*. This explains why the response for *Set 2* is over a broader range of the current interval compared to *Set 1*. It is evident that the response of the first mode of vibration in SIMLA and FatFree initiates at approximately the same current speed, but increases more rapidly in amplitude and has a narrower current interval. At last, we see that the response for parameter *Set 3* resembles *Set 1*, but with significantly larger response amplitudes with a mean value of 0.54D. This is the effect of decreasing the quadratic drag term as explained for the in-line response.

Overall, the changes in the parameters made had a significant effect on the response of the pipeline, as demonstrated by the differences in response amplitudes and behaviour between the sets. These results underscore the importance of carefully selecting parameter values when designing and analyzing free spanning pipelines and highlight the need for a comprehensive parameter study to find optimal parameters for the TD-VIV model on free spans. Additionally, there is no underlying experimental data for the span of interest, and deciding which parameter set which represents the underlying physics and the real-world scenario the most, was not possible in this case.
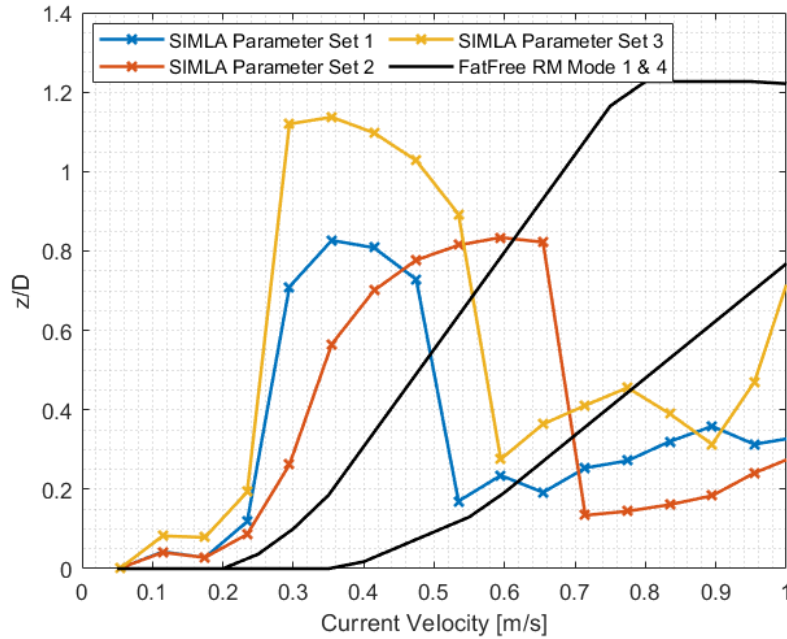
Figure 11.4: Response amplitude vs. current velocity for cross-flow direction. Response model vs. TD-VIV model.

11.2.2 Effect on stress

Figure 11.5 and 11.6 display the in-line stress at shoulder element 342 from the TD-VIV parameter study and the modal stress from the response model in FatFree, respectively. Between parameter *Set 1* and 2 for the in-line stresses, it can be seen a decrease in stress amplitude for *Set 2*, which generally agrees with the decrease in the mean response amplitude seen for the in-line response in the previous section. Between parameter *Set 1* and 3, the decrease in quadratic drag for *Set 3* gives larger stresses over broader current intervals compared to *Set 1*, as expected. It should be mentioned that the response at the shoulder element might deviate significantly from the response at the mid-span, due to the influence of varying current profiles along the span, pipe-soil interaction, and other non-linear effects on the model. This means that correlating the stresses and fatigue damage to the response amplitudes in the previous section might not be accurate. Further, it should be mentioned that a direct comparison between the stresses between the TD-VIV model and FatFree is difficult, due to multi-modal responses and not knowing which modes are activated in FatFree at different current velocities. Nonetheless, by comparing the stresses from the TD-VIV model and the modal stresses, they seem to correlate well for the lower in-line modes. Interestingly, from mode 13 and outward, there is a significant increase in stresses, which does not correlate to the TD-VIV analysis at all. By only activating the higher modes in FatFree, it can be concluded that these stress amplitudes contribute to the response at higher velocities

and significantly affect the fatigue damage/y as shown in the next subsection.
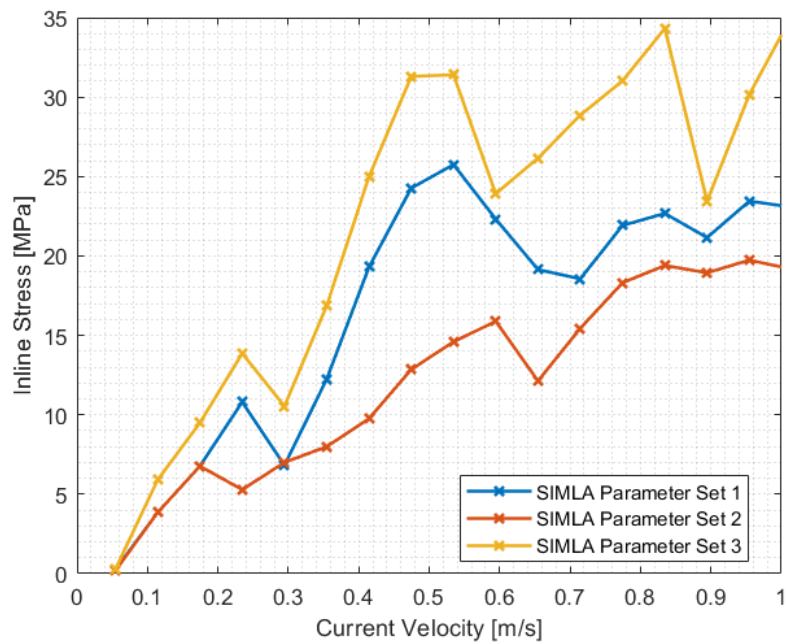

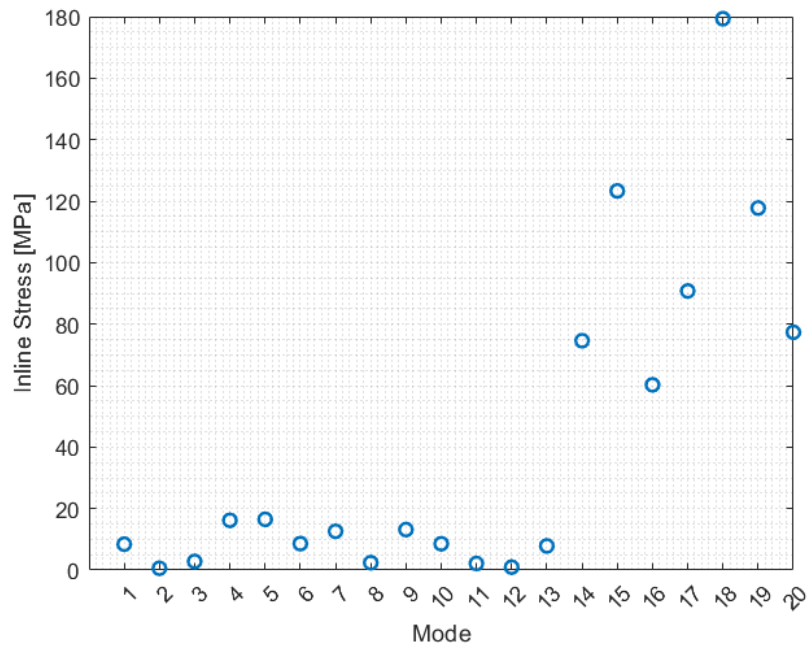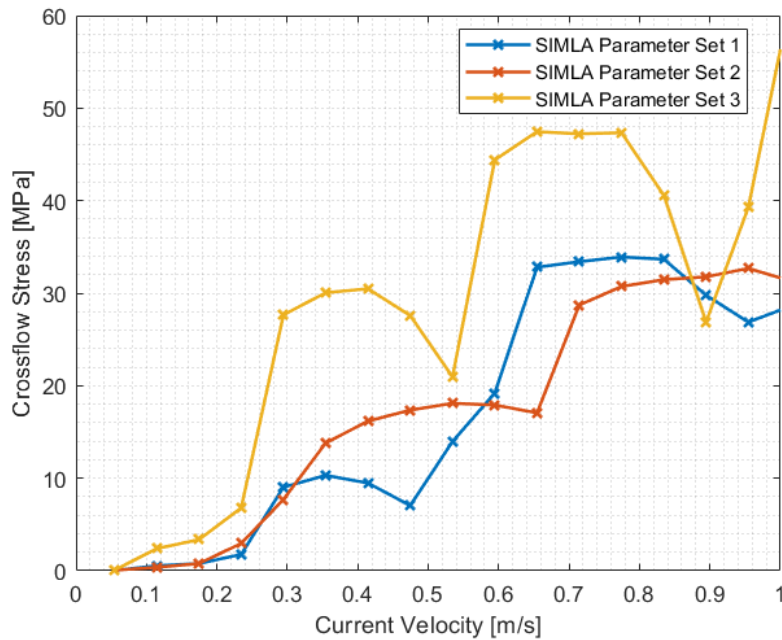Figure 11.5: Stress vs. current velocity for in-line direction ($\theta = 0$).

Figure 11.6: In-line stress vs. mode number for response model.

Figure 11.7 and 11.8 display the cross-flow stress at shoulder element 342 from the TD-VIV parameter study and the modal stress from the response model in FatFree, respectively. The individual peak intervals represent the response to a certain mode, where the first peak interval corresponds to the first mode of vibration, and the second interval to the second mode of vibration. Between parameter *Set 1*

and 2, the cross-flow stress is larger in amplitude and over a broader current range for parameter *Set 2*. This is consistent with the increase in the synchronization range, and it can be concluded that lock-in occurs over a broader range of velocities when increasing this parameter. Between parameter *Set 1* and 3, the decrease in quadratic drag for *Set 3* gives significantly larger stresses over broader current intervals compared to *Set 1*, as expected. It should be mentioned that the response at the shoulder element might deviate significantly from the response at the mid-span, due to the influence of varying current profiles along the span, pipe-soil interaction, and other non-linear effects on the model. This means that correlating the stresses and fatigue damage to the response amplitudes previously is not recommended. Further, it should be mentioned that a direct comparison between the stresses between the TD-VIV model and FatFree is difficult, due to multi-modal responses and not knowing which modes are activated in FatFree at different current velocities. Nonetheless, by comparing the stresses from the TD-VIV model and the modal stresses, it can be seen that the first mode in FatFree gives a cross-flow stress of 22MPa, and by comparing this value to the responses in SIMLA it can be seen that parameter *Set 1* and 3 deviates the most, while *Set 2* has a maximum response of 19MPa in its peak interval. For the second mode in FatFree the cross-flow stress is 21.5MPa, which is significantly lower than the responses in SIMLA which are 30MPa and above.

Figure 11.7: Stress vs. current velocity for cross-flow direction ($\theta = 270$).
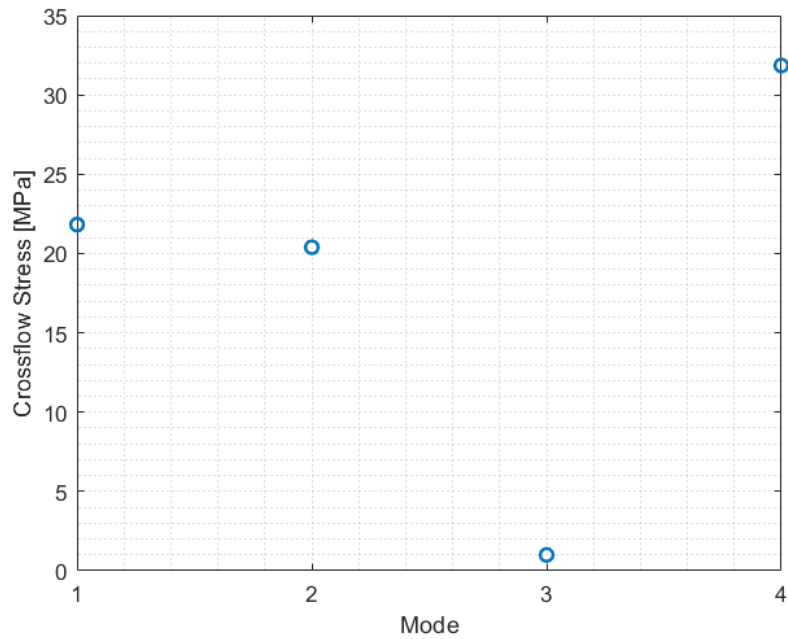
Figure 11.8: Cross-flow stress vs. mode number for response model.

11.2.3 Effect on damage/y

Figure 11.9 and 11.10 display the in-line and cross-flow damage/y as a function of current velocity, re-spectively. For velocities in the interval of 0-0.5m/s, it is seen for the in-line damage/y that the trendline correlates well between the different parameter sets and the FatFree result. For the lowest velocities, FatFree is limited to a damage/y of 10^{-6}. Parameter *Set 1* correlates best with the results from FatFree in this interval, while *Set 2* and 3 deviate with approximately plus and minus one or two powers of ten. In the current interval of 0.5-1.0m/s, there is as mentioned significantly higher in-line damage/y from FatFree compared to the SIMLA results, which is due to activation of the higher modes shown in Figure 11.6.

As for the cross-flow damage/y, it is, in general, larger and thus more conservative in FatFree compared to the SIMLA results. The observed differences between the cross-flow damage/y results obtained from FatFree and SIMLA can be attributed to the influence of non-linearities and shifting constraints present in the cross-flow direction, affecting the stress and strain distribution along shoulder elements. In the SIMLA analysis, these non-linear effects and shifting constraints were considered, resulting in generally lower cross-flow damage/y values compared to FatFree.
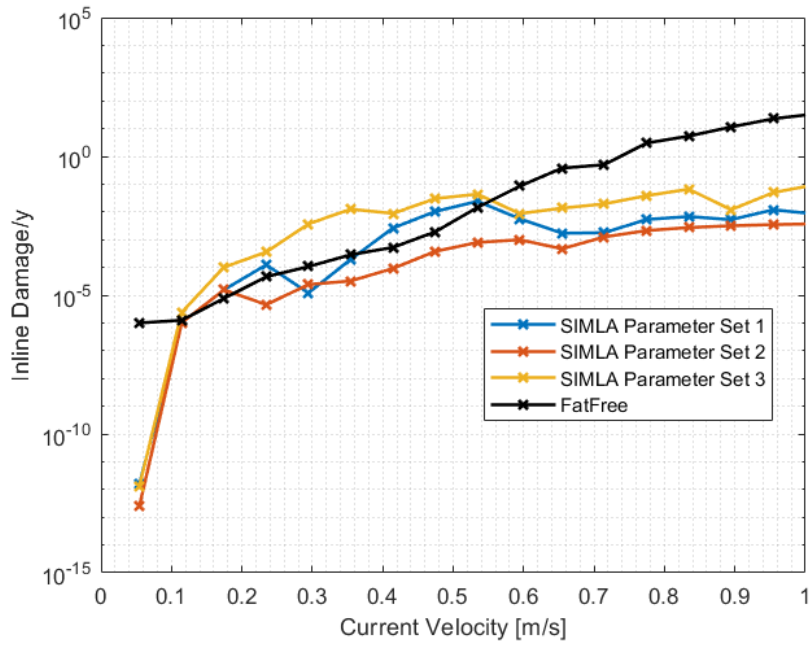
Figure 11.9: Damage/y vs. current velocity for in-line direction ($\theta = 0$).
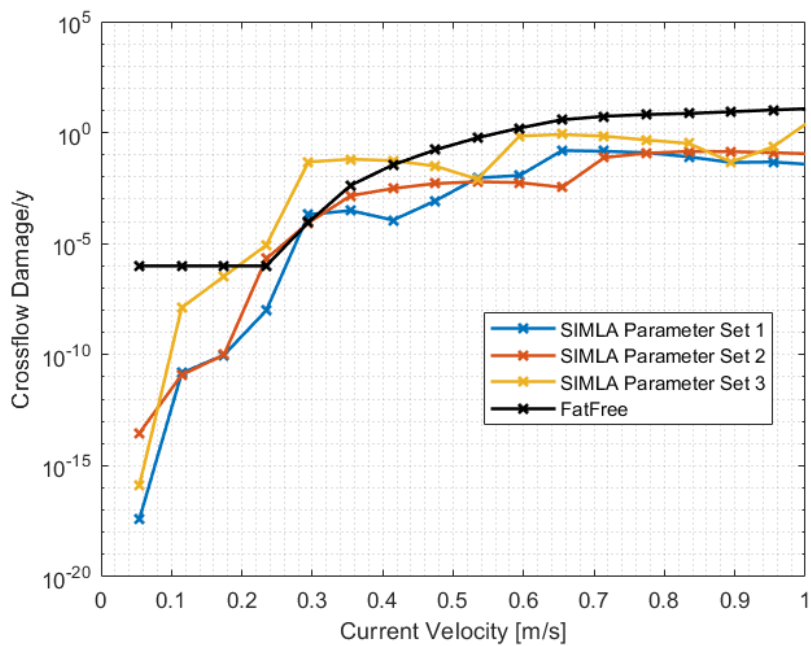
Figure 11.10: Damage/y vs. current velocity for cross-flow direction ($\theta = 270$).

12 Conclusion & recommendations

12.1 Conclusion

A realistic free span scenario was given by Reinertsen New Energy in order to perform fatigue analysis using two different VIV prediction models; the recommended response-based model in *DNV-RP-F105: Free Spanning Pipelines* [11], and a newly developed TD-VIV model at NTNU. The software FatFree was used in compliance with the response-based model, and the FEM tool SIMLA was used for the TD-VIV model. The fatigue damage/y at shoulder element 342 was investigated and compared for a given environmental loading condition using both approaches. For the specific case scenario, the in-line damage/y in FatFree and SIMLA was in good agreement, with a damage/y of 3.6×10^{-6} and 4.16×10^{-6}, respectively. The cross-flow damage/y in FatFree were 4.72×10^{-5} and 3.14×10^{-6} in SIMLA, thus an order in the power of ten difference between the two, making FatFree the more conservative result.

A sensitivity study was performed on the neighbouring shoulder elements of element 342 to investigate the importance of selecting the correct element for the damage analysis. A representative current direction from the environmental loading condition was used in the study. The results showed a significant difference in the maximum damage/y between elements 340-350. Notably, element 345 exhibited the largest damage/y among all the elements for this loading condition, with values approximately three times larger than that of element 342. This discrepancy can be attributed to the presence of non-linearities and shifting constraints in the TD-VIV model, which captures the dynamic changes in stress and strain distribution as the pipeline moves. In contrast, the response model, which uses linear approximations for the modal response, neglects these effects and underestimated their influence, especially for the cross-flow direction. These findings highlight the importance of including non-linear effects and selecting the correct element for fatigue damage calculation and suggest the need for future studies and post-processing techniques and procedures to account for this sensitivity.

A parameter study on the hydrodynamic coefficients used for the TD-VIV model in SIMLA was conducted. Three different parameter sets were investigated, where *Set 1* (which was used for the case scenario) uses the default parameters given by Sævik et al. [25] in the SIMLA user manual. *Set 2* uses coefficients from the parameter study by Farantos [28], which aimed to validate and calibrate the TD-VIV prediction tool for free spanning pipelines, focusing on both pure IL and combined IL and CF VIV. Finally, *Set 3* is similar to *Set 1*, but with a reduced quadratic drag coefficient. The effect of changing parameter sets was explored by looking at the differences in the response amplitude, stress, and damage/y between the results for the in-line and cross-flow directions. Additionally, it was compared to the results from FatFree.

Regarding the in-line response amplitude, *Set 1* and *Set 2* correlates well with the response model in FatFree, while *Set 3* predicts a significantly larger response. *Set 1* has a more non-monotonic behaviour compared to *Set 2*, which can be linked to the reduction in maximum in-line transfer frequency and synchronization range. This behaviour is more similar to the modal response amplitudes in FatFree. Thus, as seen in the case scenario, the dynamic response in SIMLA was in good agreement with the modal response in FatFree for *Set 1*, making it the more favourable parameter set for the in-line direction. The in-line stresses between the two models seemed to correlate well at lower current velocities. Interestingly, at higher velocities, the stresses were significantly larger in the response model. This was further seen in the fatigue damage/y results, where the damage/y correlated well between 0-0.6 m/s current velocity, but at higher velocities the response model was significantly more conservative. The reason for this was that at higher current velocities, the activation of unrealistically high in-line modes produced

stresses significantly larger than stresses from the dynamic analysis. The current velocities in the case scenario were between 0-0.6 m/s, hence these higher modes were not activated and did not influence the results for the case scenario, which can be seen by the good agreement between in in-line damage/y results for the case.

As for the cross-flow response amplitude, none of the parameter sets corresponded well with the response model in FatFree. First off, synchronization/lock-in for the TD-VIV models occurred at significantly lower current velocities for the fundamental natural frequency, and over a smaller range of current velocities. *Set 2* responded over the broadest current interval, which can be linked to the larger maximum cross-flow transfer frequency and synchronization range. Additionally, *Set 1* & *2* both respond at a maximum amplitude of approximately 0.83D, which was significantly less than the maximum amplitude for the response model, which was 1.22D. *Set 3* responded with a maximum amplitude of 1.15D, due to the reduction in quadratic drag coefficient. Looking at the damage/y, the response model is generally more conservative compared to the TD-VIV model used in SIMLA, for all current velocities. This explains the larger cross-flow damage/y in the case scenario.

12.2   Recommendations for further work

The following list is a proposal for further work:

- Validate the TD-VIV model with reference data such as experiments to ensure its accuracy and reliability in predicting VIV response and fatigue damage for free-spanning pipelines.

- Develop standard procedures and coefficients for different free span situations to make the TD-VIV model more widely applicable and easier to use for industry professionals. This could involve extensive testing and analysis of a wide range of different environmental conditions and pipeline configurations.

- Investigating the effect of different environmental loading conditions on the accuracy of the TD-VIV model in SIMLA, such as changes in water depth, current velocity, or the influence of wave loads. This could help to determine the range of conditions for which the model is most accurate and identify any limitations or areas for improvement.

- Developing post-processing techniques and procedures to account for the sensitivity of fatigue damage calculations to the choice of element for the damage analysis, as highlighted in the sensitivity study. This could involve developing algorithms or software tools to automate the process of selecting the appropriate element for damage analysis or developing guidelines for analysts to follow when selecting elements for fatigue analysis.

- Explore the potential for using machine learning techniques to improve the accuracy and efficiency of VIV prediction and fatigue analysis for free-spanning pipelines.

- Conduct field tests and case studies to validate the TD-VIV model in real-world scenarios and provide practical insights for industry professionals.

Bibliography

[1]   R.C. Hibbeler. *Fluid Mechanics, Second Edition in SI Units*. Pearson, 2021.

[2]   B.Mutli Sumer and Jørgen Fredsøe. *Hydrodynamics Around Cylindrical Structures*. World Scientific Publishing Co. Pte. Ltd., 2006.

[3]   Mats Jørgen Thorsen. 'Time domain analysis of vortex-induced vibration'. PhD thesis. 2016.

[4]   R. Gopalkrishnan. 'Vortex-induced forces on oscillating bluff cylinders'. PhD thesis. 1993.

[5]   K. Vikestad, J.K. Vandiver and C. M. Larsen. 'Added mass and oscillation frequency for a circular cylinder subjected to vortex-induced vibrations and external disturbance'. In: *Journal of Fluids and Structures* 14 (2000), pp. 1071–1088.

[6]   B.M. Sumer and J. Fredsøe. 'A Review on Vibrations of Marine Pipelines'. In: *Int. J. Offshore Polar Eng. 5* (1995).

[7]   R. D. Blevins. *Vibration of structures induced by fluid flow*. - Harris' shock and vibration handbook. McGraw-Hill, 1990.

[8]   T. Sarpkaya. 'Fluid Forces on Oscillating Cylinders'. In: *Journal of the Waterway, Port, Coastal and Ocean Division* 104 (1978).

[9]   N. Jauvtis and C. H. K. Williamson. 'The effect of two degrees of freedom on vortex-induced vibration at low mass and damping'. In: *Journal of Fluid Mechanics* 509 (2004), pp. 23–62.

[10]   *DNV-RP-C205: Environmental Conditions and Environmental Loads*. Det Norske Veritas, 2014.

[11]   *DNV-RP-F105: Free Spanning Pipelines*. Det Norske Veritas, 2014.

[12]   *FatFree*. - Sesam User Manual. Det Norske Veritas, 2020.

[13]   Knut Vedeld, Håvar A.Sollund and Jostein Hellesland. 'Free vibrations of free spanning offshore pipelines'. In: *Engineering Structures* 56 (2013), pp. 68–82.

[14]   Knut Vedeld et al. 'Effective axial forces in offshore lines and clad pipes'. In: *Engineering Structures* 66 (2014), pp. 66–80.

[15]   O. Fyrileiv and K. Mørk. 'Structural Response of Pipeline Free Spans Based on Beam theory'. In: OMAE02, 21st International Conference on Offshore Mechanics and Arctic Engineering (Oslo, Norway). Vol. 4. ASME, pp. 175–183.

[16]   P.E. Voie et al. 'VIV Best Practice: Guideline on analysis of vortex-induced vibrations in risers and umbilicals'. In: (2002).

[17]   A.D. Trim, H. Braaten and M.A. Tognarelli. 'Experimental investigation of vortex-induced vibration of long marine risers.' In: *Journal of Fluids and Structures* 21 (2005), pp. 335–361.

[18]   *DNV-RP-F114: Pipe-soil interaction for submarine pipelines*. Det Norske Veritas, 2017.

[19]   Olav Fyrileiv, Kim .J Mørk and Knut O. Ronold. *Free Span Design According To The DNV RP-F105 For Free Spanning Pipelines*. Det Norske Veritas, 2002.

[20]   J.V. Ulveseter et al. 'Time domain simulation of riser VIV in current and irregular waves'. In: *Marine Structures* 60 (2018), pp. 241–260.

[21]   Sang Woo Kim et al. 'Prediction of deepwater riser VIV with an imrpvoed time domain model including non-linear structural behavior'. In: *Ocean Engineering* 236 (2021).

[22]   J.V. Ulveseter, S. Sævik and C.M. Larsen. 'Time domain model for calculation of pure in-line vortex-induced vibrations'. In: *Journal of Fluids and Structures* 68 (2017), pp. 158–173.

[23] Stig Berge and Sigmund Kyrre Ås. *Compendium - Fatigue and Fracture Design of Marine Structures, Third revised edition.* Norwegian University of Science and Technology, NTNU., 2017.

[24] Ragnar Sigbjörnsson Ivar Langen. *Dynamisk analyse av konstruksjoner.* SINTEF, avdeling for konstruksjonsteknikk, 1979.

[25] Svein Sævik et al. *SIMLA Version 3.21.0 User Manual.* SINTEF, 2022.

[26] Svein Sævik. *Simla Theory Manual.* SINTEF Ocean AS, 2017.

[27] K Bell. *Eigensolvers for structural problems: Some algorithms for symmetric eigenvalue problems and their merits.* Delft University Press, 1998.

[28] Christos Farantos. 'Improved VIV Prediction of Free Spanning Pipelines and Cables'. MA thesis. 2022.

Appendix

A   Flow Regimes
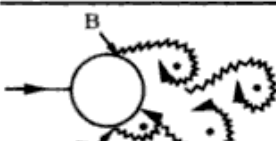
|		
a)	No separation. Creeping flow	$Re < 5$
b)	A fixed pair of symmetric vortices	$5 < Re < 40$
c)	Laminar vortex street	$40 < Re < 200$
d)	Transition to turbulence in the wake	$200 < Re < 300$
e)	Wake completely turbulent. A:Laminar boundary layer separation	$300 < Re < 3\times10^5$ Subcritical
f)	A:Laminar boundary layer separation B:Turbulent boundary layer separation;but boundary layer laminar	$3 \times 10^5 < Re < 3.5 \times 10^5$ Critical (Lower transition)
g)	B: Turbulent boundary layer separation;the boundary layer partly laminar partly turbulent	$3.5 \times 10^5 < Re < 1.5 \times 10^6$ Supercritical
h)	C: Boundary layer completely turbulent at one side	$1.5\times10^6 < Re < 4\times10^6$ Upper transition
i)	C: Boundary layer completely turbulent at two sides	$4\times10^6 < Re$ Transcritical

Figure A.1: Flow regimes

B Cap damage/y results
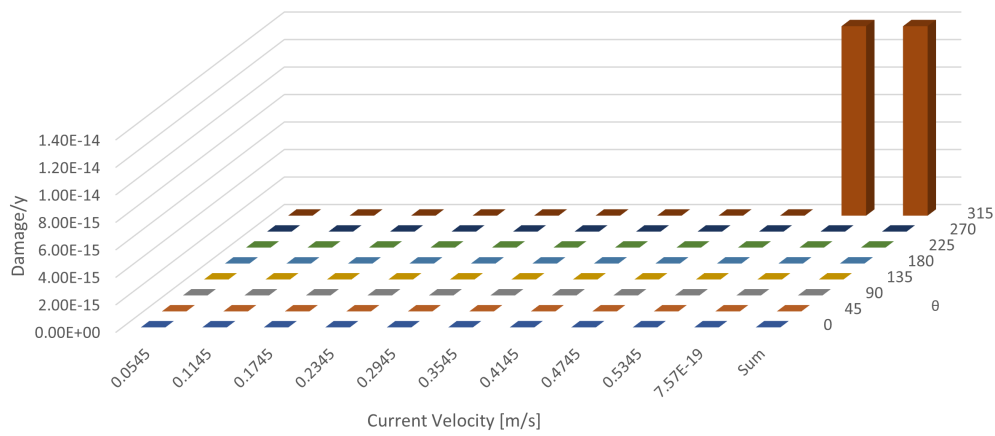
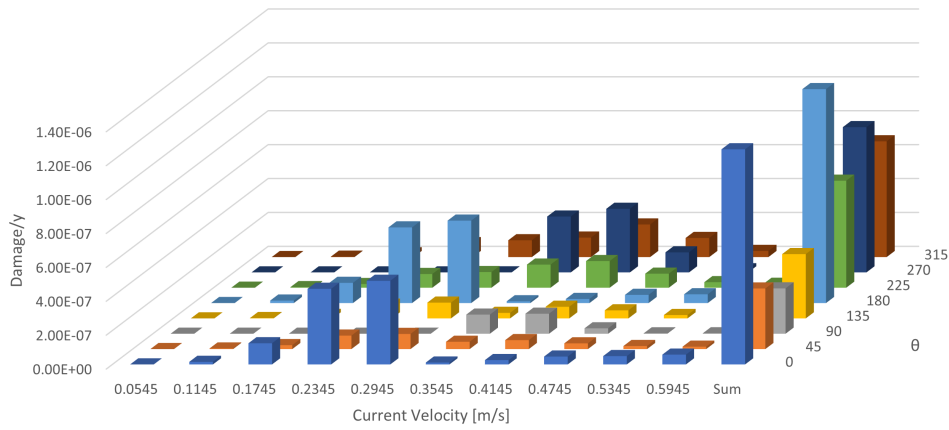Figure B.1: Cap damage/y from current 0° relative to North
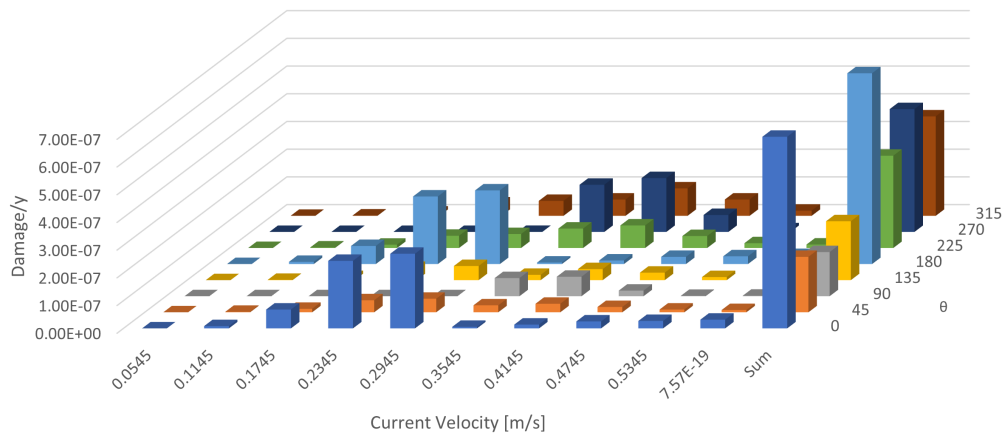
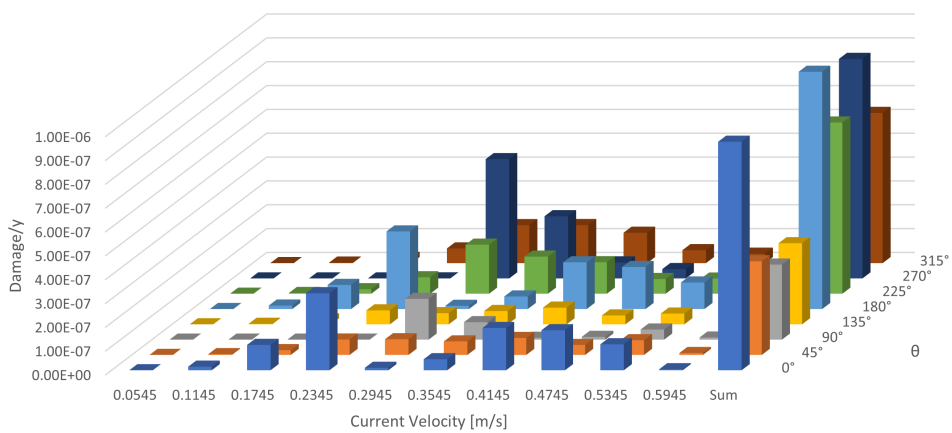Figure B.2: Cap damage/y from current 45° relative to North
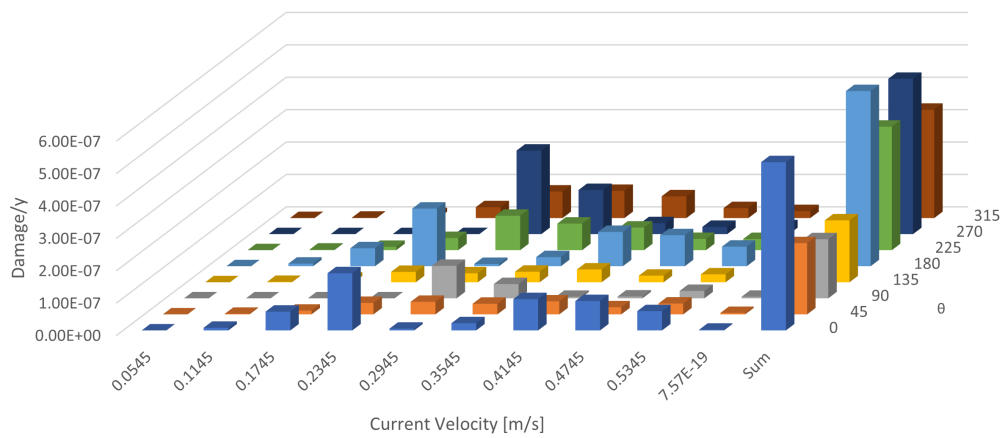
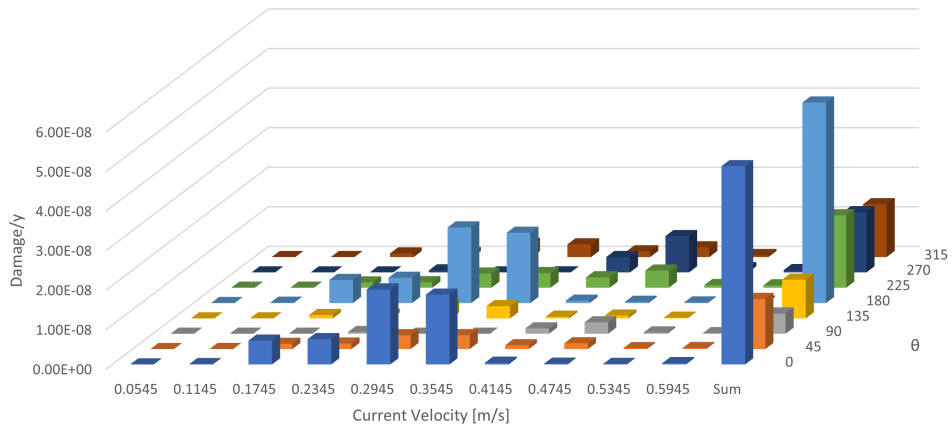Figure B.3: Cap damage/y from current 90° relative to North
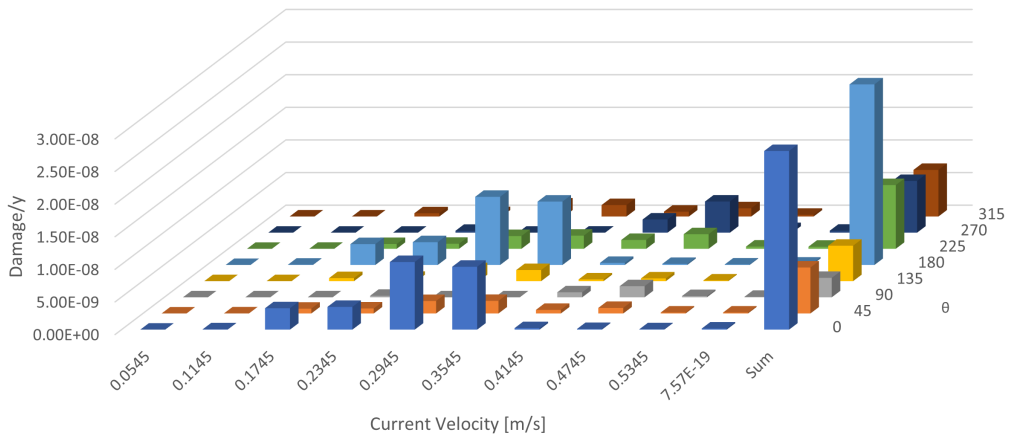
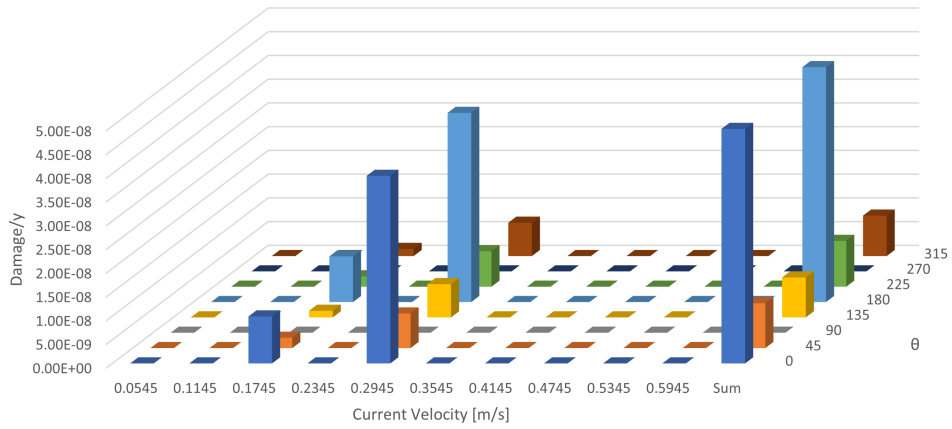Figure B.4: Cap damage/y from current 135° relative to North
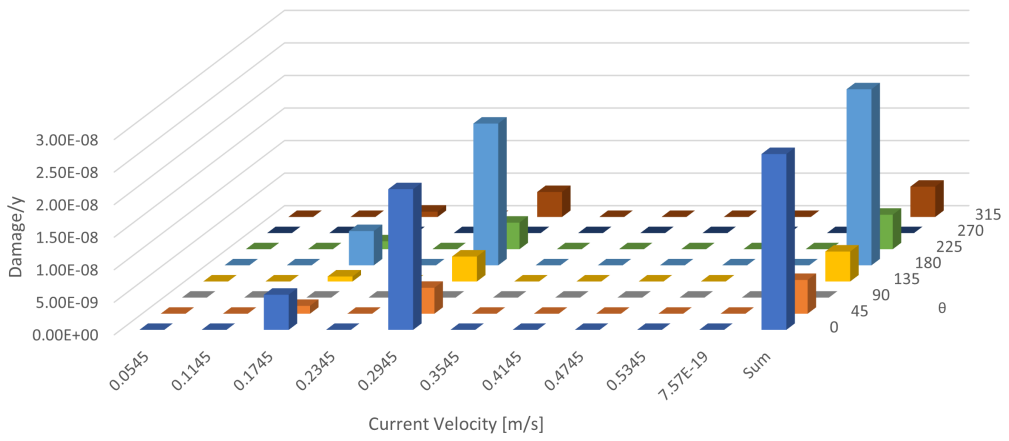
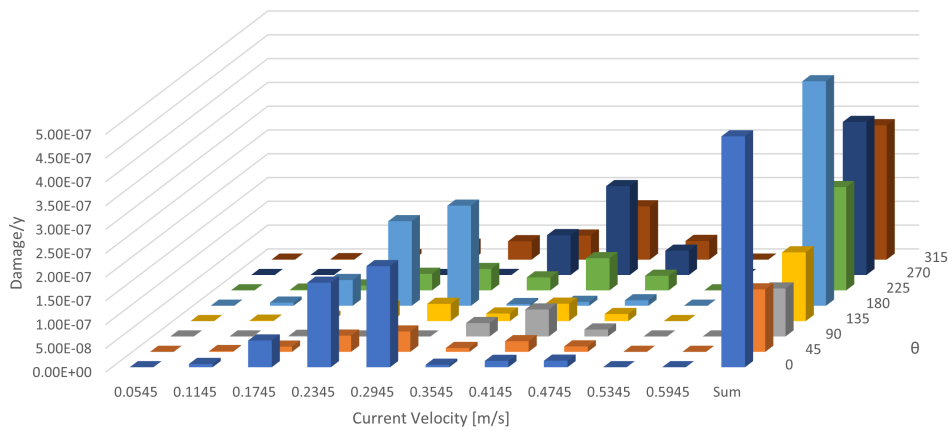Figure B.5: Cap damage/y from current 180° relative to North
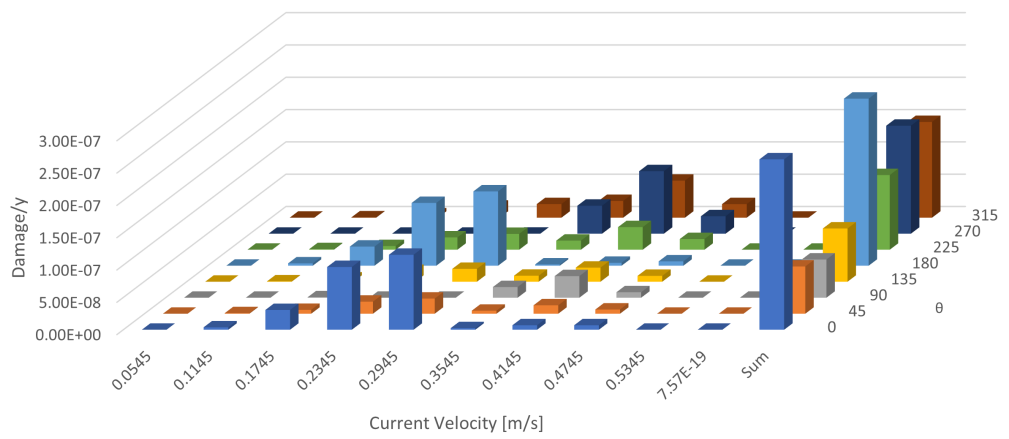
Figure B.6: Cap damage/y from current 225° relative to North
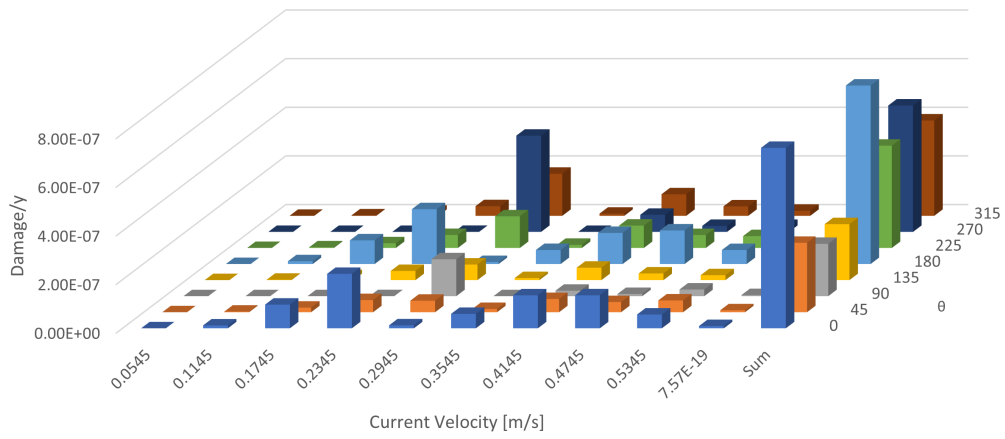
Figure B.7: Cap damage/y from current 270° relative to North
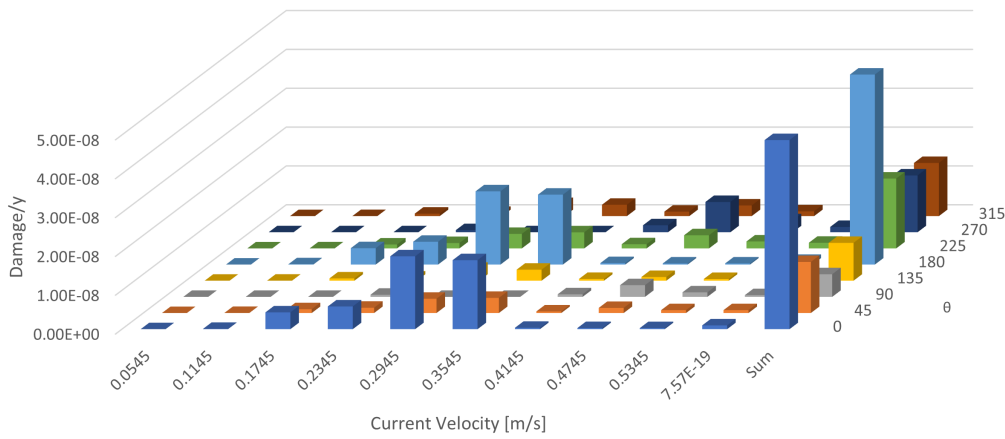
Figure B.8: Cap damage/y from current 315° relative to North
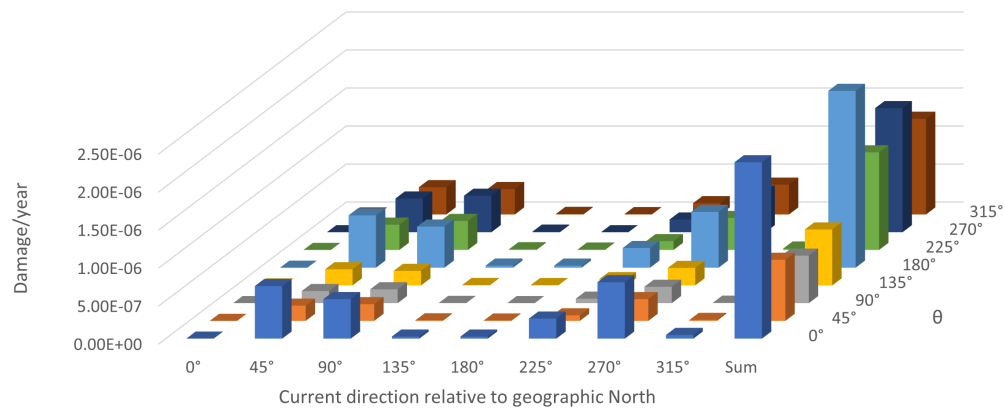
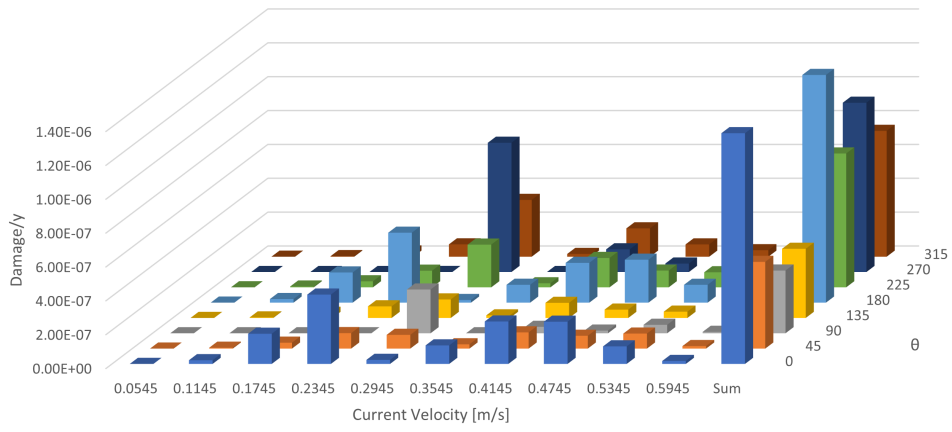Figure B.9: Cap cumulative damage/y

C   Root damage/y results
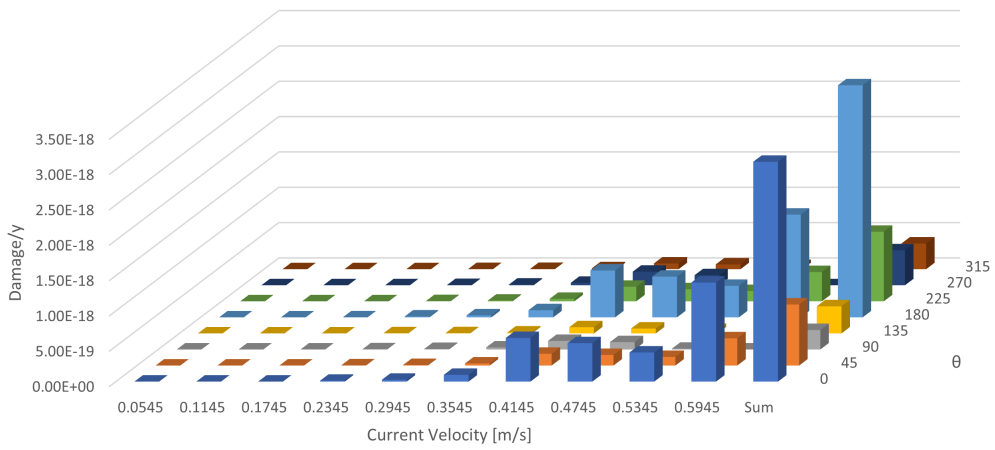
Figure C.1: Root damage/y from current 0° relative to North

Figure C.2: Root damage/y from current 45° relative to North

Figure C.3: Root damage/y from current 90° relative to North

Figure C.4: Root damage/y from current 135° relative to North

Figure C.5: Root damage/y from current 180° relative to North

Figure C.6: Root damage/y from current 225° relative to North

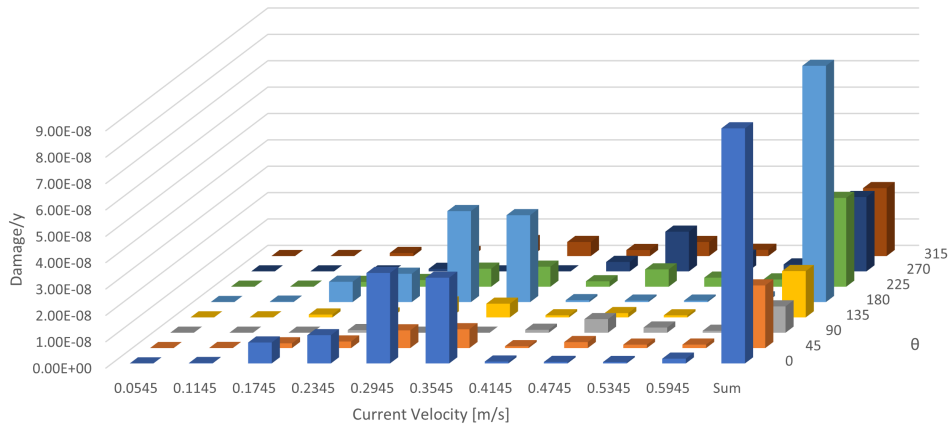Figure C.7: Root damage/y from current 270° relative to North

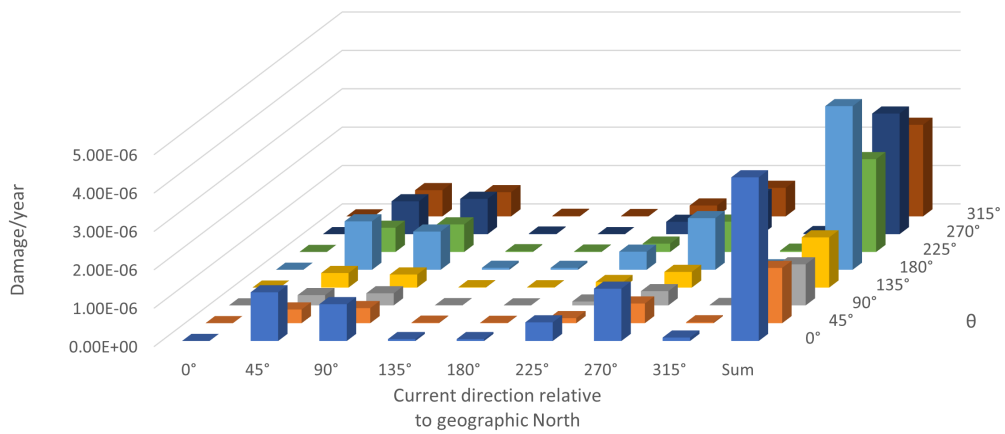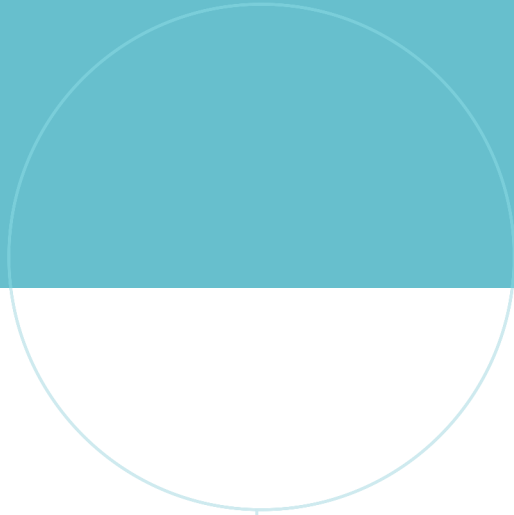Figure C.8: Root damage/y from current 315° relative to North

Figure C.9: Root cumulative damage/y